

N73-15673 SQT

MSC-05161
SUPPLEMENT 1



NATIONAL AERONAUTICS AND SPACE ADMINISTRATION

APOLLO 15 MISSION REPORT
SUPPLEMENT 1

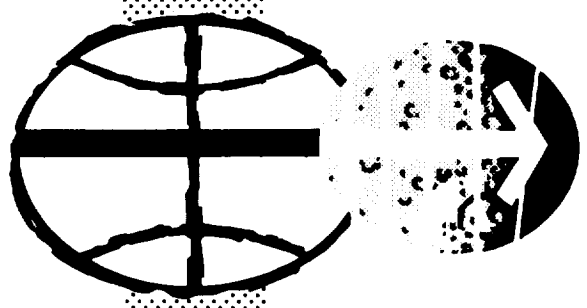
APOLLO 15 GUIDANCE, NAVIGATION, AND CONTROL
SYSTEM PERFORMANCE ANALYSIS REPORT

CASE FILE
COPY



DISTRIBUTION AND REFERENCING

This paper is not suitable for general distribution or referencing. It may be referenced only in other working correspondence and documents by participating organizations.



MANNED SPACECRAFT CENTER
HOUSTON, TEXAS
SEPTEMBER 1972

1.

2.

3.

APOLLO 15 MISSION REPORT

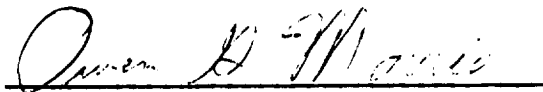
SUPPLEMENT 1

APOLLO 15 GUIDANCE, NAVIGATION AND CONTROL
SYSTEM PERFORMANCE ANALYSIS REPORT

PREPARED BY

TRW Systems

APPROVED BY

A handwritten signature in cursive script, appearing to read "Owen G. Morris", is written over a horizontal line.

Owen G. Morris

Manager, Apollo Spacecraft Program

NATIONAL AERONAUTICS AND SPACE ADMINISTRATION

MANNED SPACECRAFT CENTER

HOUSTON, TEXAS

SEPTEMBER 1972

PROJECT TECHNICAL REPORT
TASK E-38E

APOLLO 15 GUIDANCE, NAVIGATION, AND CONTROL
SYSTEM PERFORMANCE ANALYSIS REPORT

NAS 9-12330

11 FEBRUARY 1972

Prepared for
NATIONAL AERONAUTICS AND SPACE ADMINISTRATION
MANNED SPACECRAFT CENTER
HOUSTON, TEXAS

Prepared by
Electronic Systems
Engineering Department

PROJECT TECHNICAL REPORT
TASK E-38E

APOLLO 15 GUIDANCE, NAVIGATION, AND CONTROL
SYSTEM PERFORMANCE ANALYSIS REPORT

NAS 9-12330

11 FEBRUARY 1972

Prepared for
NATIONAL AERONAUTICS AND SPACE ADMINISTRATION
MANNED SPACECRAFT CENTER
HOUSTON, TEXAS

Prepared by
Electronic Systems
Engineering Department

Approved by *J. E. Alexander*
J. E. Alexander, Manager
Electronic System Engineering
Department

Approved by *D. L. Rue*
D. L. Rue, Manager
Task E-38E

.

.

.

.

TABLE OF CONTENTS

	<u>PAGE</u>
1. INTRODUCTION	1-1
1.1 Purpose	1-1
1.2 Summary	1-1
2. LM IMU PERFORMANCE	2-1
2.1 Descent Performance	2-2
2.2 Ascent Performance	2-5
3. LM AGS PERFORMANCE	3-1
3.1 Altitude and Altitude Rate Update During Descent	3-1
3.1.2 State Vector Transfers from PGNCs	3-1
3.2 Sensor Performance	3-2
3.2.1 Gyro and Accelerometer Free-flight Performance	3-2
3.2.2 AGS-PGNCs Attitude Difference During Powered Flight	3-2
3.2.2.1 Descent Attitude Differences	3-3
3.2.2.2 Ascent Attitude Differences	3-5
3.2.3 Powered Descent Velocity Comparisons	3-7
3.2.4 Ascent Velocity Comparisons	3-9
3.2.5 Comparisons of ASA Inflight Errors to Preflight Performance Estimates	3-10
3.2.5.1 Accelerometer Error Summary	3-10
3.2.5.2 Gyro Error Summary	3-10
4. DIGITAL AUTOPILOT PERFORMANCE	4-1
4.1 CSM Digital Autopilot	4-1
4.1.1 SPS Burn/Yaw SPS Gimbal Transient During TEI	4-1
4.1.2 Universal Tracking Program - Option 2	4-4
4.1.3 Universal Tracking Program - Option 5	4-4
4.2 LM Digital Autopilot	4-10
4.2.1 LM DAP Performance During Powered Descent Braking Phase	4-10

TABLE OF CONTENTS (CONTINUED)

	<u>PAGE</u>
4.2.2 LM DAP Performance During Powered Descent Approach Phase	4-11
4.2.3 LM DAP Performance During Powered Descent Landing Phase	4-12
4.2.4 LM DAP Performance During Ascent	4-13
REFERENCES	R-1

TABLES

	<u>PAGE</u>
2.1 Gyro Drifts	2-9
2.2 Accelerometer Biases	2-10
3.1 State Vector Transfer Errors	3-11
3.2 ASA 017 Gyro Static Bias Drift History (Deg/Hr)	3-12
3.3 ASA 017 Accelerometer Static Bias History (ug)	3-12
3.4 LM AGS Error Model (Accelerometer)	3-13
3.5 Accelerometer Error Summary	3-14
3.6 Gyro Bias Error Summary (Deg/Hr)	3-15
3.7 Gyro Input Axis Misalignments	3-16

ILLUSTRATIONS

		<u>PAGE</u>
2-1	Apollo 15 LM Descent Inertial Delta V (AGS-PGS)	2-11
2-2	Apollo 15 LM Descent Inertial Delta V (AGS-PGS)	2-13
2-3	Apollo 15 LM Descent Inertial Delta V (AGS-PGS)	2-15
2-4	Apollo 15 LM Descent Inertial Delta P (AGS-PGS)	2-17
2-5	Apollo 15 LM Descent Inertial Delta P (AGS-PGS)	2-19
2-6	Apollo 15 LM Descent Inertial Delta P (AGS-PGS)	2-21
2-7	Apparent Attitude Relationship Between PGNCS and AGS During Ascent	2-23
2-8	Apollo 15 Ascent Inertial Delta V (AGS-PGS)	2-25
2-9	Apollo 15 Ascent Inertial Delta V (AGS-PGS)	2-27
2-10	Apollo 15 Ascent Inertial Delta V (AGS-PGS)	2-29
3-1	AGS-PGNCS Altitude Difference	3-17
3-2	AGS-PGNCS Altitude Rate Difference	3-18
3-3	Apollo 15 LM Descent Integrated Body Rate	3-19
3-4	Apollo 15 LM Descent Integrated Body Rate	3-21
3-5	Apollo 15 LM Descent Integrated Body Rate	3-23
3-6	Apollo 15 LM Descent AGS-PGS Attitude Difference	3-25
3-7	Apollo 15 LM Descent AGS-PGS Attitude Difference	3-27
3-8	Apollo 15 LM Descent AGS-PGS Attitude Difference	3-29
3-9	Apollo 15 LM Descent AGS-PGS Integrated Body Rate Difference	3-31
3-10	Apollo 15 LM Descent AGS-PGS Integrated Body Rate Difference	3-33
3-11	Apollo 15 LM Descent AGS-PGS Integrated Body Rate Difference	3-35

ILLUSTRATIONS (CONTINUED)

	<u>PAGE</u>
3-12 Apollo 15 LM Ascent Integrated Body Rate	3-37
3-13 Apollo 15 LM Ascent Integrated Body Rate	3-39
3-14 Apollo 15 LM Ascent Integrated Body Rate	3-41
3-15 Apollo 15 LM Ascent AGS-PGS Attitude Difference	3-43
3-16 Apollo 15 LM Ascent AGS-PGS Attitude Difference	3-45
3-17 Apollo 15 LM Ascent AGS-PGS Attitude Difference	3-47
3-18 Apollo 15 LM Ascent AGS-PGS Integrated Body Rate Difference	3-49
3-19 Apollo 15 LM Ascent AGS-PGS Integrated Body Rate Difference	3-51
3-20 Apollo 15 LM Ascent Integrated Body Rate Difference	3-53
3-21 Apollo 15 LM Descent Delta VB (AGS-PGS)	3-55
3-22 Apollo 15 LM Descent Delta VB (AGS-PGS)	3-57
3-23 Apollo 15 LM Descent Delta VB (AGS-PGS)	3-59
3-24 Apollo 15 LM Ascent Delta VB (AGS-PGS)	3-61
3-25 Apollo 15 LM Ascent Delta VB (AGS-PGS)	3-63
3-26 Apollo 15 LM Ascent Delta VB (AGS-PGS)	3-65
4-1 Yaw SPS Gimbal Transient During TEI	4-14
4-2 CSM Y-Control Axis Rates and CDU Angles During CMC Program P20	4-15
4-3 CSM X-Control Axis Rates and CDU Angles During CMC Program P20	4-16
4-4 Vehicle Orientation	4-17
4-5 Error Cross-plot	4-18

ILLUSTRATIONS (CONTINUED)

		<u>PAGE</u>
4-6	Enlargement of Attitude Error Anomaly	4-19
4-7	Major Jet Firings	4-20
4-8	Comparison of Gimbal Angles and Commands During Anomaly	4-21
4-9	Apollo 15 RCS Propellant Consumption During Powered Descent	4-22

NOMENCLATURE

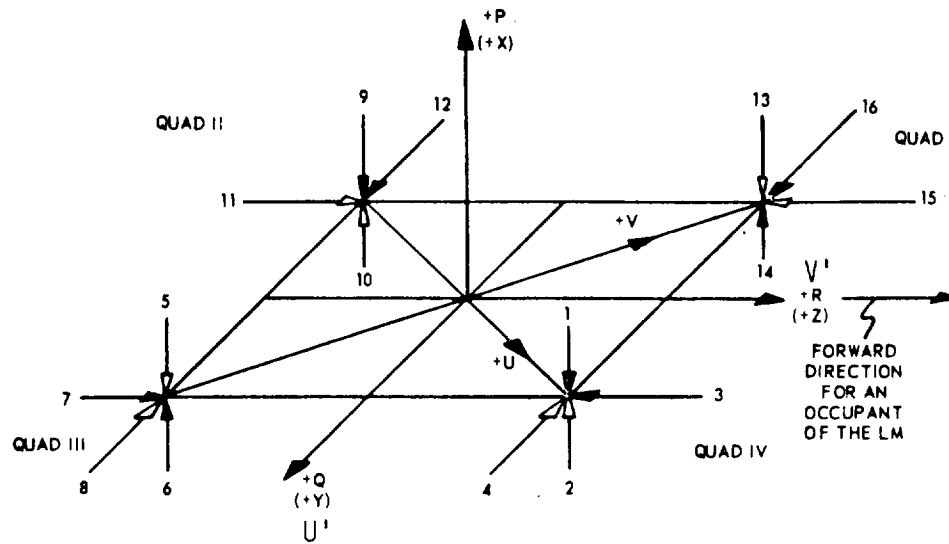
ACB (X, Y, Z)	Accelerometer bias (Channels X, Y, Z)
ADSRA (X, Y, Z)	Gyro drift due to acceleration along the spin reference axis (Channels X, Y, Z)
ADIA (X, Y, Z)	Gyro drift due to acceleration along the input axis (Channels X, Y, Z)
AGS	Abort Guidance System
AOT	Alignment Optical Telescope
APS	Ascent Propulsion System
ASA	Abort Sensor Assembly
CDU	Coupling Data Unit
CM	Command Module
CSM	Command and Service Module
CMC	Command Module Computer
DAP	Digital Autopilot
DC	Direction Cosine
DPS	Descent Propulsion System
DSKY	Display and Keyboard
EMS	Entry Montior System
EPC	Earth Prelaunch Calibration
FDAI	Flight Director Attitude Indicator
GDA	Gimbal Drive Actuator
GDC	Gyro Display Coupler
GET	Ground Elapsed Time (Range Time)
GN&C	Guidance, Navigation and Control
IFC	Inflight Calibration
IMU	Inertial Measurement Unit
IRIG	Inertial Rate Integrating Gyro
LGC	LM Guidance Computer
LM	Lunar Module
LR	Landing Radar
meru	Milli-Earth Rotational Units
MIT/CSDL	MIT/Charles Stark Draper Laboratory

NOMENCLATURE (CONTINUED)

MSC	Manned Spacecraft Center
MSFN	Manned Space Flight Network
NASA	National Aeronautics and Space Administration
NAV BASE	Navigation Base
NBD (X, Y, Z)	Gyro Bias Drift
Omega P'error	Rate error about P axis
Omega U'error	Rate error about U' axis
Omega V'error	Rate error about V' axis
ORB RATE	Orbital Rate
P error	Yaw axis error
PDI	Powered Descent Initiation
PGNCS	Primary Guidance, Navigation and Control System
PIC	Pre-Installation Calibration
PIPA	Pulsed Integrating Pendulous Accelerometer
PPM	Parts per Million
RCS	Reaction Control System
RSS	Root of the Sum of the Squares
S/C	Spacecraft
SCT	Scanning Telescope
SFE (X, Y, Z)	Scale Factor (Channels X, Y, Z)
SM	Service Module
SPS	Service Propulsion System
SIMBAY	Scientific Instrumentation Module Bay
TEI	Trans-Earth Insertion
TVC	Thrust Vector Control
U error	Computed Errors
U'error	Computed Errors
V error	Computed Errors
V'error	Computed Errors
w.r.t.	With Respect To
YACTOFF	Yaw Actuator Offset

NOMENCLATURE (CONTINUED)

YCMD	Yaw Gimbal Command
μg	Micro-gravities
P, U, V axis	DAP control axis oriented relative to LM body axes as shown below:



1. INTRODUCTION

1.1 PURPOSE

This report presents the detailed analyses of Apollo 15 Guidance, Navigation and Control equipment inflight performance. The analyses will supplement the discussions of CSM and LM GN&C performance presented in the Apollo 15 Mission Report (Reference 1).

1.2 SUMMARY

The Guidance, Navigation and Control Systems installed in the Apollo 15 spacecraft performed as expected with a few exceptions. In the CSM, significant SCT visibility degradation was observed as the result of fogging in the eye piece, the roll axis of the GDC would not align properly and the EMS scroll scribed intermittently during entry. In the LM, the AGS warning and master alarm lights falsely illuminated shortly after completion of LM ascent and the crew reported that the cross-pointer needles were not working during the braking phase of rendezvous. These hardware anomalies along with several procedural anomalies are discussed in the MSC Mission Report (Reference 1).

This report contains the results of additional studies which were conducted to confirm the conclusions of the MSC Mission Report and contains analyses which were not completed in time to meet the Mission Report deadline.

The LM IMU data were examined during the lunar descent and ascent phases. Most of the PGNCs descent absolute velocity error was caused by platform misalignments. PGNCs radial velocity divergence from AGS during the early part of descent was partially caused by PGNCs gravity computation differences from AGS. The remainder of the differences between PGNCs and AGS velocity were easily attributable to attitude reference alignment differences and tolerable instrument errors. For ascent the PGNCs radial

velocity error at insertion was examined. The total error of 10.8 ft/sec was well within mission constraints but larger than expected. Of the total error, 2.30 ft/sec was PIPA bias error, which was suspected to exist pre-lunar liftoff. The remaining 8.5 ft/sec is most probably satisfied with a large pre-liftoff platform misalignment. A gravity anomaly at the landing site deflected the IMU measurement of gravity away from the landing site radius vector resulting in a misalignment about the Y platform axis (-295 sec) which was approximately 1.7 times expected maximum. It appears that IMU sensor performance was acceptable.

Detailed studies of the CSM DAP were required to investigate a SPS gimbal transient during the TEI maneuver and a comprehensive study of SIMBAY pointing in lunar orbit was conducted to investigate unexpected long duration RCS jet firings. The gimbal transient was the result of a PGNCS CDU transient and the unexpected RCS firings were the result of a software anomaly. The software anomaly will be resolved on the following missions with procedure changes. The CDU transient problem has been observed before in coasting flight but this was the first time it was observed in powered flight. In either case no detrimental effects have occurred or are expected. No corrective action is planned.

Detailed error separation studies of the AGS Abort Sensor Assembly indicated excellent performance of the accelerometers and gyros during coasting and powered flight.

2.0 LM IMU PERFORMANCE

LM IMU performance was examined for both coasting and powered flight. Results were acceptable. Residual gyro drift measurements (differences between the total gyro drift and the LGC compensation being applied) based on the alignments performed are presented in Table 2.1. The two sets of drift values calculated while the LM was in coasting flight are direct measures of residual gyro drift and are directly comparable to the one sigma specification value of two meru. The first P57 includes primarily coasting flight drift and will be evaluated against the coasting flight criteria. All of the nine values fall within or quite close to the two meru limit. All subsequent drift errors were calculated using the P57 data while the LM was on the lunar surface. Different limits for the X gyro are applicable since while on the surface, the input axis acceleration sensitive drift must also be considered. Only one surface drift value varied significantly from the expected 1σ value, that being the final P57 Z gyro residual drift measured prior to liftoff. However, the 1σ uncertainty in the alignment technique about the Z axis is 0.023 degrees which results in an uncertainty of 1.15 meru for the Z drift measurement in question. Indications are, the gyros were performing within acceptable limits during coasting flight and while on the surface.

PIPA bias calculations based on coasting flight data and lunar surface data are presented in Table 2.2. The accelerometer instruments showed excellent stability during coasting and across powered flight periods. Across the shutdown period on the lunar surface, the X and Y instrument biases shifted by 0.39 and 0.46 cm/sec² respectively which is expected. For the first time, the biases were updated on the lunar surface and the biases remained stable for the remainder of the LM active periods. After ascent to lunar orbit, the Z instrument compensation was changed to adjust for a small shift which occurred before PDI and the X compensation was adjusted to agree more closely with the post powerup bias measured on the lunar surface.

2.1 DESCENT PERFORMANCE

IMU performance during the descent period was based on assessment of a PGNCs inertial velocity state at touchdown which was independent of the landing radar data and comparisons of the PGNCs thrust and total velocities with AGS data during descent. The PGNCs touchdown vector was obtained by integrating the incremental thrust accelerations, recovered from telemetry, to the time of touchdown. The trajectory was initialized 20 seconds prior to ullage using the onboard state vector. The resultant inertial velocity and the true inertial velocity at the landing site are shown below:

<u>SM Coordinates</u>	<u>PGNCs Inertial Velocity without Radar Updating</u>	<u>True Inertial Velocity at Landing Site</u>	<u>ΔV (Ft/Sec) PGNCs-TRUE</u>
X	4.67 ft/sec	0 ft/sec	4.67
Y	5.22 ft/sec	3.05 ft/sec	2.17
Z	-15.01 ft/sec	-13.25 ft/sec	-1.76

A set of IMU errors which force the PGNCs data to agree more closely with the true inertial velocity at the landing site is shown below:

<u>Error Source</u>	<u>Value</u>	<u>Ratio Flight/Preflight</u>	<u>Contribution (Ft/Sec)</u>		
			<u>ΔV_x</u>	<u>ΔV_y</u>	<u>ΔV_z</u>
ACBX	40 μg	0.2	0.99		
ACBY	-10 μg	0.05		-0.25	
ACBZ	-110 μg	0.6			-2.75
ϕ_y	134 $\widehat{\text{sec}}$	0.7	3.67		1.50
ϕ_x	- 89 $\widehat{\text{sec}}$	0.4		2.42	
			<u>Σ 4.66</u>	<u>2.17</u>	<u>-1.25</u>

Accelerometer bias errors (ACBX, Y, Z) in the error set are those residual biases measured pre-PDI and noted in Table 2.2.⁽¹⁾ The platform misalignment angles ϕ_y and ϕ_x are acceptable for an inflight alignment and are less than one sigma errors as noted by the column referencing the inflight value to the preflight estimate.

⁽¹⁾ $1 \text{ CM/sec}^2 = 1000 \mu g$

A further assessment of the PGNCS performance is based on the comparison of PGNCS onboard state vectors with the AGS onboard state vectors. Figures 2-1 through 2-3 present AGS minus PGNCS total inertial velocity differences and Figures 2-4 through 2-6 show the AGS minus PGNCS total inertial position differences. The plot of primary interest is Figure 2-1 showing ΔV_x which is essentially altitude rate. The plot shows a divergence starting at PDI with an increasing rate starting at the time landing radar altitude updates begin. The divergence continues until landing radar altitude rate updates begin at which time, the divergence is stopped and the difference begins to decrease. Indications are, the AGS altitude rate estimate is better than PGNCS before landing radar updates start, after which time the PGNCS was driven back toward the AGS estimate of altitude rate. In order to isolate the cause for the divergence, differences between AGS and PGNCS were computed in the thrust velocity domain, i.e., AGS sensed velocity minus PGNCS sensed velocity independent of gravity. These differences are shown as dashed lines in Figure 2-1 through 2-3, and indicate that for ΔV_x , the inertial instruments account for about half of the divergence observed in the total differences. For ΔV_y and ΔV_z , almost all of the total velocity divergence before start of radar updating is directly accountable to sensed velocity differences, i.e., minimal gravity effects. The ΔV_z sensed difference between AGS and PGNCS is primarily the result of the PGNCS bias error which was previously discussed coupled with some AGS/PGNCS attitude misalignments. The ΔV_y sensed difference is primarily attitude misalignment between the AGS inertial reference and PGNCS IMU attitude. AGS errors are discussed in Section 3 of this report. Explanation of total ΔV_x is now explained in two parts; (1) gravity effects and (2) sensor differences.

1) ΔV_x Gravity Effects

Both AGS and PGNCS computers calculate gravity effects during powered flight using a spherical gravity model which is expressed as:

$$\underline{g} = -\frac{\mu m}{r^2} \underline{u}_r$$

where μ_m = moon gravitational constant
 \underline{u}_r = unit vector in direction of \underline{r}
 \underline{r} = radius vector

For this discussion, \underline{u}_r is effectively along the X inertial direction, so the expression will be simplified to:

$$g_x = - \frac{\mu_m}{r^2}$$

Prior to landing radar altitude updating, the PGNCS and AGS gravity effects are different because each computer is using a different value for μ_m .

$$\text{PGNCS } \mu_m = 0.173139 \times 10^{15} \text{ ft}^3/\text{sec}^2$$

$$\text{AGS } \mu_m = 0.173188 \times 10^{15} \text{ ft}^3/\text{sec}^2$$

The difference in μ_m results in a velocity computation difference (AGS-PGNCS) of $\Delta V_x = -0.3$ ft/sec at start of altitude update. This value plus the sensed error resolves the differences between AGS and PGNCS at the start of LR altitude updating. After altitude updating starts, the X velocity difference begins to diverge at a faster rate. PGNCS position state vector updating using radar data is adjusted onboard to account for terrain variations under the spacecraft. The terrain variations are modeled preflight and are stored in the computer. Postflight analysis (Reference 2) has shown that the terrain was modeled in error, and the effect was, to introduce an error into the PGNCS position state each time a radar measurement was incorporated. The terrain model coming into closer agreement with the actual terrain features later on in descent along with altitude rate measurements from the radar prevented this modeling error from having any significant effect on the LM landing. However, the earlier effect was, to drive the PGNCS position state away from the AGS position state and this is easily observable from Figure 2-4. The large difference in ΔR_x at start of altitude updating caused further difference in the computation of gravity effects by AGS and PGNCS. Between the first altitude

update and start of altitude rate update, the ΔR_x difference caused a velocity difference of -0.91 ft/sec. In addition, the μm difference contributed an additional -0.52 ft/sec yielding a total ΔV_x velocity difference due to gravity effects of -1.43 ft/sec. The gravity effects plus the sensed velocity error resolves the difference between AGS and PGNCs at the start of altitude rate updating to within -0.37 ft/sec which is within the noise level of the data being utilized.

2) ΔV_x Sensor Differences

The sensed difference between AGS and PGNCs can easily be satisfied due to the PGNCs accelerometer bias errors, known misalignment between the AGS inertial reference and PGNCs IMU attitude and AGS accelerometer errors. PGNCs accelerometer errors have been previously discussed and AGS attitude and accelerometer errors will be discussed in Section 3 of this report.

In conclusion, the IMU performance during descent was acceptable and only about half of the divergence between PGNCs and AGS altitude rate is attributable to sensor errors. The gravity effects as the result of PGNCs terrain modeling error and differences between PGNCs and AGS moon gravitational constant caused the remainder of the altitude rate divergence.

2.2 ASCENT PERFORMANCE

For ascent, the PGNCs insertion vector was corrected for (1) known accelerometer bias errors which existed during ascent (noted in Table 2.2) and (2) corrected for the best estimate landing site vector. The PGNCs vector was subsequently compared with a postflight established MSFN vector. The AGS insertion vector was also compared with the MSFN vector and the comparisons are presented below:

<u>Difference</u>	<u>$\Delta \dot{X}$ (Radial) (Ft/Sec)</u>	<u>$\Delta \dot{Y}$ (Cross-range) (Ft/Sec)</u>	<u>$\Delta \dot{Z}$ (Down-range) (Ft/sec)</u>
PGNCs-MSFN	8.49	-8.31	-0.72
AGS-MSFN	3.24	-10.08	0.43

A set of IMU errors which will fit the PGNC absolute insertion velocity error is shown below:

<u>Error Source</u>	<u>Value</u>	<u>Ratio Flight/Preflight</u>	<u>Contribution</u>		
			<u>ΔV_x</u>	<u>ΔV_y</u>	<u>ΔV_z</u>
SFEX	116 ppm	1 σ	0.13		
NBDY	-0.03°/hr	1 σ	0.20		
ADSRAY	-0.075°/hr/g	1 σ	0.14		
ϕ_y	-295 $\widehat{\text{sec}}$	5 σ	8.00		-1.60
ϕ_x	-305 $\widehat{\text{sec}}$	2 σ		-8.31	
			<u>Σ 8.47</u>	<u>-8.31</u>	<u>-1.60</u>

The ϕ_x misalignment error conveniently satisfies the ΔV_y and the size of the misalignment is consistent with predicted uncertainties. The ϕ_y error appears to be the most reasonable fit for the large ΔV_x , but the misalignment is inconsistent with preflight estimates. As shown in the table above, when the ϕ_y is selected to totally account for ΔV_x , approximately 1 ft/sec residual remains in ΔV_z , the downrange direction. However, MSFN has the greatest uncertainty in the Z direction which could easily account for the poor velocity match in that direction. The reasons for selection of Y misalignment to fit the end point errors are as follows:

- 1) As the above table reveals, contribution to ΔV_x for one sigma scale factor (XSF) and gyro drift (YGCDR and YADSR) errors are extremely small. Large instrument errors would be required to account for the 8.49 ft/sec X velocity error; an error which would suggest a failed instrument. Free-fall data acquired pre-PDI and post insertion, lunar surface data and lunar ascent data reflects good performance of the accelerometers and gyros thus contradicting a failed instrument hypothesis.
- 2) Postflight studies have been conducted to assess the IMU attitude errors prior to liftoff and these studies also give indications of misalignments larger than preflight estimates. The studies used AOT star sighting data acquired while on the lunar surface to determine LM body attitude. Multiple AOT star sightings were processed in a weighted least squares estimator to determine the best

estimate of LM body attitude with respect to a moon-fixed local level coordinate system. Gravity vector measurements obtained at the time of the AOT sightings were also used in order to detect and compensate for LM tilting between batches of AOT sightings. Once the body attitude was determined, the gimbal angles at a specific time were used to determine the IMU orientation at the time in question. The computed and the desired platform orientations were then compared to determine misalignments. The IMU orientation was computed after completion of the final P57 and results indicated the following platform misalignments.

$$\begin{aligned}\Delta\theta_x &= -144 \widehat{\text{sec}} \\ \Delta\theta_y &= -180 \widehat{\text{sec}} \\ \Delta\theta_z &= 180 \widehat{\text{sec}}\end{aligned}$$

Maximum expected (3σ) gravity/star alignment errors computed pre-flight were 445, 169 and 260 arc seconds respectively for X, Y and Z. The abnormally large error about the Y axis is thought to be caused by a gravity anomaly at the landing site which deflected the PGNCS gravity measurement away from the true local vertical. The liftoff error is conceivably larger than the estimate above, because some uncertainty exists in the method used ($+ 40 \widehat{\text{sec}}$) and the IMU drifted for approximately 40 minutes before liftoff occurred. The large Y axis misalignment at first observation appears to contradict the 0.03 degree star angle difference (Noun 5) computed onboard at the time of the alignment. However, review of the P57 measurement geometry reveals that a Y axis misalignment is not totally contained in the N05 value. For the P57 alignment, the vehicle was setting with the Z body axis pointing 5 degrees north of the CSM orbit plane and the right hand detent was used for the star measurement. As a result the plane which contains the star and gravity vector is 65 degrees away from the orbit plane. The star angle difference calculation measures primarily those errors in the plane containing the star and gravity vectors. Errors perpendicular to the plane go undetected. Since the final alignment errors perpendicular to the plane are in fact about the Y axis, the Noun 05 measurement will not totally represent the true $\Delta\theta_y$.

- 3) The large difference between PGNCS and AGS error in the radial direction additionally cast some suspicion on the PGNCS and at first observation suggests a problem in the PGNCS X axis. If a PGNCS initial alignment caused the radial error

because of a gravity anomaly, the AGS should reflect a similar error, since it also uses gravity for performing its pre-lift-off alignment. Proof of this hypothesis is evident from Figure 3-16 in Section 3, where actual difference between AGS and PGNCS attitude are presented. The plot shows AGS attitude relative to PGNCS attitude in body coordinates. For ascent, the relationships between body differences and inertial attitude differences are $\Delta\theta_{XI} = \Delta\theta_{ZB}$, $\Delta\theta_{YI} = -\Delta\theta_{YB}$ and $\Delta\theta_{ZI} = -\Delta\theta_{XB}$.

Therefore from Figure 3-16 it can be seen that the AGS starts out with a pre-lift-off misalignment from PGNCS of 80 arc seconds. But further study of the same figure shows that the AGS continued to diverge away from PGNCS throughout the course of the burn. The sketch in Figure 2-7 clarifies the following remarks. PGNCS was apparently misaligned about Y pre-lift-off by a significant amount. AGS/PGNCS attitude data shows that AGS was within 80 $\overline{\text{sec}}$ of PGNCS at the same time but misaligned in a direction toward the true inertial. In the course of the burn, the AGS attitude reference continued to diverge toward the true inertial. The AGS attitude reference apparent drift is primarily the result of ASA misalignments in conjunction with the significant body maneuvers which are performed during ascent. The end result is, an AGS measured inertial velocity which is better than PGNCS. Further proof is obtained when AGS-PGNCS sensed velocity differences in inertial space are derived and plotted in Figures 2-8 through 2-10. As shown, the largest sensed error is in the X direction, and this sensed difference between AGS and PGNCS can be satisfied with a 140 $\overline{\text{sec}}$ misalignment about Y. Review again of Figure 3-16 shows an average inertial attitude misalignment between AGS and PGNCS of 140 $\overline{\text{sec}}$.

- 4) Review of lunar gravity modeling studies¹ confirmed a large offset of the "g" vector at the Hadley Rille Site when mascon effects are considered. When a L1 potential model was modified with mascon effects at the nominal landing site, the gravity vector shifted .019 degrees to the north and 0.108 degrees to the west. The primary effect on a platform aligning to the "g" vector for a westerly flight azimuth would be to tilt the vertical axis downrange. For the A-15 mission, this is equivalent to a -390 $\overline{\text{sec}}$ misalignment about the platform y axis.

In summary, the most reasonable explanation for the PGNCS radial error at insertion is platform misalignment. From available data it appears that IMU sensor performance was acceptable and the large pre-lift-off Y misalignment was the result of inappropriate lunar potential modeling, not hardware error.

¹ MSC Memo FM4 (71-97), Apollo 15 Lunar G, dated July 9, 1971

Table 2.1. Gyro Drifts

Type	GET Hr:Min	Corrective Torquing	Time Lapse (Hours/Min)	Torquing Angles (Degrees)			Residual (1) Drift Rates Meru			Residual Drift Limit (Meru)
				X	Y	Z	X	Y	Z	
P52#1 (Coast)	99:11 (Rev. 11)	Yes	N/A	--	--	--	--	--	--	
P52#2 (Coast)	101:16 (Rev. 12)	Yes	2:04	-.002	+ .076	-.046	.06	-2.36	-1.43	+2
P52#3 (Coast)	103:00 (Rev. 13)	Yes	1:44	-.010	+ .023	-.034	.38	-.88	-1.31	+2
P57#1 (Pre-power down)	105:07	No	2:07	-.011	-.041	-.002	+.34	+1.28	-0.06	+2
P57#2 (Pre-power down)	105:23	Yes	2:23	-.075	+ .058	-.060	2.10	-1.62	-1.68	+2 (Y&Z) +2.4 (X)
P57#3 (Pre-power down)	105:47	Yes	--	-.008	-.021	-.033	(insufficient ΔT)			
P57#4 (Post-power up)	169:38	Yes	--	-.083	+ .006	+ .028	(not valid-system was shutdown)			
P57#5 (Post-power up)	170:59	Yes	1:21	+ .021	+ .012	-.057	-1.04	-0.59	-2.81	+2 (Y&Z) +2.4 (X)

Note (1): Change from prelaunch load compensation values of:

NBDX = 3.20 meru
 NBDY = -0.70 meru
 NBDZ = 1.40 meru

Table 2.2 Accelerometer Biases

Time Period	Source	Result (cm/sec ²)			Bias Shift From Compensation			Bias Shift Limit (cm/sec ²)
		X	Y	Z	X	Y	Z	
Prelaunch	Mean of KSC Calibrations	1.71	1.42	1.42	-	-	-	
Prelaunch	Flight load	1.70	1.41	1.42	-	-	-	
Pre-PDI (100:59)	Coast monitoring	1.72	1.40	1.43	.02	-.01	.01	+0.2
Pre-PDI (104:12)	Coast monitoring	1.74	1.40	1.31	.04	-.01	-.11	+0.2
Pre-Ascent	Surface monitoring	2.09	1.87	1.29	.39	.46	-.13	N/A
Pre-Ascent	New flight load	(1.90)	(1.75)	1.42	-	-	-	
Post-Insertion	Coast monitoring	2.03	1.74	1.27	.13	-.01	-.15	+0.2
Post-Insertion	Coast monitoring	2.06	1.82	1.26	.16	.07	-.16	+0.2
Post-Insertion	New flight load	(2.06)	1.75	(1.26)	-	-	-	

() Indicates value changed from previous flight load

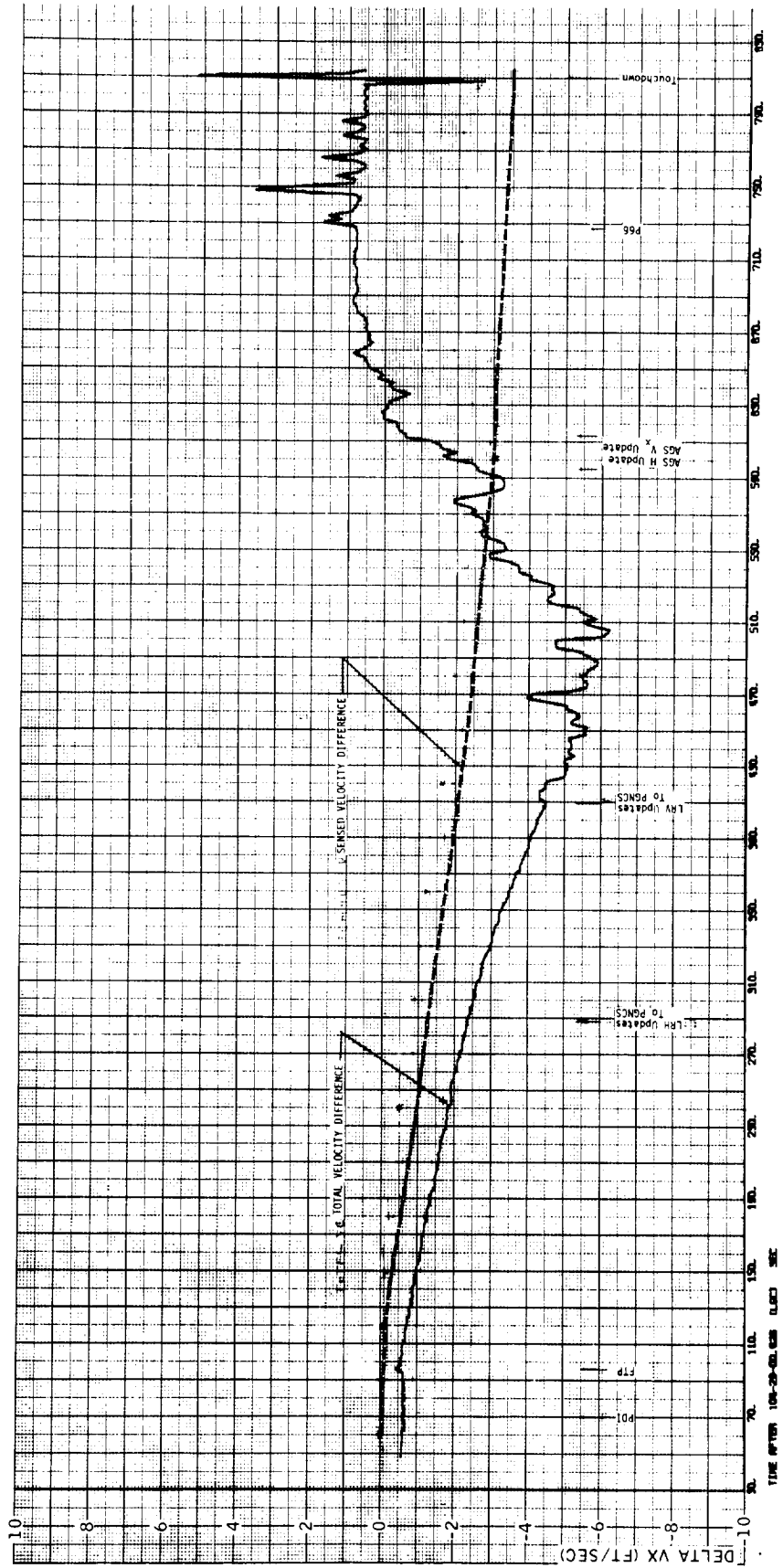


FIGURE 2-1. APOLLO 15 LM DESCENT
INERTIAL DELTA V (AGS-PGS)

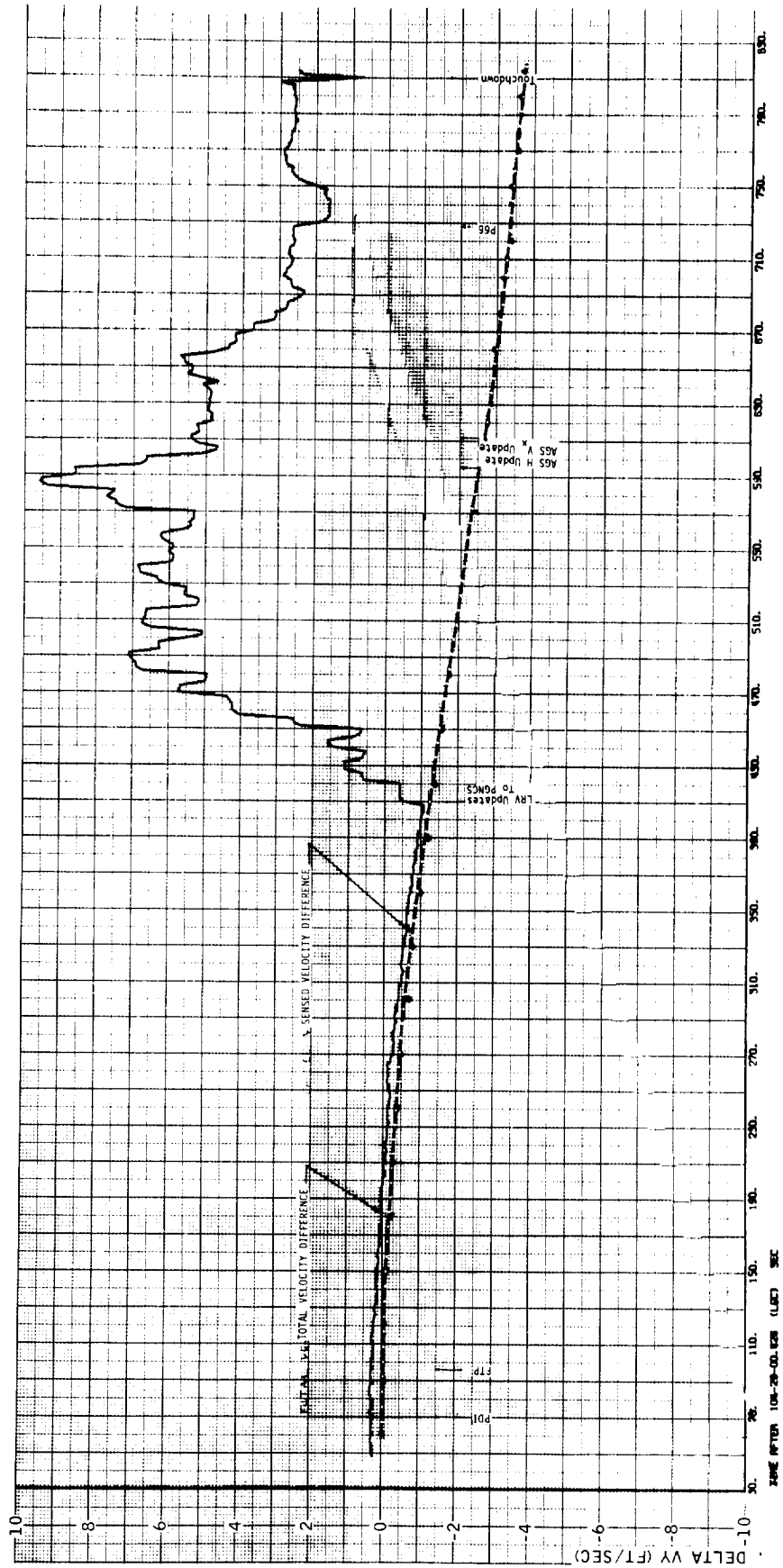


FIGURE 2-2. APOLLO 15 LM DESCENT
INERTIAL DELTA V (AGS-PGS)

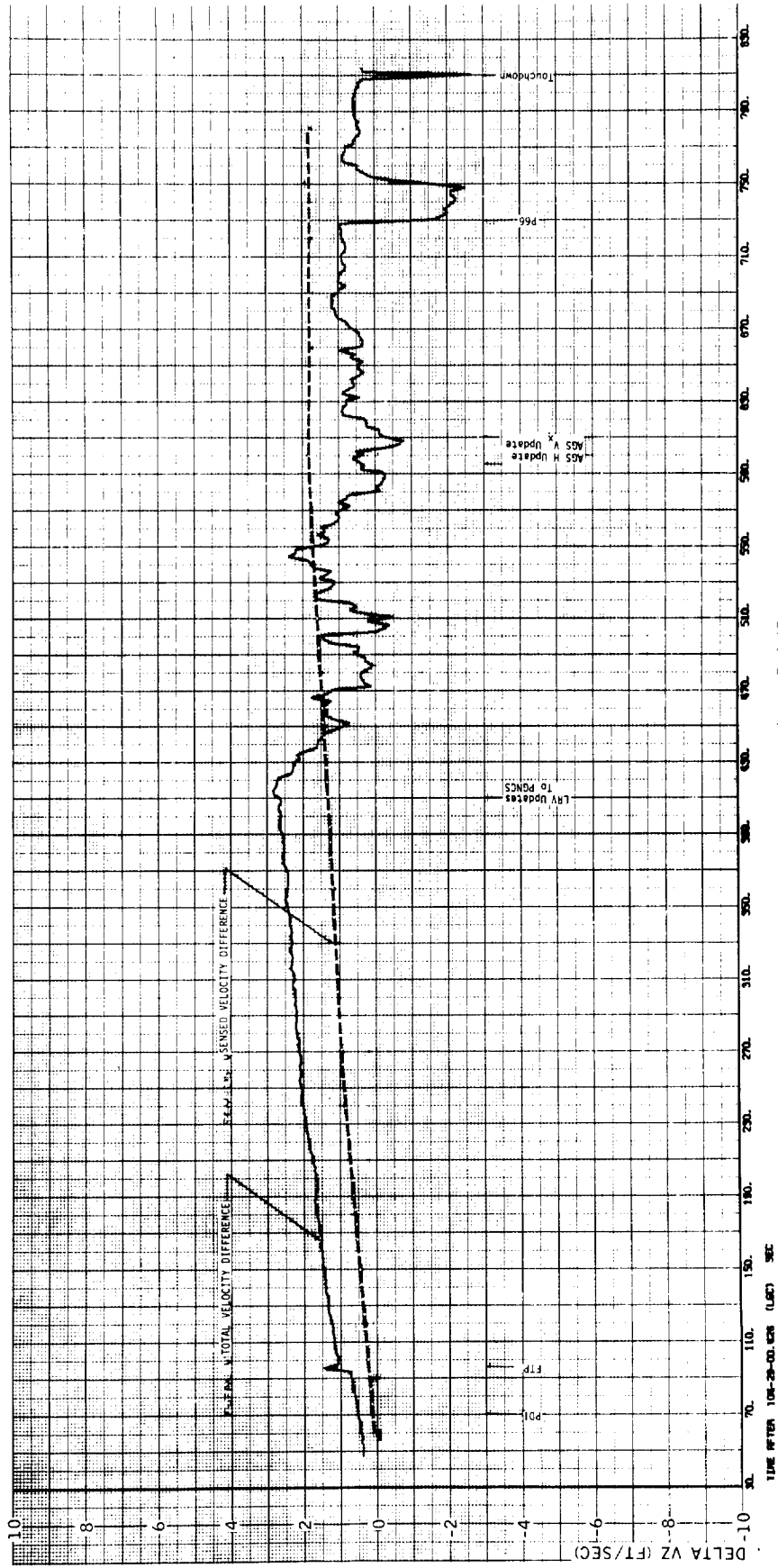


FIGURE 2-3. APOLLO 15 LM DESCENT
INERTIAL DELTA V (AGS-PGS)

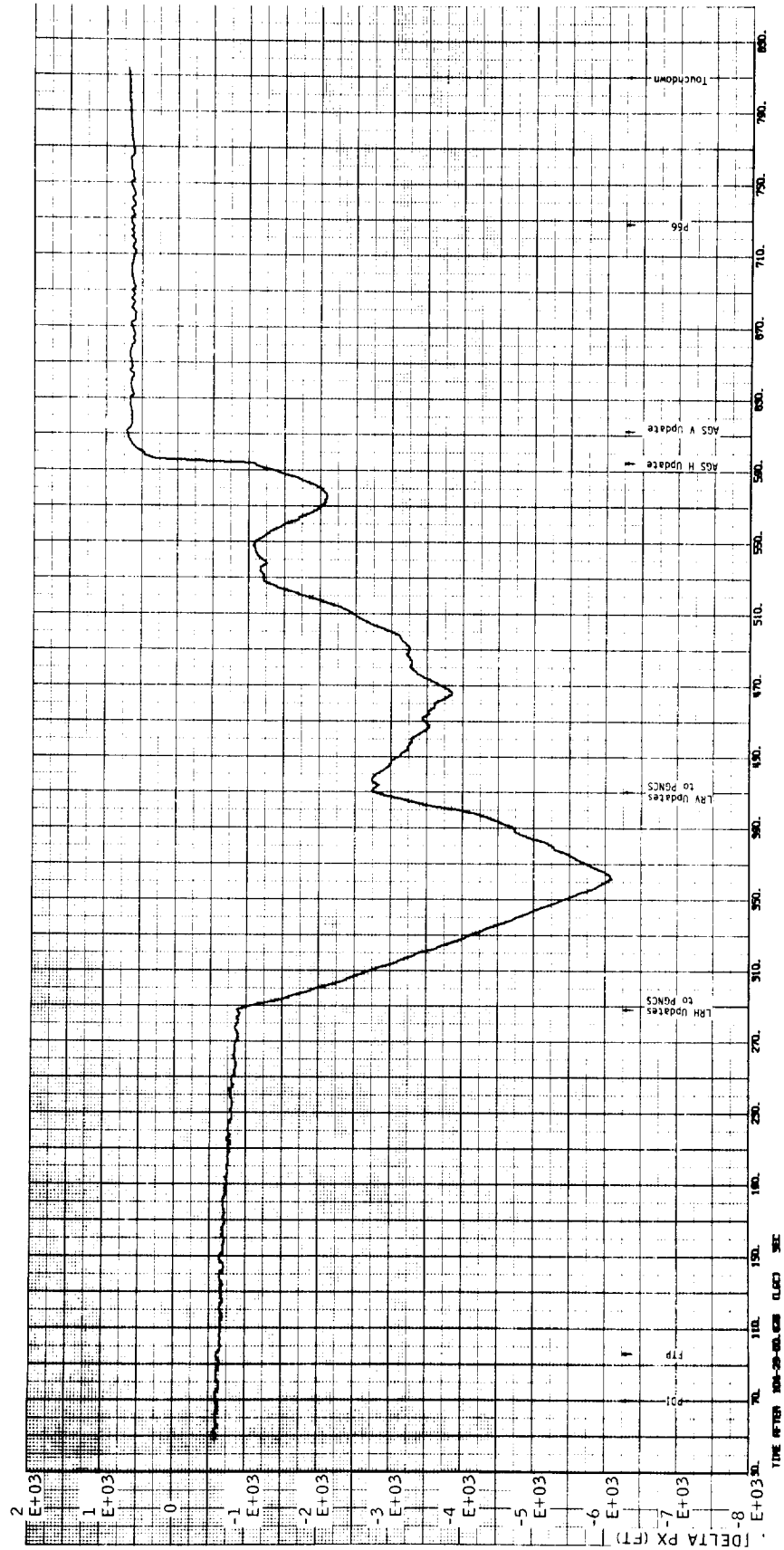
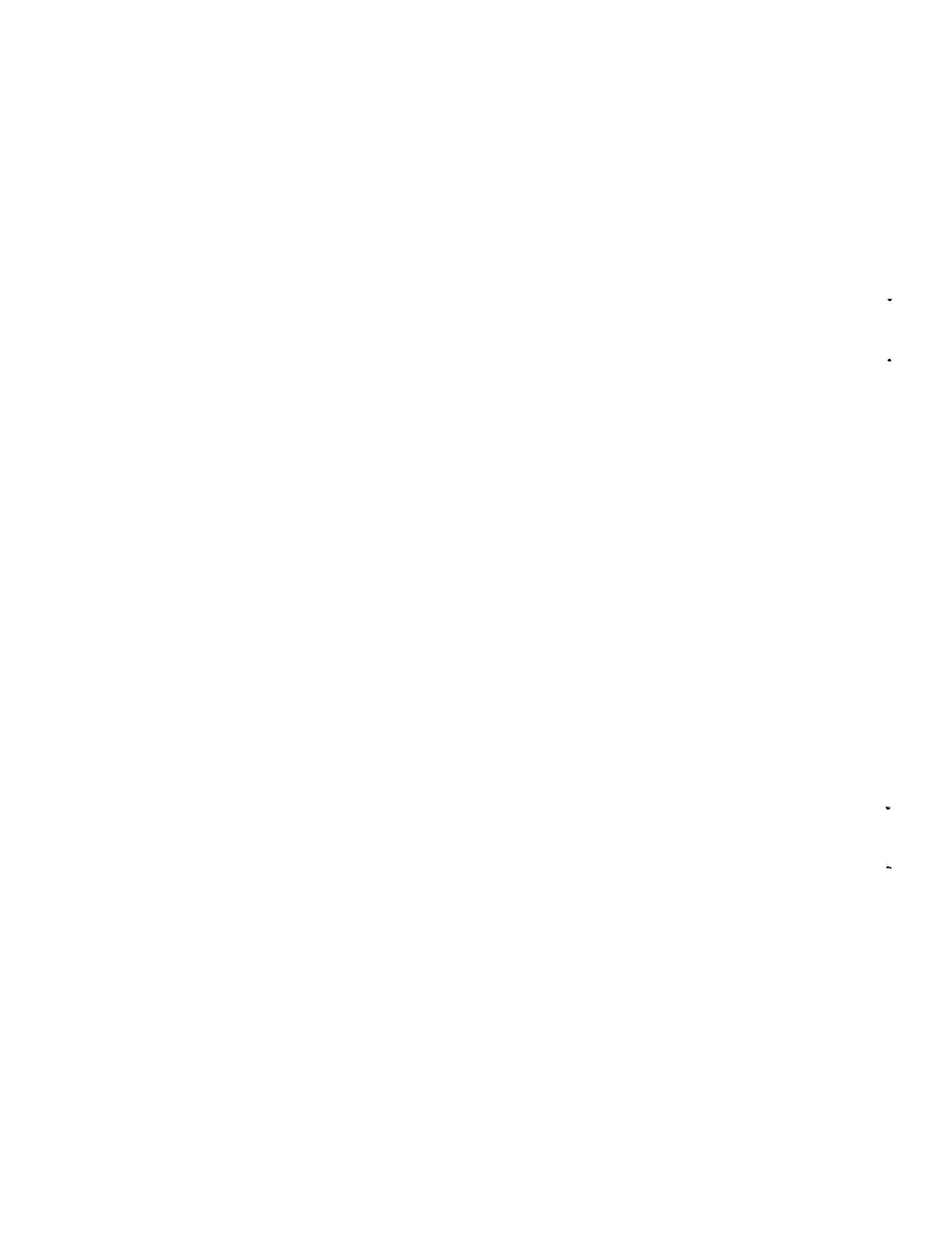


FIGURE 2-4. APOLLO 15 LM DESCENT
INERTIAL DELTA P (AGS-PGS)



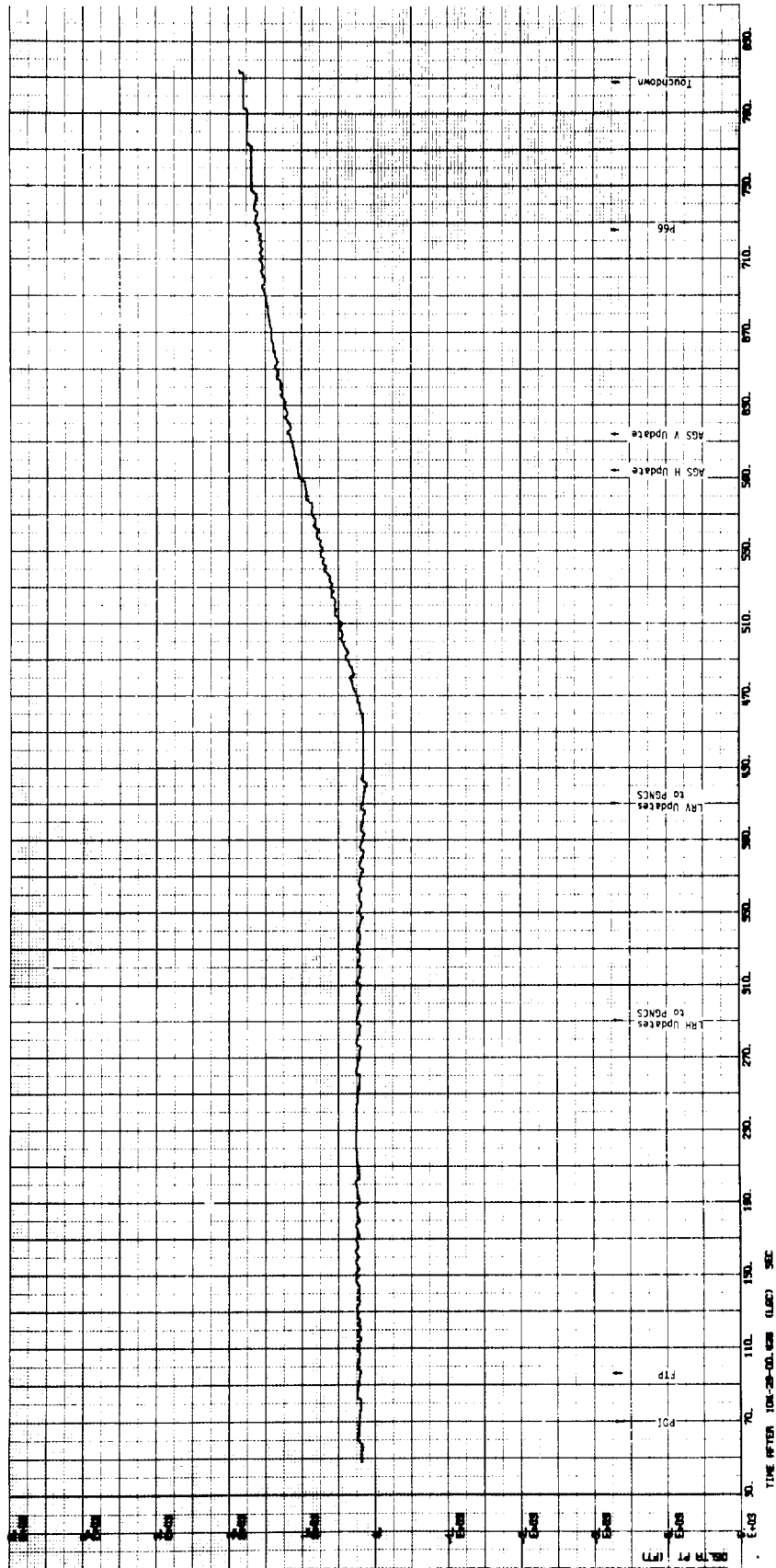


FIGURE 2-5. APOLLO 15 LM DESCENT
INERTIAL DELTA P (AGS-PGS)

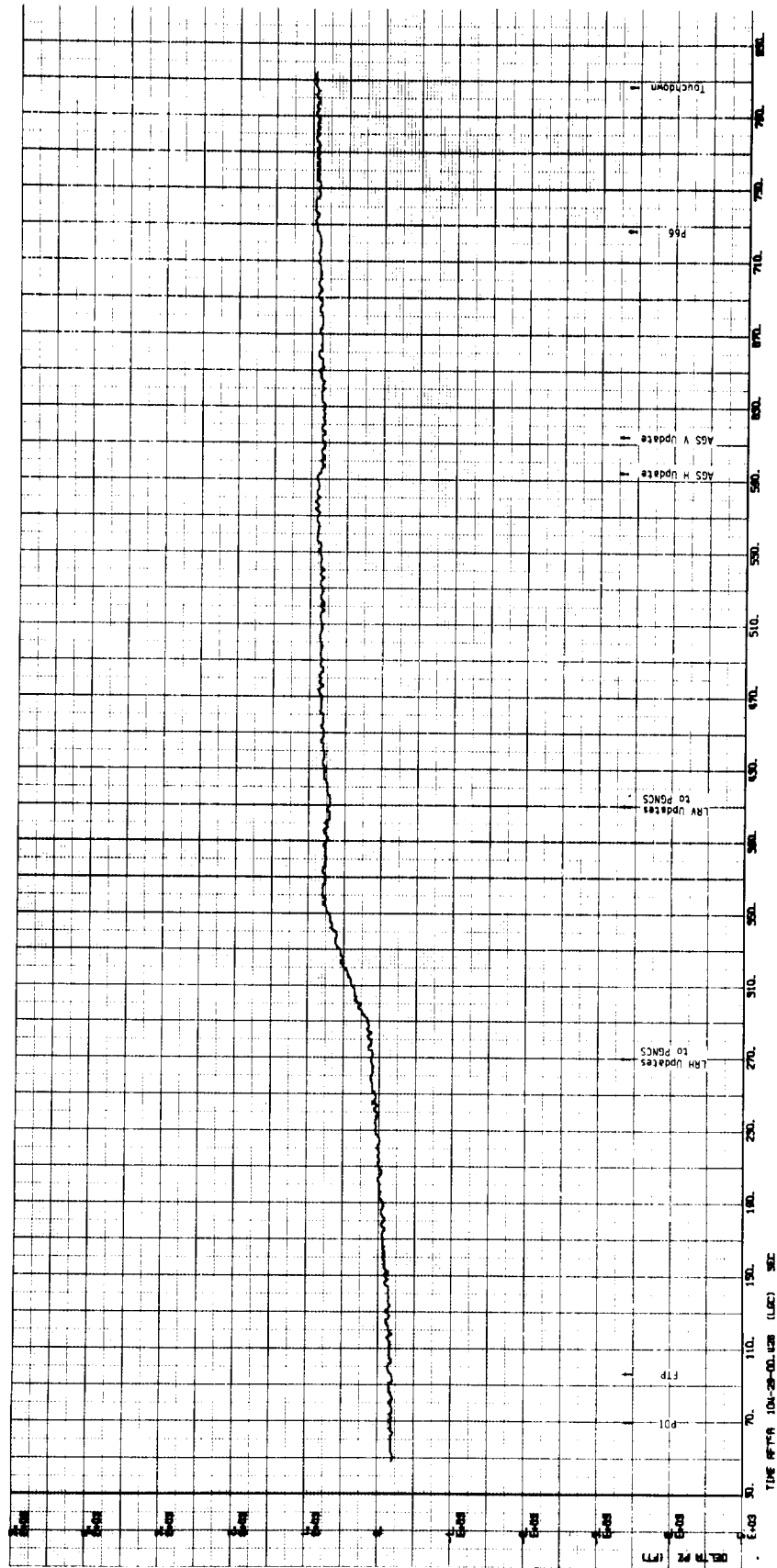
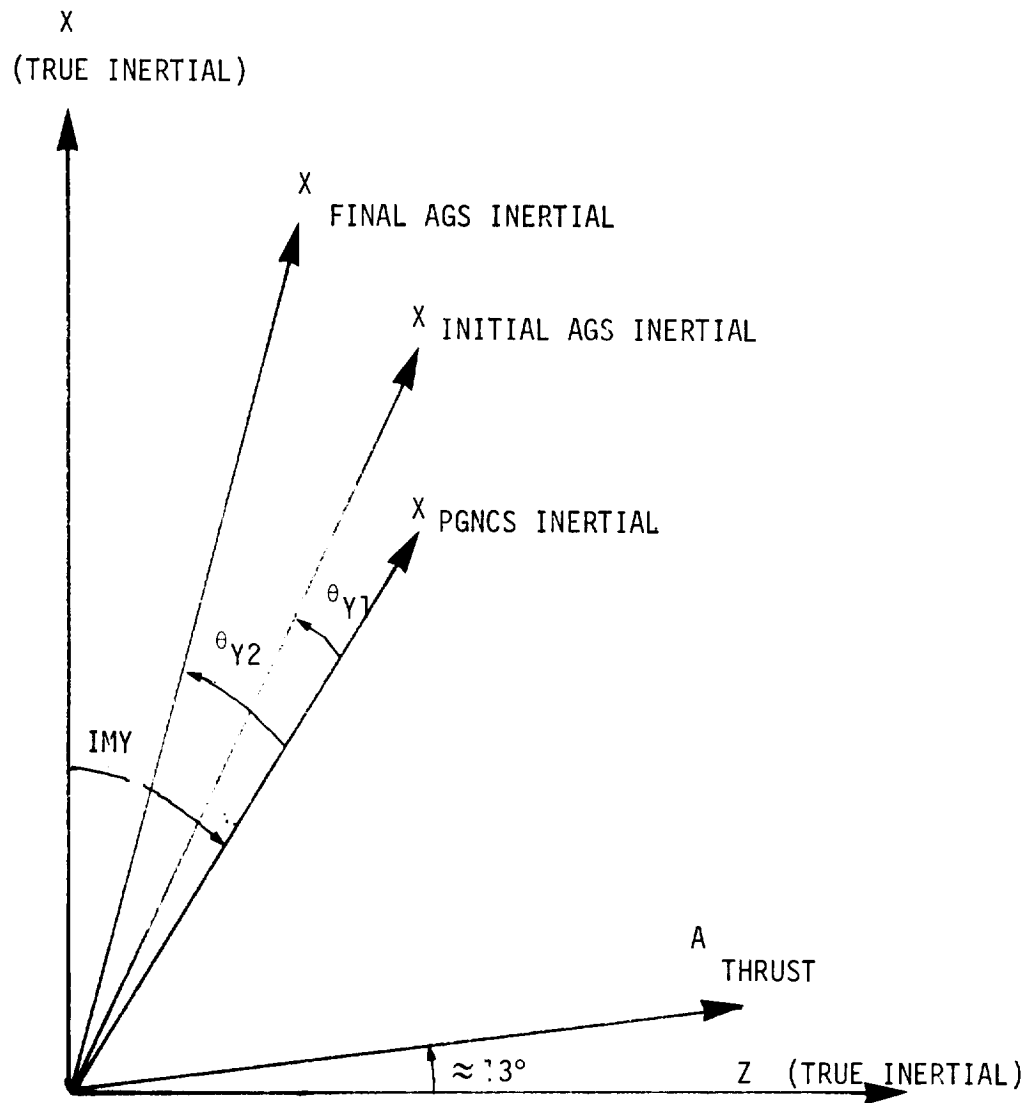


FIGURE 2-6. APOLLO 15 LM DESCENT
INERTIAL DELTA P (AGS-PGS)



IMY = Initial PGNCS misalignment ($-295 \widehat{\text{sec}}$)

θ_{Y1} = AGS initial misalignment from PGNCS ($80 \widehat{\text{sec}}$)

θ_{Y2} = AGS final misalignment from PGNCS ($140 \widehat{\text{sec}}$)

Figure 2-7. Apparent Attitude Relationship Between PGNCS and AGS During Ascent

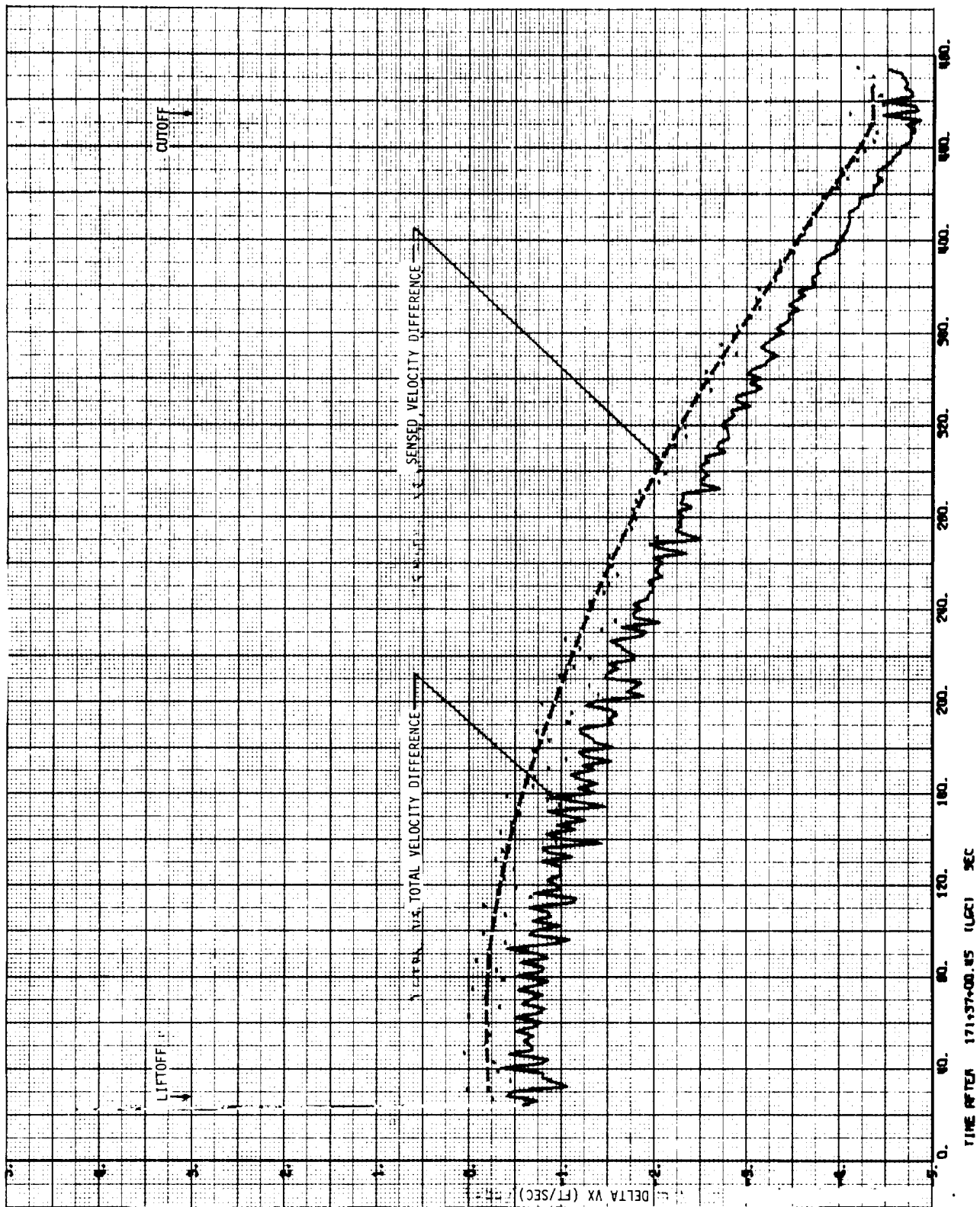


FIGURE 2-8. APOLLO 15 ASCENT INERTIAL DELTA V (AGS-PGS)

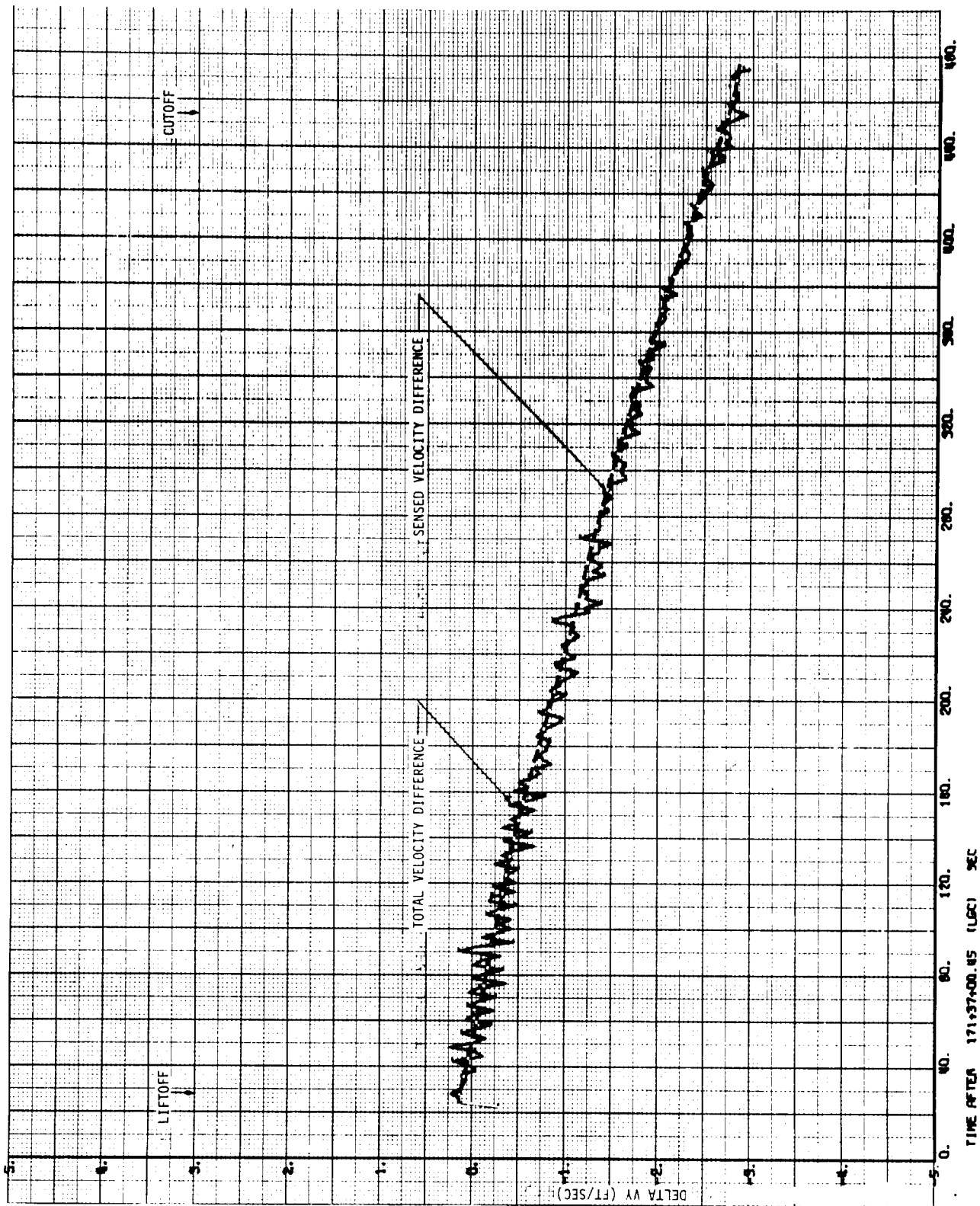


FIGURE 2-9. APOLLO 15 ASCENT INERTIAL DELTA V (AGS-PGS)

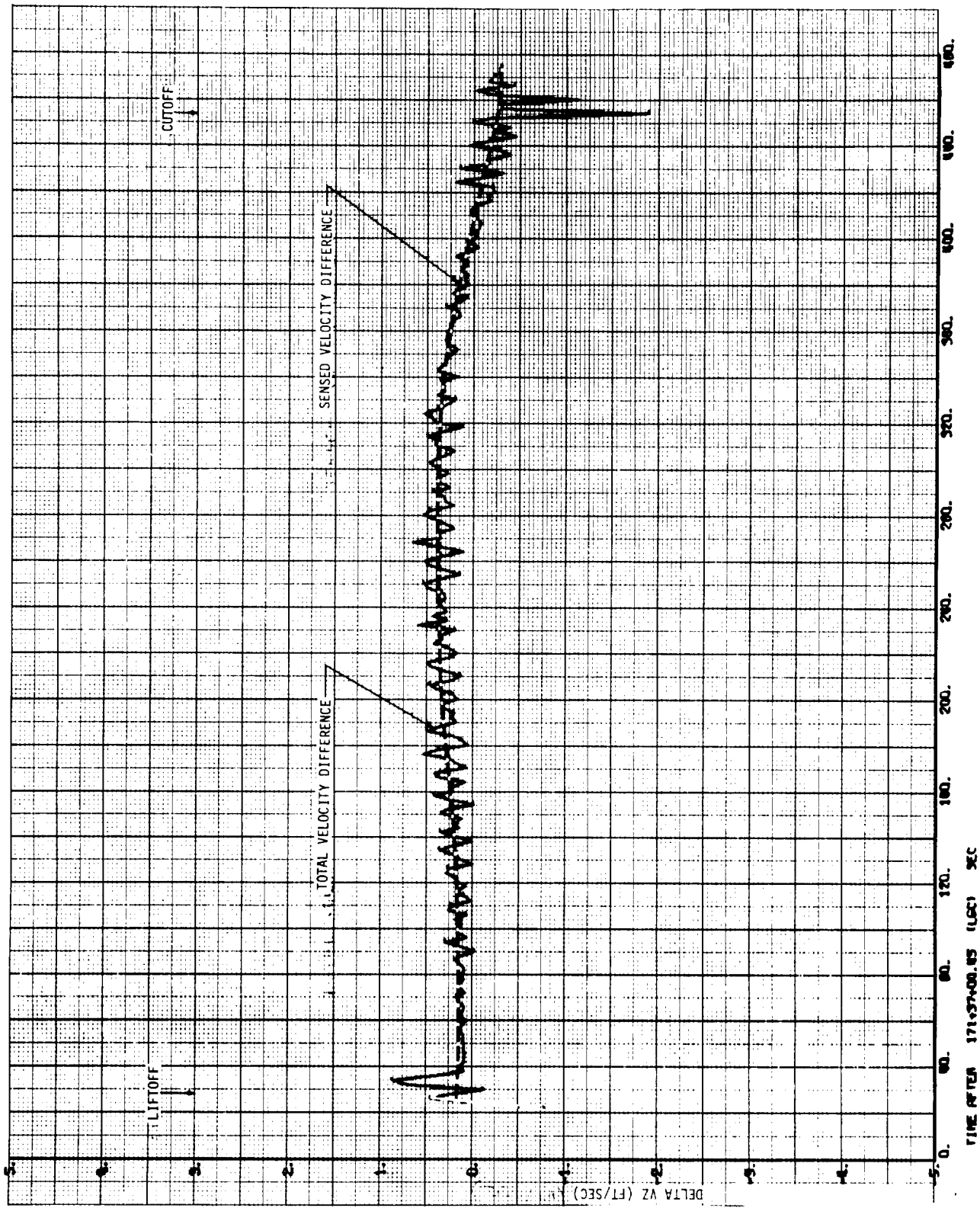


FIGURE 2-10. APOLLO 15 ASCENT INERTIAL DELTA V (AGS-PGS)

3.0 LM AGS PERFORMANCE

3.1 Altitude and Altitude Rate Update During Descent

Apollo 15 was different from previous missions in that altitude and altitude rate updates were executed during powered descent while only altitude updates were performed on previous missions. The AGS minus PGNCs altitude and altitude rate differences for pertinent times during the descent are summarized below:

	<u>Pre-Altitude Update</u>	<u>Post-Altitude Update</u>	<u>Pre-Velocity Update</u>	<u>Post-Velocity Update</u>	<u>Touchdown</u>
Δh (ft)	-1018	368	616	616	678
$\dot{\Delta h}$ (ft/sec)	2.4	-2.4	-1.6	-1.0	0.5

The differences throughout descent are plotted in Figures 3-1 and 3-2. The 368 foot error in altitude remaining after the altitude update is the result of a 1.8 second time delay in executing the update, approximately the same size execution error as observed on previous missions. The altitude rate update had little effect on the AGS velocity vector since the AGS was maintaining an accurate velocity trajectory before the update.

3.1.2 State Vector Transfers from PGNCs

There were four state vector transfers in the Apollo 15 mission. Three of them were prior to PDI and one just before lunar surface liftoff. During the mission, the ground data processor indicated the first two pre-PDI state transfers were significantly in error. Specifically, the second state vector transfer (103:12:32.02 GET) CSM position and velocity errors displayed on the flight controllers console were 1071.84, 13,067.87, 318.15 feet; -11.62, -0.48, and -0.29 feet/second radial, downrange and crossrange respectively.

All four of the state vector transfers were analyzed by comparing the AGS and PGNCs state vectors which were obtained from telemetry data. The method used in this analysis was to propagate the PGNCs using a best estimate gravity model to the AGS epoch. The results were then compared with the AGS state vectors.

The results presented in Table 3.1 indicate that all four state vector transfers were properly executed and all errors were within the expected value of 750 feet for position components and 0.75 feet/second for velocity components.

The ground computed errors in the first two pre-PDI state vector transfers were evidently caused by the ground operations and not by the AGS or PGNCS.

3.2 Sensor Performance

3.2.1 Gyro and Accelerometer Free-flight Performance

Inflight gyro fixed drift is based on free-flight AGS attitude comparisons with PGNCS attitude and the AGS inflight and lunar surface calibrations. A history of gyro fixed drift for ASA 017 is presented in Table 3.2.

AGS accelerometer biases determined from calibrations and free-flight velocity accumulations are shown in Table 3.3. The histories show good long and short term stability.

3.2.2 AGS-PGNCS Attitude Difference During Powered Flight

In order to obtain estimates of gyro errors, two types of attitude differences are examined.

- 1) Body angle difference, $\underline{\theta}$. This parameter is the small angle difference between the AGS direction cosine (DC), matrix A, and the PGNCS gimbal angle matrix, G. It is computed from

$$I + \begin{bmatrix} 0 & \theta_Z & -\theta_Y \\ -\theta_Z & 0 & \theta_X \\ \theta_Y & -\theta_X & 0 \end{bmatrix} = AG^T$$

- 2) Integrated body rate difference, $\Delta\Omega$. This parameter is computed from:

$$\Delta\Omega = \int (\omega_{\text{AGS}} - \omega_{\text{PGNCS}}) dt$$

where the indicated rates are obtained from

$$I + [\omega_{\text{AGS}}] = \dot{A} A^T, I + [\omega_{\text{PGNCS}}] = \dot{G} G^T$$

In theory, this should be the more useful parameter since error propagation modes are simpler and initial matrix misalignments do not propagate at all. In practice, it has been found that integration of the 1 second data often yields misleading results, and $\Delta\Omega$ is used only to corroborate the patterns in the θ residual curves.

To simplify the error analysis, error equations were written for single axis rotations which occurred during the powered flight phases. The error model for each discrete maneuver analyzed will be given in the text. The error terms used are defined as follows:

ΔT = Timing error

θ_0 = Initial body angle difference (at the start of a given maneuver)

ψ = AGS gyro input axis misalignment w.r.t. NAV BASE

\underline{B} = $b_S + b_D$ = constant gyro rate difference (static + dynamic)

\underline{K} = Gyro scale factor error

3.2.2.1 Descent Attitude Differences

Three sets of data plots are provided to support the descent analysis.

- 1) Ω : Integrated body rate (Figures 3-3 through 3-5). These parameters do not generally represent physical angles, but do appear as driving functions on the error models.

- 2) θ : AGS-PGNCS body angle differences (Figure 3-6 through 3-8)
- 3) $\Delta\Omega$: AGS-PGNCS integrated body rate differences (Figure 3-9 through 3-11).

The reference time for each of these descent plots is 104:29:00.1 (LGC clock Time) which is approximately 70 seconds before descent engine ignition. For the minus 48 degree roll maneuver at $t = 250-266$ seconds on Figure 3-3, the error model for Y and Z attitude error and integrated body rate differences are:

$$\begin{aligned}\Delta\theta_Y &= -(\psi_Z - \theta_{0Z}) \sin \Omega_X + (\psi_Y - \theta_{0Y}) (1 - \cos \Omega_X) \\ \Delta\theta_Z &= (\psi_Z - \theta_{0Z}) (1 - \cos \Omega_X) + (\psi_Y - \theta_{0Y}) \sin \Omega_X \\ \Delta\Omega_Z &= -\psi_Z \Omega_X \\ \Delta\Omega_Y &= \psi_Y \Omega_X\end{aligned}$$

Using the values of $\Delta\theta$, θ_0 , and $\Delta\Omega$ taken from the appropriate plots, the "least squares" solution for the gyro misalignments is found to be:

$$\psi_Z = 44 \widehat{\text{sec}}, \psi_Y = 33 \widehat{\text{sec}}$$

For the minus 55 degree pitch maneuver at $t = 630-760$ seconds on Figure 3-4, the error equations for X and Z attitude error are:

$$\begin{aligned}\Delta\theta_X &= (\psi_Z - \theta_{0Z}) \sin \Omega_Y + (\psi_X - \theta_{0X}) (1 - \cos \Omega_Y) \\ \Delta\theta_Z &= (\psi_Z - \theta_{0Z}) (1 - \cos \Omega_Y) - (\psi_X - \theta_{0X}) \sin \Omega_Y\end{aligned}$$

Using the values of $\Delta\theta$ and θ_0 from the plots, the gyro misalignments are found to be:

$$\psi_Z = 36 \widehat{\text{sec}}, \psi_X = -35 \widehat{\text{sec}}$$

It should be clarified at this time, that true gyro input axis misalignment from the ASA cannot be separated from ASA misalignment to the navigation base. Therefore, in the subsequent discussions, when gyro input axis misalignment is referred to, the value quoted includes both error sources.

The constant pitch rate maneuver during the descent between 80 seconds and 500 seconds in Figure 3-4 provides a suitable segment of time for observing the input axes misalignments effects and at the same time to isolate the gyro drift effects. The $\Delta\Omega_X$ and $\Delta\Omega_Z$ curves are suitable for analysis and error models for the period in question are:

$$\Delta\Omega_X = \psi_Z \Omega_Y + \Delta T B_X$$

$$\Delta\Omega_Z = \psi_X \Omega_Y + \Delta T B_Z$$

Using the a priori ψ_Z and ψ_X values and the following observed changes:

$$\Delta\Omega_X = 20 \widehat{\text{sec}}$$

$$\Delta\Omega_Z = -35 \widehat{\text{sec}}$$

$$\Omega_Y = -35 \text{ degrees ;}$$

the two equations yield values of $B_X = +0.10$ degree/hr and $B_Z = -0.03$ degree/hr. Measured residual fixed drift for the X gyro pre-PDI was 0.10 degree/hr. The dynamic error for the X gyro is therefore approximately zero and the dynamic error for the Z gyro is -0.03 degree/hr. The Y data appears to be too noisy to interpret a drift value.

3.2.2.2 Ascent Attitude Differences

The ascent attitude comparisons consist of the same parameters used in the descent phase.

$\Omega_X, \Omega_Y, \Omega_Z$ shown in Figures 3-12, 3-13, 3-14

$\theta_X, \theta_Y, \theta_Z$ shown in Figures 3-15, 3-16, 3-17

$\Delta\Omega_X, \Delta\Omega_Y, \Delta\Omega_Z$ shown in Figures 3-18, 3-19, 3-20

The zero reference time on each of these plots is 171:37:00.35 (LGC clock time) which is approximately 22 seconds before liftoff.

As expected, the Y and Z channel data are quite noisy and generally unsuitable for any detailed error analyses. It is interesting to note that the noise level suddenly decreases after T = 300 seconds (particularly in Y), because the body rate limit cycle begins to subside.

The maneuver chosen for analyzing the gyro misalignments was a large pitch change at T = 578-630 seconds. Since the +100 degree pitch (Y) maneuver occurred after engine cutoff, the attitude comparisons are relatively noise free. The error model for the integrated body rate difference, $\Delta\Omega$ is:

$$\begin{aligned}\Delta\Omega_X &= \psi_Z \Omega_Y \\ \Delta\Omega_Y &= K_Y \Omega_Y + \Delta t \omega_Y \\ \Delta\Omega_Z &= \psi_X \Omega_Y\end{aligned}$$

The error model for the matrix misalignment, θ , is

$$\begin{aligned}\Delta\theta_X &= (\psi_Z - \theta_{OZ}) \sin \Omega_Y + (\psi_X - \theta_{OX}) (1 - \cos \Omega_Y) \\ \Delta\theta_Y &= K_Y \Omega_Y + \Delta t \omega_Y \\ \Delta\theta_Z &= -(\psi_X - \theta_{OX}) \sin \Omega_Y + (\psi_Z - \theta_{OZ}) (1 - \cos \Omega_Y)\end{aligned}$$

In terms of total changes across the maneuver, the error equations become:

$$\begin{aligned}\Delta\Omega_X &= 240 \widehat{\text{sec}} = 1.745 \psi_Z \\ \Delta\theta_X &= 160 \widehat{\text{sec}} = (\psi_Z + 146) (.985) + (\psi_X - 70) (1.174) \\ \Delta\theta_Z &= 320 \widehat{\text{sec}} = (\psi_Z + 146) (1.174) - (\psi_X - 70) (.985)\end{aligned}$$

The "best" least squares solution for the gyro misalignments is

$$\psi_Z = 113 \widehat{\text{sec}}, \psi_X = 15 \widehat{\text{sec}}$$

Knowing the above error sources the effects of X and Z dynamic gyro drift can now be estimated during the ascent burn by analyzing the θ_X plots.

The error model for the period in question is:

$$\Delta\theta_X = (\psi_Z - \theta_{OZ}) \sin \Omega_Y + (\psi_X - \theta_{OX})(1 - \cos \Omega_Y) + \frac{B_X}{\omega_Y} \sin \Omega_Y - \frac{B_Z}{\omega_Y} (1 - \cos \Omega_Y)$$

Observed changes from available plots across the time period, T = 120-454 seconds, are:

$$\begin{aligned} \Delta\theta_X &= -60 \widehat{\text{sec}} \\ \Omega_Y &= -36 \text{ degrees} \\ \omega_Y &= -.098 \text{ degree/sec} = 350 \text{ degree/hr} \end{aligned}$$

Using the a priori estimates of gyro misalignments from above and static bias errors from Table 3.2, the error model reduces to:

$$-60 \widehat{\text{sec}} = (-96 -22 + 52) \widehat{\text{sec}} + b_{DX} (346 \frac{\widehat{\text{sec}}}{\circ/\text{hr}}) + b_{DZ} (112 \frac{\widehat{\text{sec}}}{\circ/\text{hr}})$$

Thus we see that the a priori errors adequately explain the θ_X residuals, and conclude that there is no significant X-gyro dynamic drift and (with less certainty) no significant Z-gyro dynamic drift.

3.2.3 Powered Descent Velocity Comparisons

Start of powered descent (PDI) was at 104:30:09 GET with lunar touch-down occurring at 104:42:30 GET. Total accumulated velocity during the descent phase was approximately 6829 feet/second. PGNCs sensed two second velocity data were corrected for PGNCs errors. (See Section 2), rotated into body axes using IMU gimbal angles and summed to form velocity histories in body space. Differencing these PGNCs body axes velocities from the AGS sensed velocities, derived by extracting gravity from the AGS velocity state vector and rotating the sensed ΔV using the DC matrix, yielded the curves shown in Figures 3-21 through 3-23. Since these differences are derived using gimbal angle data to rotate PGNCs V (gimbal angles provide

a true relationship between body and platform space) and using the CD matrix to rotate AGS ΔV (which is simply reversing the process the onboard computer performed), the error curves theoretically represent only accelerometer errors and timing errors. The step change in velocity error occurring at entrance to the approach phase (P64) in Figure 3-21 is also observable in Z channel (Figure 3-23). This is a data processing error resulting from the inability to properly handle high angular acceleration. At P64, the LM performs a pitch maneuver of approximately 40 degrees to allow the astronaut to view the landing site. The maneuver is performed at an angular rate high enough to produce sizable angular accelerations at the IMU and ASA due to the offset of the sensors from the LM center of gravity. Due to the low frequency data rate, perfect transformation of this angular acceleration from IMU to body axes is difficult and some processing error is unavoidable. The 0.8 feet/second step in velocity error results. This problem has been encountered on previous missions and is discussed in Reference 3.

Using a weighted least squares filter with the AGS accelerometer error model, a set of error coefficients was determined which fit the velocity difference curves. Modeled accelerometer errors are listed in Table 3.4. The fit was terminated at the P64 point so as not to corrupt the fit with the unmodeled step error. Results of the fit are listed below:

<u>Error Model Symbol</u>	<u>Description</u>	<u>Value</u>
XASF	X Accelerometer scale factor	12 ppm
YAMTX	Y Accelerometer misalignment toward X	-16 $\widehat{\text{sec}}$
ZAMTX	Z Accelerometer misalignment toward X	4 $\widehat{\text{sec}}$
XAB	X Accelerometer static bias	-33 ug
YAB	Y Accelerometer static bias	-21 ug
ZAB	Z Accelerometer static bias	-38 ug

The accelerometer bias errors were constrained in the fit to agree with the static bias values determined before PDI ignition. All of the remaining errors in the X channel have been solved for in terms of scale factor error (XASF) because the only other sensitive error in the X channel, dynamic accelerometer bias, is highly correlated with XASF and inseparable. For the Y channel, all of the dynamic error has been solved for in terms of Y accelerometer misalignment toward X (YAMTX) because the only other significant error, dynamic accelerometer bias, is highly correlated and inseparable. For the Z channel, misalignment and dynamic bias are similarly inseparable.

3.2.4 Ascent Velocity Comparisons

Start of ascent was at 171:37:22 GET with insertion occurring at 171:44:30 GET. Total accumulated velocity during the ascent phase was approximately 5970 feet/second. Ascent velocity differences were developed in the same manner described in descent Section 3.2.3, and are presented in Figures 3-24 through 3-26. PGNC errors (see Section 2) have been eliminated from these differences. The weighted least squares filter was used to fit a set of AGS accelerometer errors to the velocity differences. Results of the fit were as follows:

<u>Error Model Symbol</u>	<u>Description</u>	<u>Value</u>
XASF	X Accelerometer scale factor	-142 ppm
YAMTX	Y Accelerometer misalignment toward X	-25 $\widehat{\text{sec}}$
ZAMTX	Z Accelerometer misalignment toward X	-32 $\widehat{\text{sec}}$
XAB	X Accelerometer static bias	- 30 ug
YAB	Y Accelerometer static bias	- 53 ug
ZAB	Z Accelerometer static bias	- 46 ug

The accelerometer static biases in the fit were based on a segment of free fall data after completion of orbit insertion. For the same reasons indicated in the descent discussion, all the remaining X axis velocity error was solved for in terms of scale factor error and all remaining Y and Z velocity error has been solved for in terms of instrument misalignments toward the spacecraft X axis.

3.2.5 Comparisons of ASA Inflight Errors to Preflight Performance Estimates

3.2.5.1 Accelerometer Error Summary

Based on the AGS capability estimate, the accelerometer errors agree favorably with the preflight performance estimates derived for the particular instruments flown on Apollo 15.

For powered flight, accelerometer errors are summarized in Table 3-5. As noted in Section 3.2.3, individual accelerometer dynamic error terms are not fully separable and as a result were arbitrarily grouped into one error source for each axis. For comparison with the preflight estimates, again it was necessary to define a single performance index which could represent the premission performance estimates and the inflight estimate. A performance index was derived by converting all the non-bias errors such as sensing axis misalignment and scale factor error into equivalent acceleration errors. This is possible only because the ratios of the partials for the errors mentioned above are fairly constant through the descent and ascent trajectories, thus explaining the high correlation between these errors.

The table shows reasonable corroboration of errors with the preflight system modeling for ASA 017 and good correlation between the two phases of flight.

3.2.5.2 Gyro Error Summary

Gyro information retrieved from the attitude comparisons during ascent and descent indicate excellent agreement with ASA 017 Preflight Performance Estimates. Dynamic bias information was obtained on the X and Z instruments, however noisy data precluded separation of any meaningful information about the Y gyro. Free-flight stability was excellent for all instruments. Gyro drift information for descent and ascent are compared with the preflight estimates in Table 3-6. Gyro misalignment information retrieved from the analysis is presented in Table 3.7 and indicates good agreement with the preflight error model.

TIME GET hr:min:sec	ΔX ft	ΔY ft	ΔZ ft	ΔV_X ft/sec	ΔV_Y ft/sec	ΔV_Z ft/sec
101:23:17.216	113.	-86.	9.	.202	.126	-.253
103:12:13.216	-50.	-250.	-158.	-.227	.125	-.096
104:12:49.206	558.	-109.	138.	-.195	.113	.608
171:21:15.96	-138.	-12.	160.	.031	.048	.236
LM STATE VECTOR ERRORS IN AGS COORDINATES						

TIME GET hr:min:sec	ΔX ft	ΔY ft	ΔZ ft	ΔV_X ft/sec	ΔV_Y ft/sec	ΔV_Z ft/sec
101:23:17.216	-66.	173.	33.	-.148	.035	.082
103:12:13.216	317.	-71.	-22.	-.251	.218	-.178
104:12:49:204	-62.	-146.	-65.	.435	.079	.215
171:21:15.96	-292.	275.	-321.	.216	-.05	-.001
CSM STATE VECTOR ERRORS IN AGS COORDINATES						

Table 3-1. State Vector Transfer Errors

Table 3.2. ASA 017 Gyro Static Bias Drift History (Deg/Hr)

Gyro	(1)	(2)	(3)	(4)	(5)	(6)
	Preflight Mean	Inflight Calibration 101:40	Rev 13 104:10 - 104:20	Lunar Surface Calibration #1 105:00	Lunar Surface Calibration #2 170:36	Post Ascent 171:58
X	-0.12	-0.21	-0.11	-0.14	-0.12	0.03
Y	-0.93	-0.81	-0.76	-0.81	-0.78	-0.75
Z	0.06	0.15	0.15	0.06	0.02	-0.02

Table 3.3. ASA 017 Accelerometer Static Bias History (ug)

Accelerometer	Preflight Calibration		Inflight Calibration		Pre-Descent		Post-Ascent	
	Mean							
X	-67		-62		-95		-92	
Y	93		124		103		71	
Z	-89		-62		-100		-108	

Table 3.4. LM AGS Error Model (Accelerometer)

Mnemonic	Description
XAB	X accelerometer bias
YAB	Y accelerometer bias
ZAB	Z accelerometer bias
XASF	X accelerometer scale factor
XAMTY	X accelerometer misalignment toward Y
XAMTZ	X accelerometer misalignment toward Z
YAMTX	Y accelerometer misalignment toward X
YASF	Y accelerometer scale factor
YAMTZ	Y accelerometer misalignment toward Z
ZAMTX	Z accelerometer misalignment toward X
ZAMTY	Z accelerometer misalignment toward Y
ZASF	Z accelerometer scale factor
TB	Accelerometer timing bias

Table 3.5. Accelerometer Error Summary

Descent Equivalent Accelerometer Bias Errors (ug)					
Axis	Error Source	Inflight Estimate	ASA 017 Preflight Estimate		
			Mean	3 σ	
X	Bias, nonlinearity and dynamic errors		-6	101	
	Scale factor		<u>16</u>	<u>74</u>	
	Total	-26	10	125	
Y	Bias, nonlinearity and dynamic errors		-4	88	
	Internal sensing axis alignment		-54	34	
	ASA alignment to navigation base		<u>0</u>	<u>195</u>	
	Total	-44	-58	217	
Z	Bias, nonlinearity and dynamic errors		-22	88	
	Internal sensing axis alignment		0	12	
	ASA alignment to navigation base		<u>0</u>	<u>195</u>	
	Total	-32	-22	214	
Ascent Equivalent Accelerometer Bias Errors (ug)					
Axis	Error Source	Inflight Estimate	ASA 017 Preflight Estimate		
			Mean	3 σ	
X	Bias, nonlinearity and dynamic errors		-6	107	
	Scale factor		<u>19</u>	<u>95</u>	
	Total	-91	13	143	
Y	Bias, nonlinearity and dynamic errors		-4	3	
	Internal sensing axis alignment		-72	46	
	ASA alignment to navigation base		<u>0</u>	<u>156</u>	
	Total	-105	-76	162	
Z	Bias, nonlinearity and dynamic errors		-22	2	
	Internal sensing axis alignment		0	16	
	ASA alignment to navigation base		<u>0</u>	<u>156</u>	
	Total	-113	-22	157	

Table 3.6. Gyro Bias Error Summary (Deg/Hr)

		Descent		
		ASA 017 Preflight Estimate		ASA 017 Inflight Estimate
		Mean	3σ	
X	Gyro fixed drift	0	0.45	0.10 (1)
Y		0	0.45	0.05 (1)
Z		0	0.46	0 (1)
X	Gyro spin axis mass unbalance	0	0.53	} (2) 0
X	Gyro dynamic drift	0.02	0.29	
Y		0.13	0.25	-
Z		<u>- 0.09</u>	<u>0.26</u>	<u>-0.03</u>
X	Total (deg/hr)	0.02	0.75	0.10
Y		0.13	0.51	-
Z		- 0.09	0.53	-0.03

		Ascent		
		ASA 017 Preflight Estimate		ASA 017 Inflight Estimate
		Mean	3σ	
X	Gyro fixed drift	0	0.42	0.15 (3)
Y		0	0.41	0.03 (3)
Z		0	0.41	-0.04 (3)
X	Gyro Spin axis mass unbalance	0	0.53	} (2) 0
X	Gyro dynamic drift	0.02	0.26	
Y		0.11	0.28	-
Z		<u>- 0.07</u>	<u>0.34</u>	<u>0</u>
X	Total drift (deg/hr)	0.02	0.72	0.15
Y		0.11	0.51	-
Z		- 0.07	0.53	-0.04

(1) Table 3.2 column 3 minus column 2

(2) Postflight data are not sufficient to separate x gyro spin axis unbalance and gyro dynamic drift

(3) Table 3.2 column 6 minus column 5

Table 3.7. Gyro Input Axis Misalignments

Gyro Input Axis Error Sources	ASA 017 Preflight Estimate ($\widehat{\text{sec}}$)		Inflight Value Descent ($\widehat{\text{sec}}$)	Inflight Value Ascent ($\widehat{\text{sec}}$)
	Mean	3σ		
Internal misalignment X toward Y	50	9		
ASA to nav. base mis- alignment	$\frac{0}{50}$	$\frac{120}{120}$	$\psi_Z = 44$	$\psi_Z = 113$
Internal misalignment Z toward X	33	19		
ASA to nav. base mis- alignment	$\frac{0}{33}$	$\frac{120}{121}$	$\psi_Y = 33$	Not attainable
Internal misalignment Z toward Y	-39*	15		
ASA to nav. base mis- alignment	$\frac{0}{-39}$	$\frac{120}{121}$	$\psi_X = -35$	$\psi_X = 15$

As shown in the table, inflight estimates cannot separate internal misalignments from ASA misalignments.

* Sign reversed to agree with inflight convention.

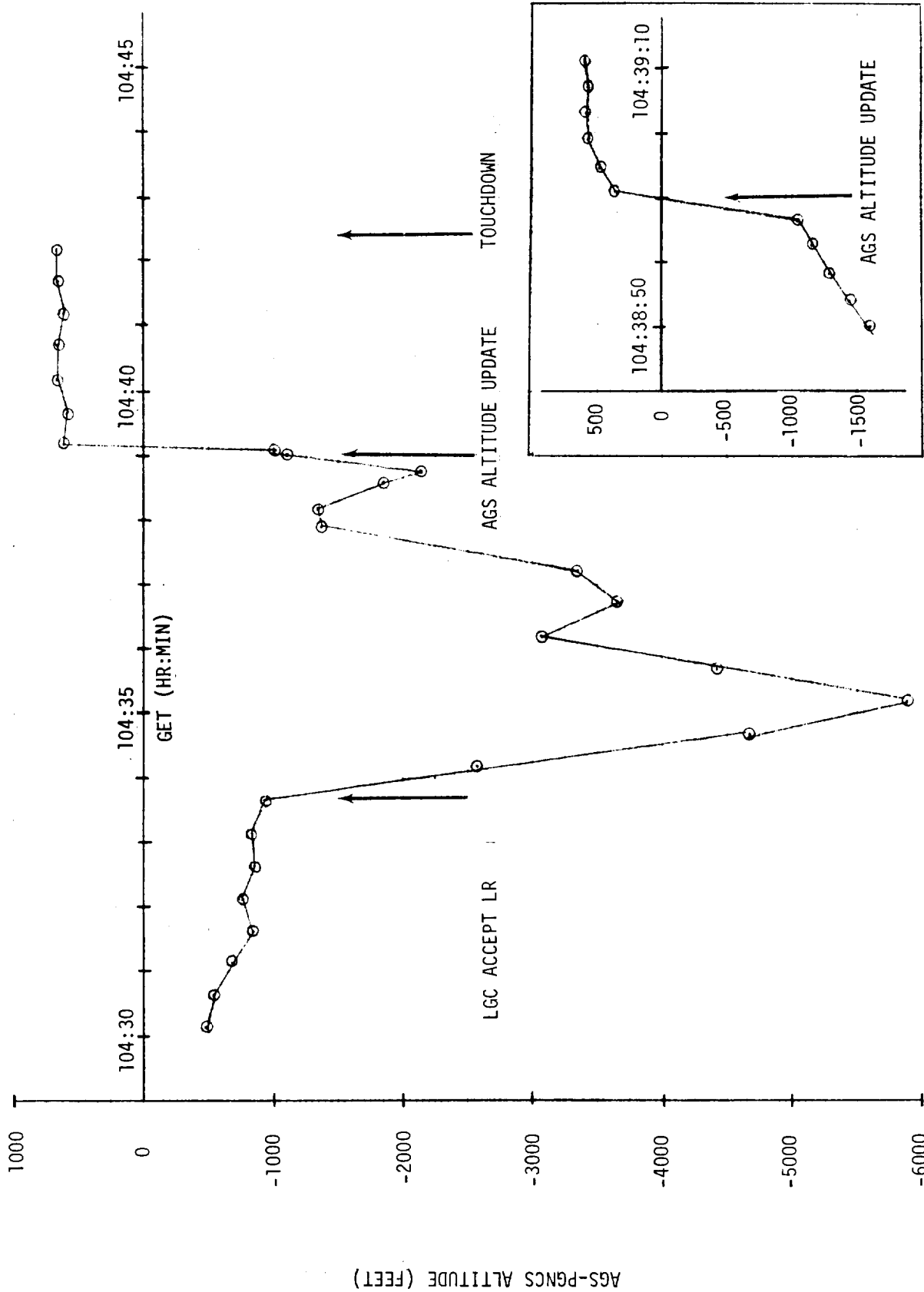


FIGURE 3-1 AGS-PGNCS ALTITUDE DIFFERENCE

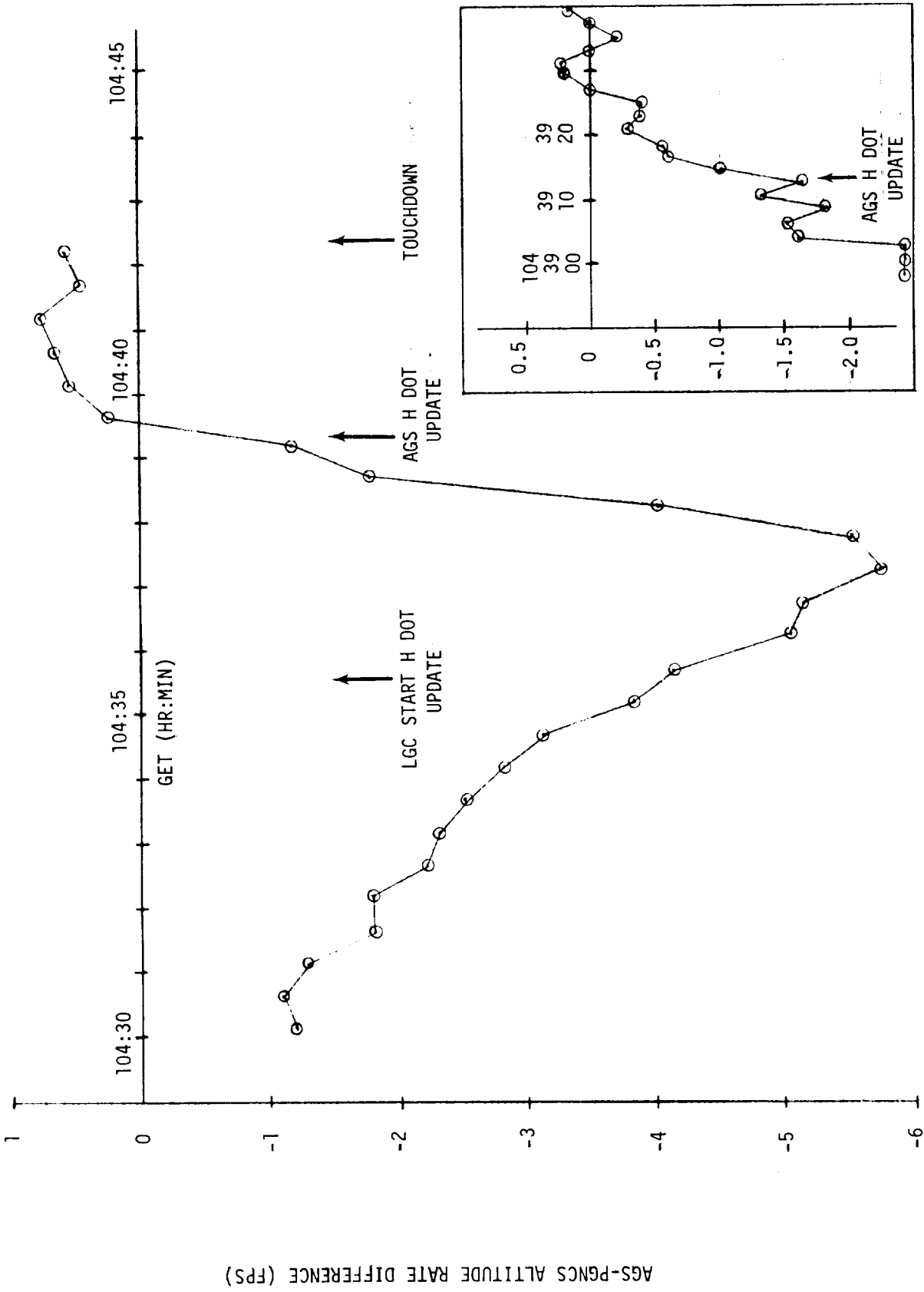


FIGURE 3-2 AGS-PGNCS ALTITUDE RATE DIFFERENCE

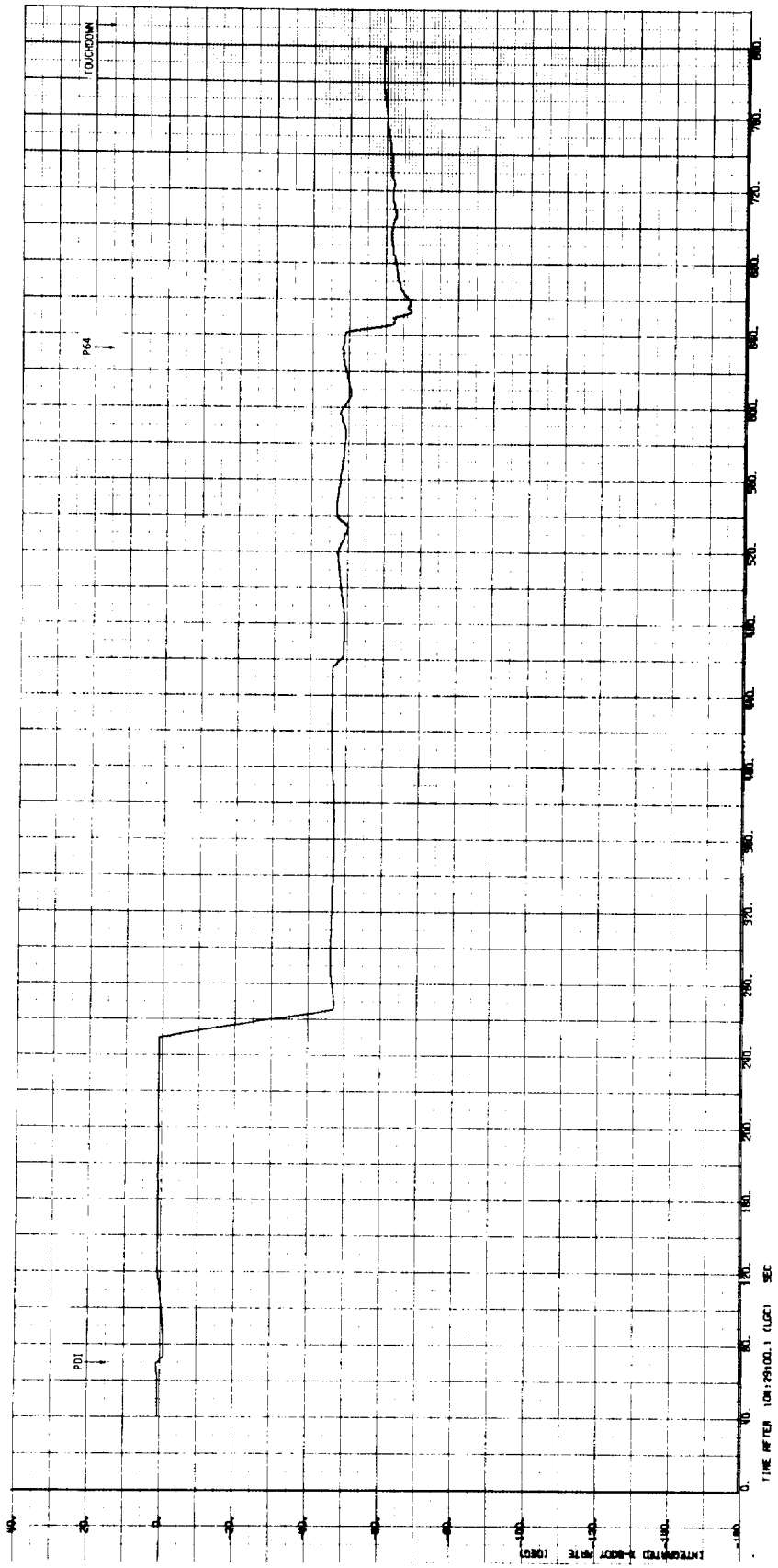


FIGURE 3-3. APOLLO 15 LM DESCENT INTEGRATED BODY RATE

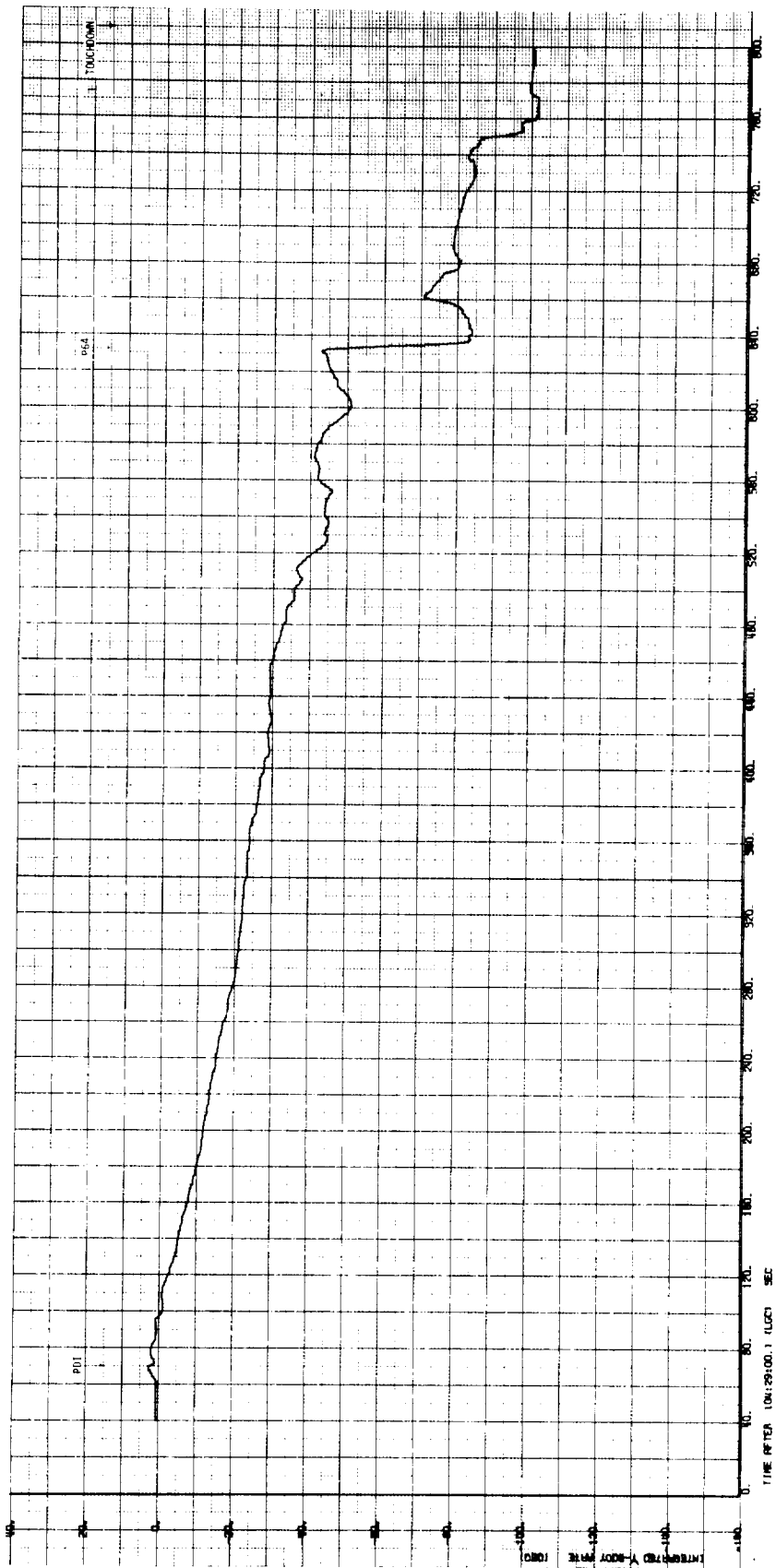


FIGURE 3-4. APOLLO 15 LM DESCENT INTEGRATED BODY RATE

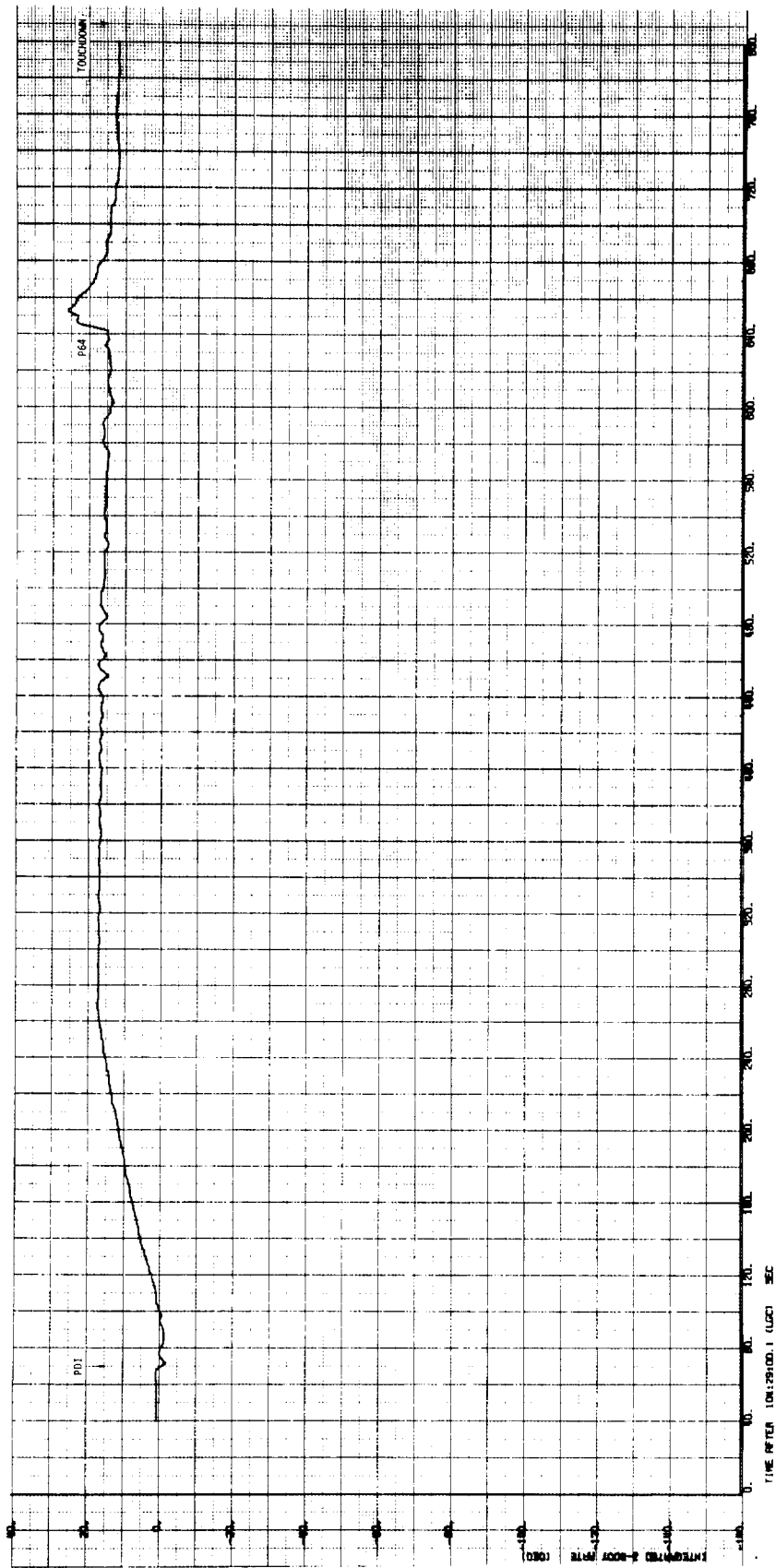


FIGURE 3-5. APOLLO 15 LM DESCENT
INTEGRATED BODY RATE

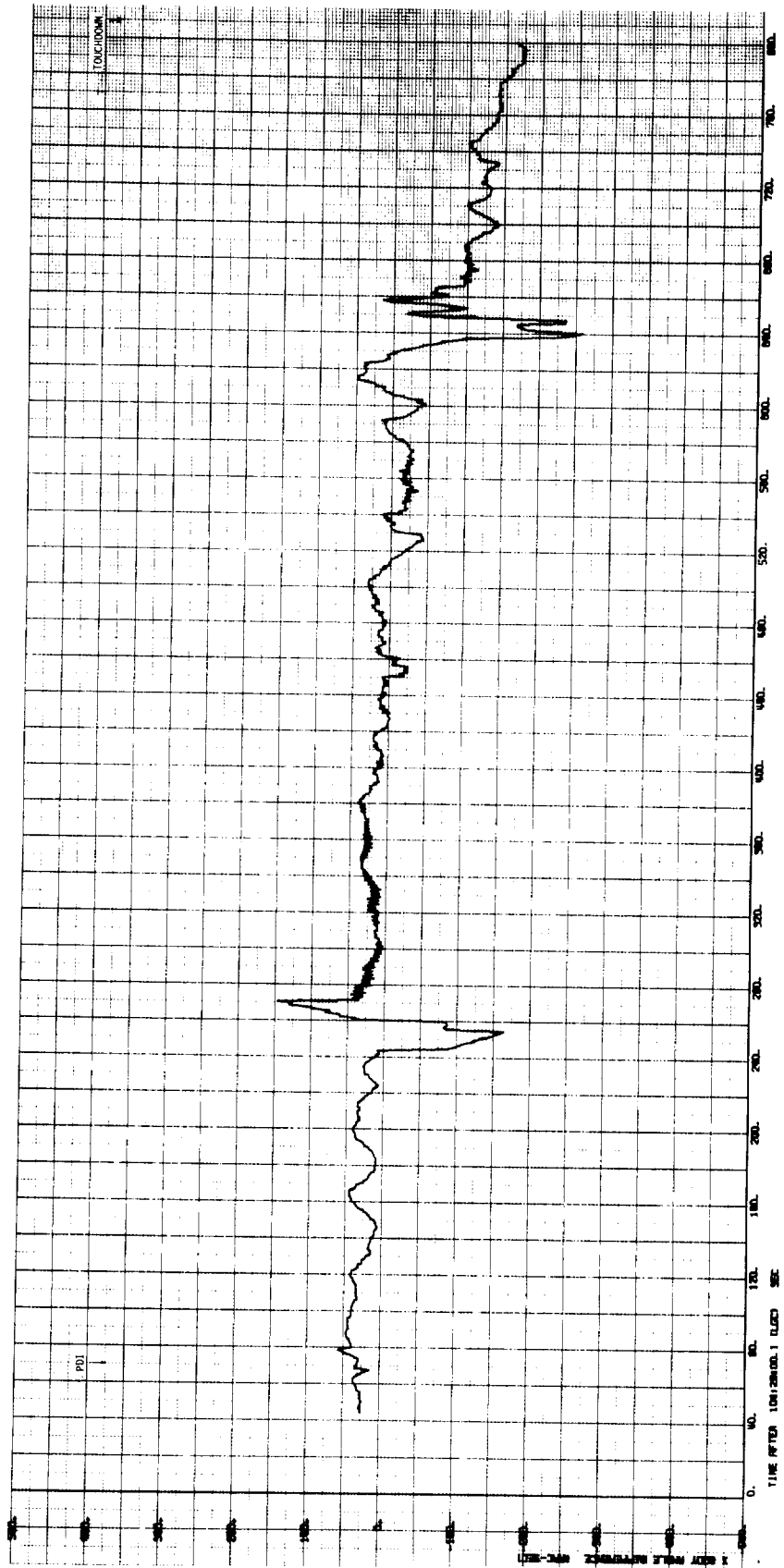


FIGURE 3-6. APOLLO 15 LM DESCENT AGS-PGS ATTITUDE DIFFERENCE

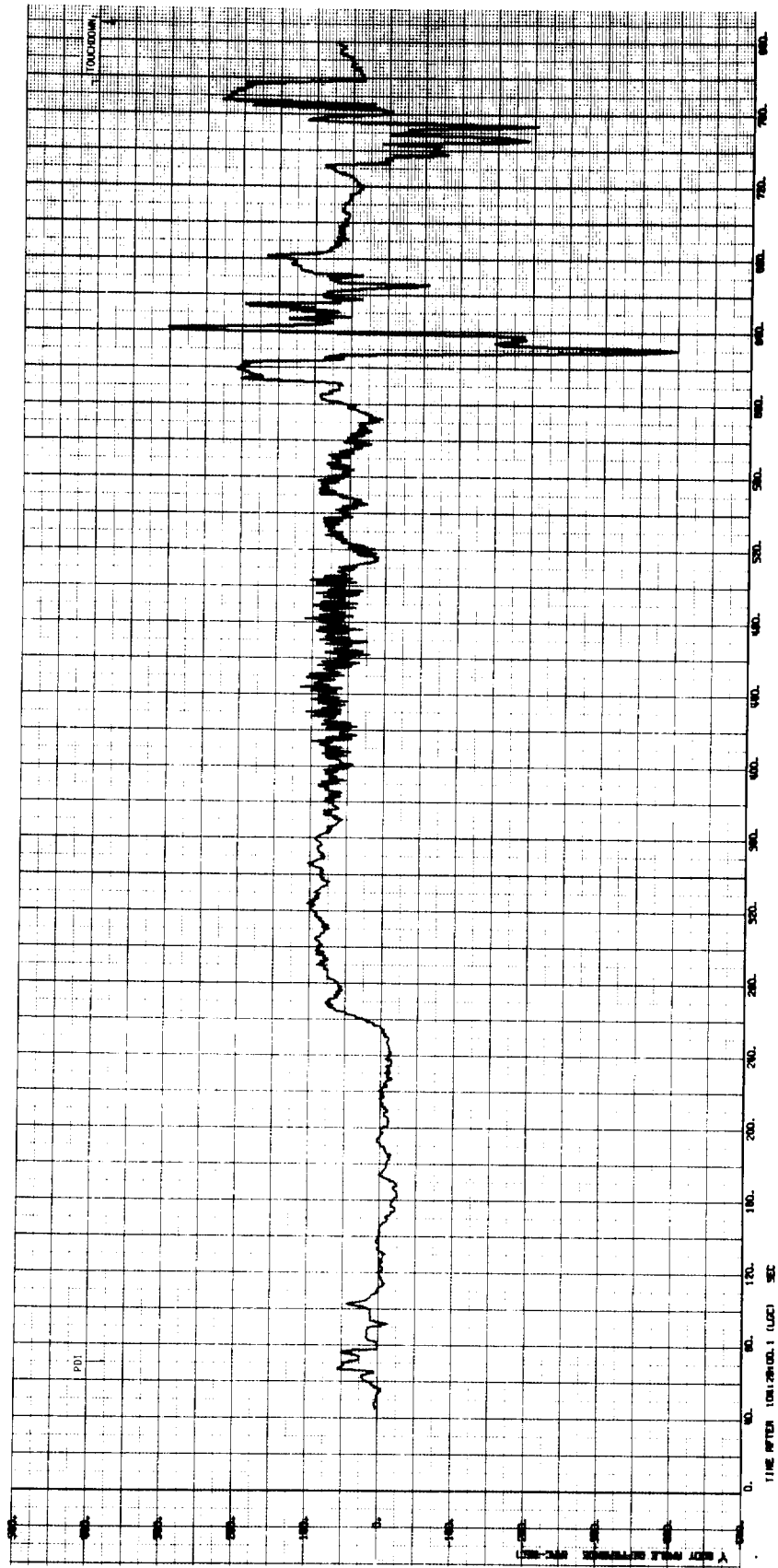


FIGURE 3-7. APOLLO 15 LM DESCENT AGS-PGS ATTITUDE DIFFERENCE

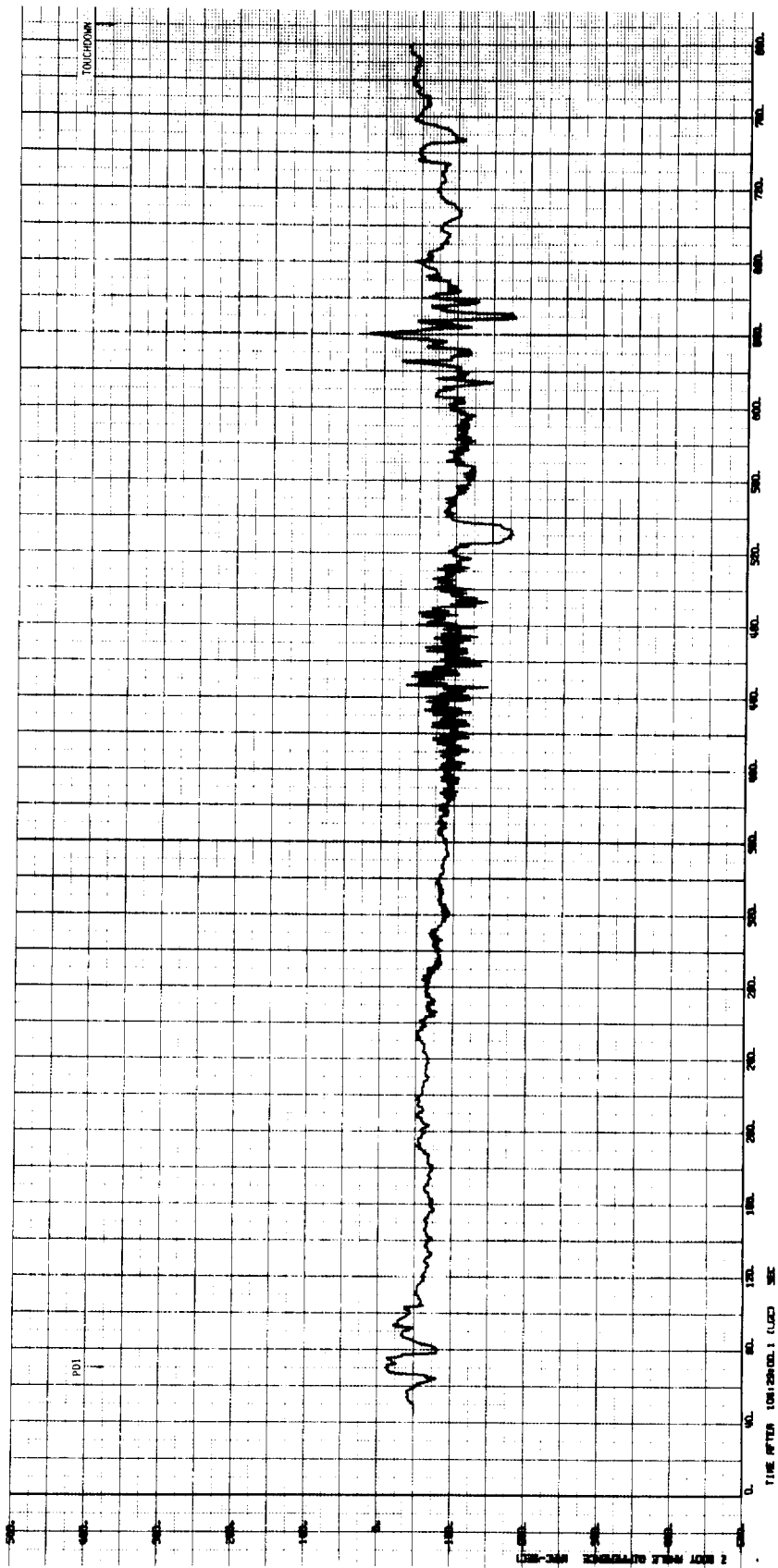


FIGURE 3-8. APOLLO 15 LM DESCENT AGS-PGS ATTITUDE DIFFERENCE

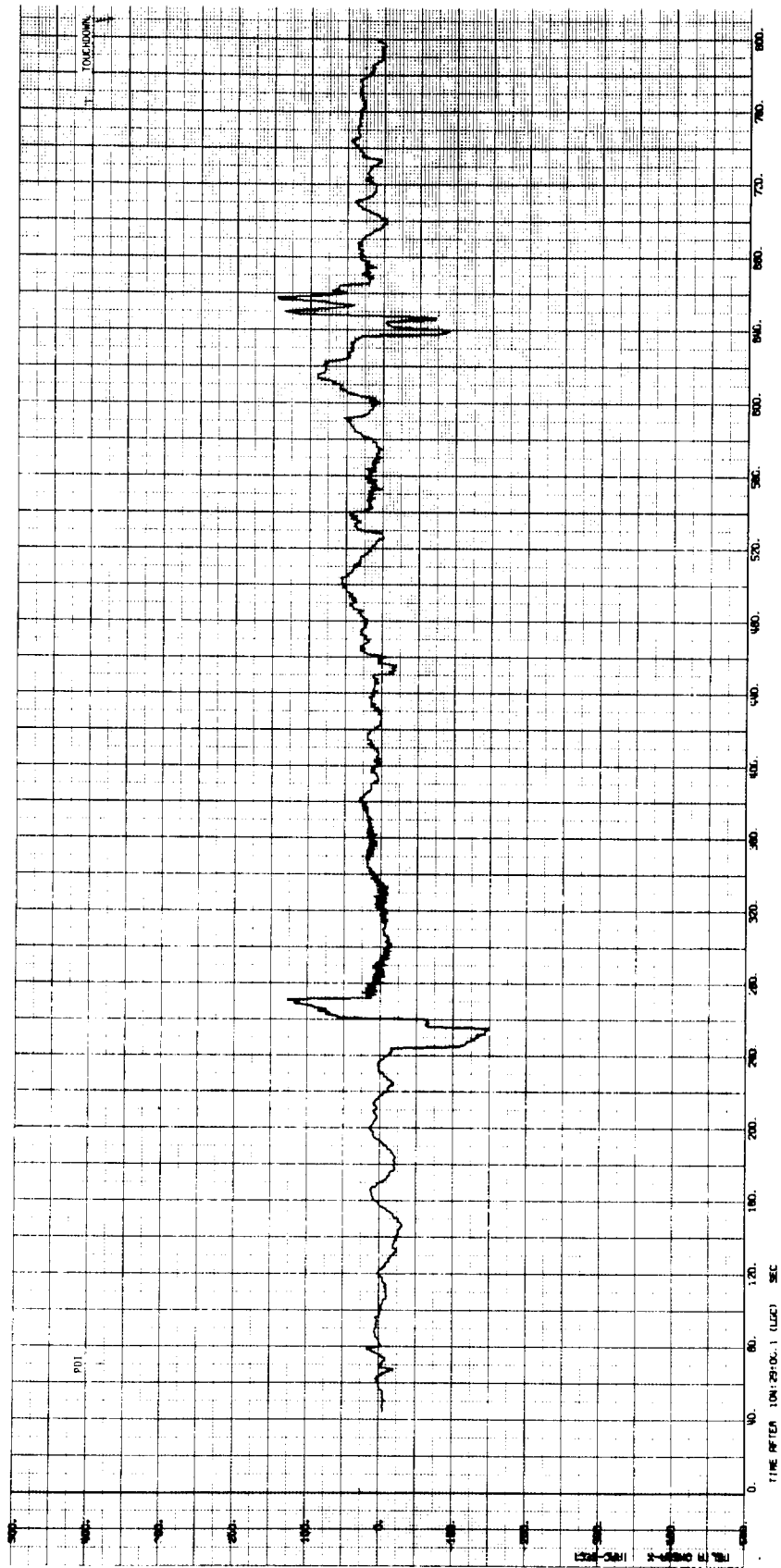


FIGURE 3-9. APOLLO 15 LM DESCENT AGS-PGS INT. BODY RATE DIFFERENCE

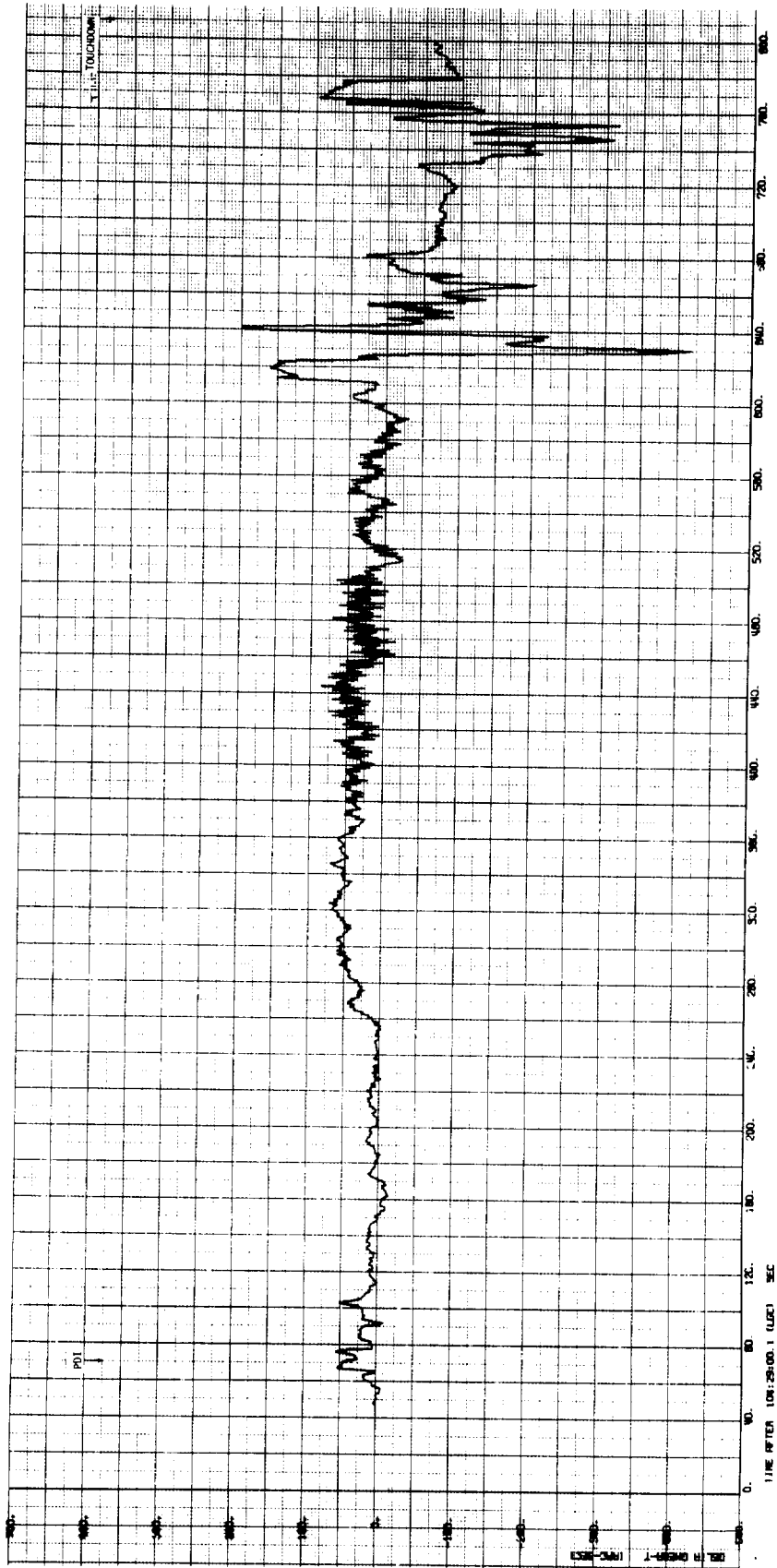


FIGURE 3-10. APOLLO 15 LM DESCENT AGS-PGS
INT. BODY RATE DIFFERENCE

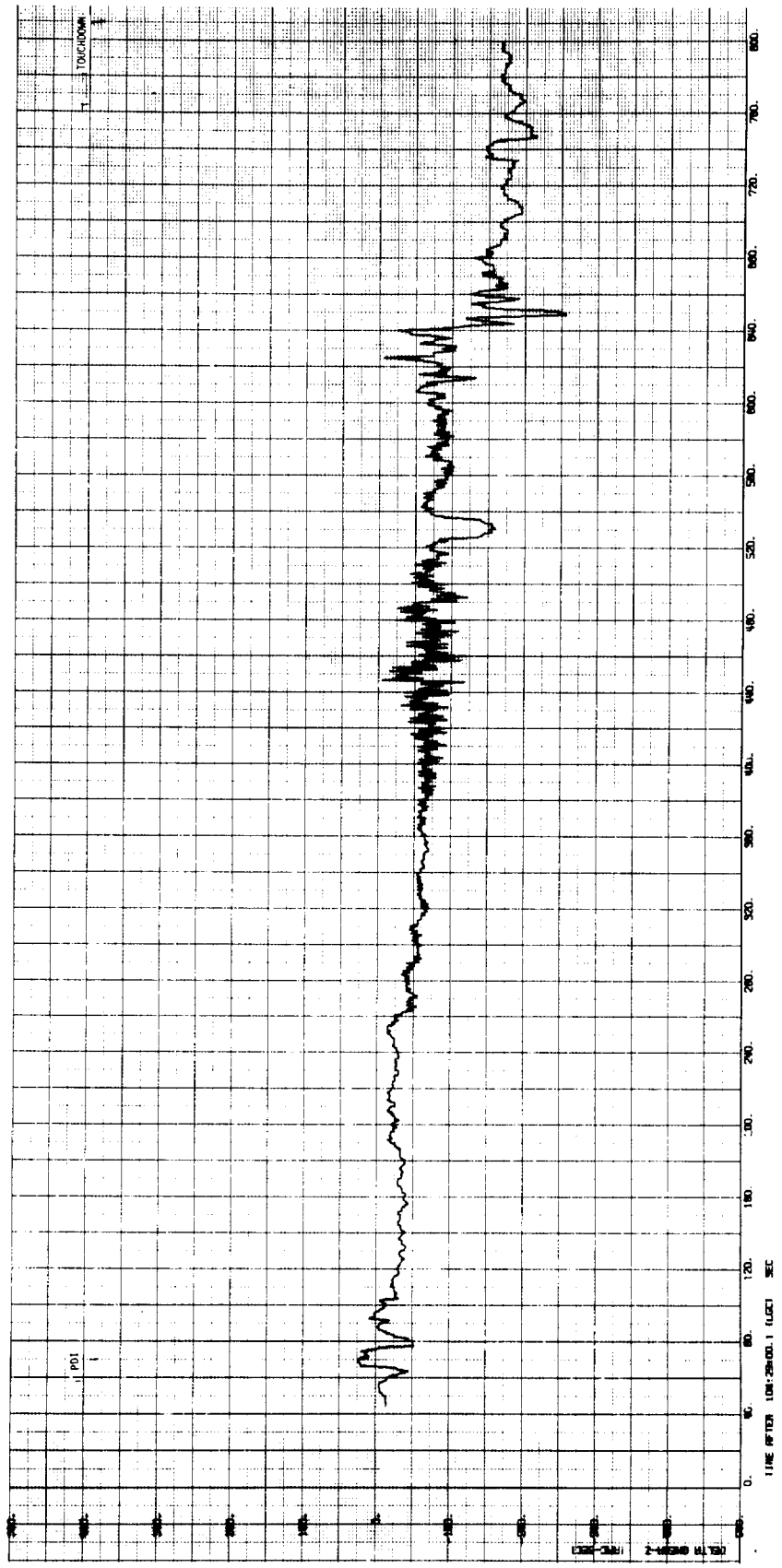


FIGURE 3-11. APOLLO 15 LM DESCENT AGS-PGS
INT. BODY RATE DIFFERENCE

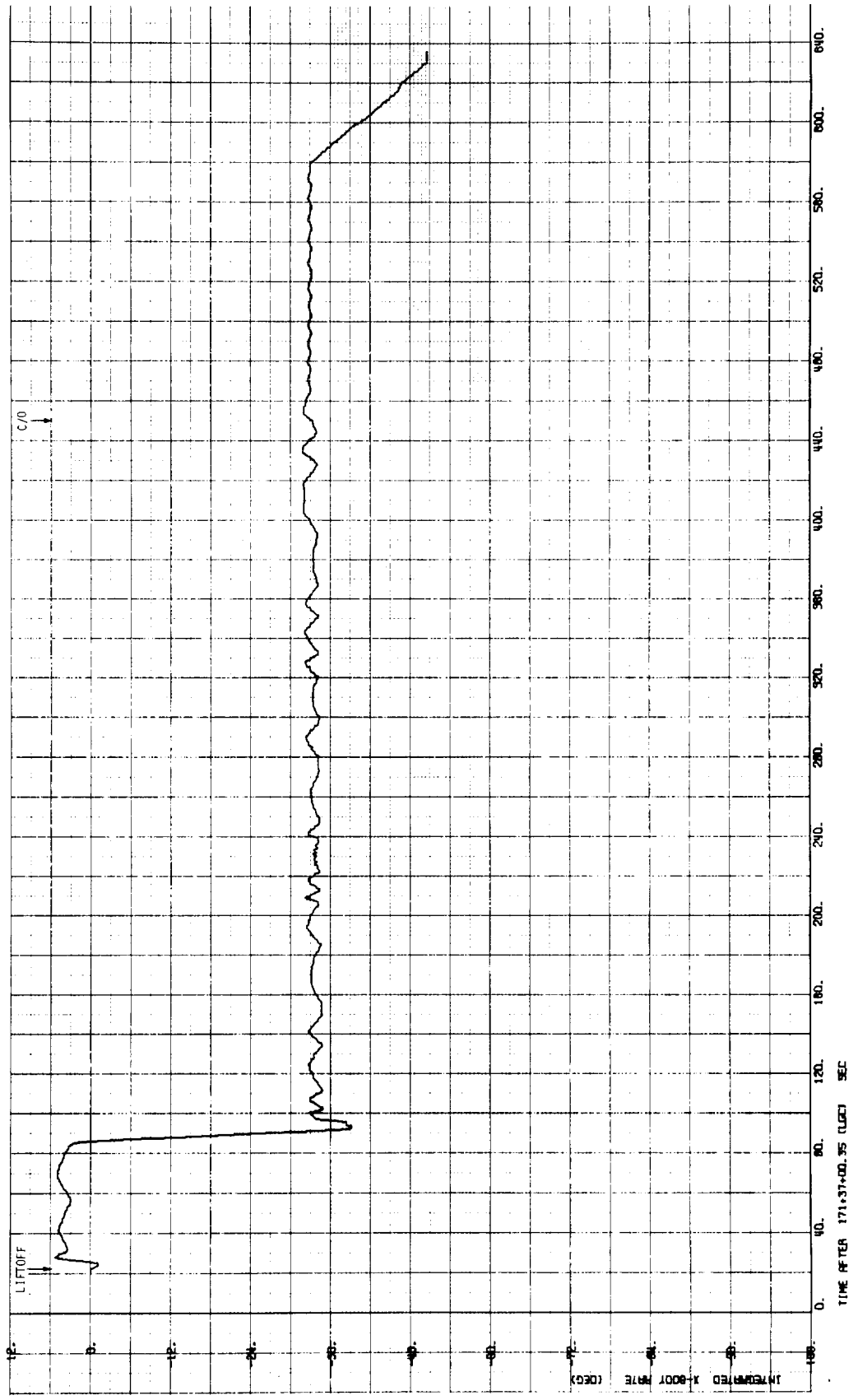


FIGURE 3-12. APOLLO 15 LM ASCENT INTEGRATED BODY RATE

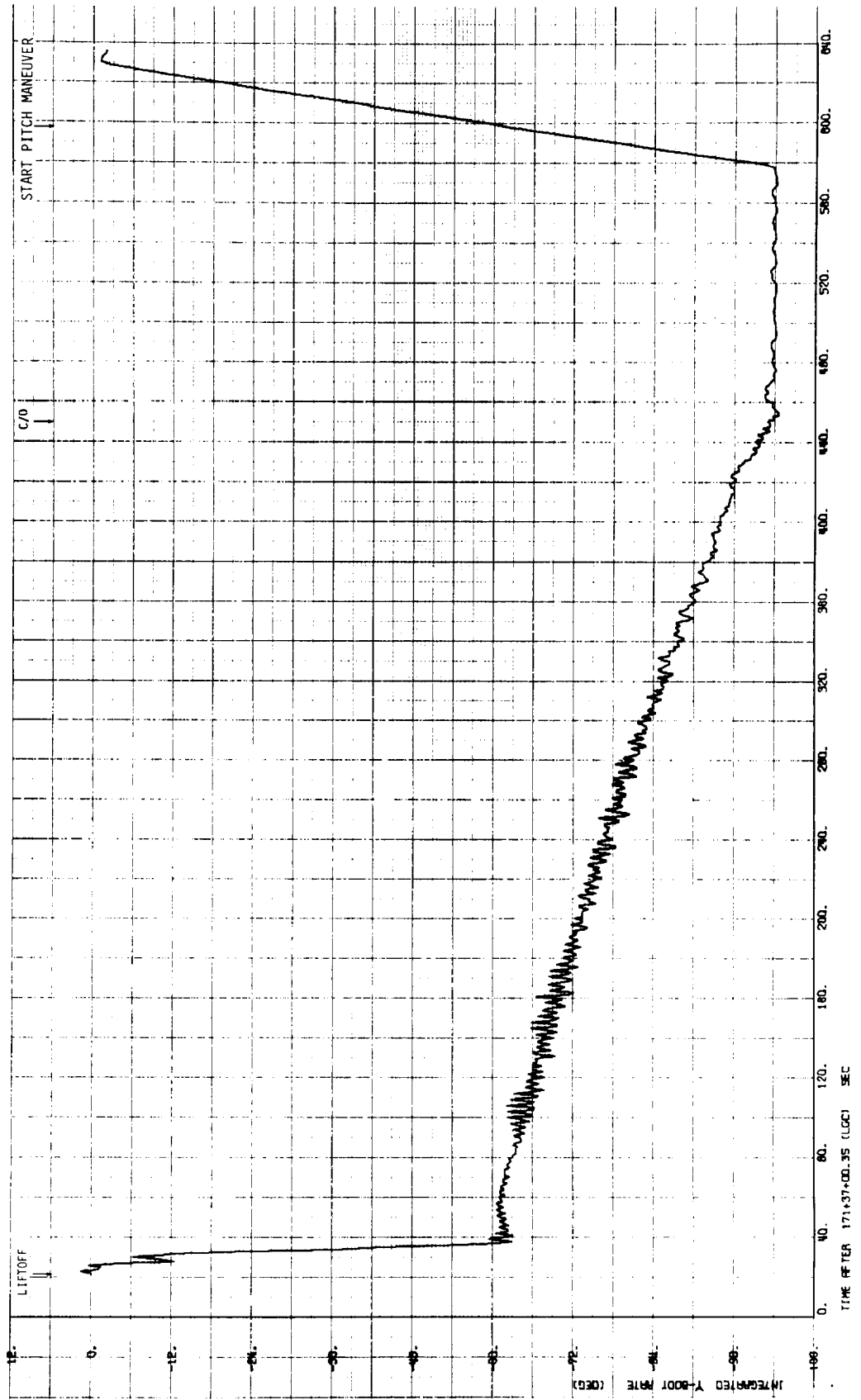


FIGURE 3-13. APOLLO 15 LM ASCENT INTEGRATED BODY RATE

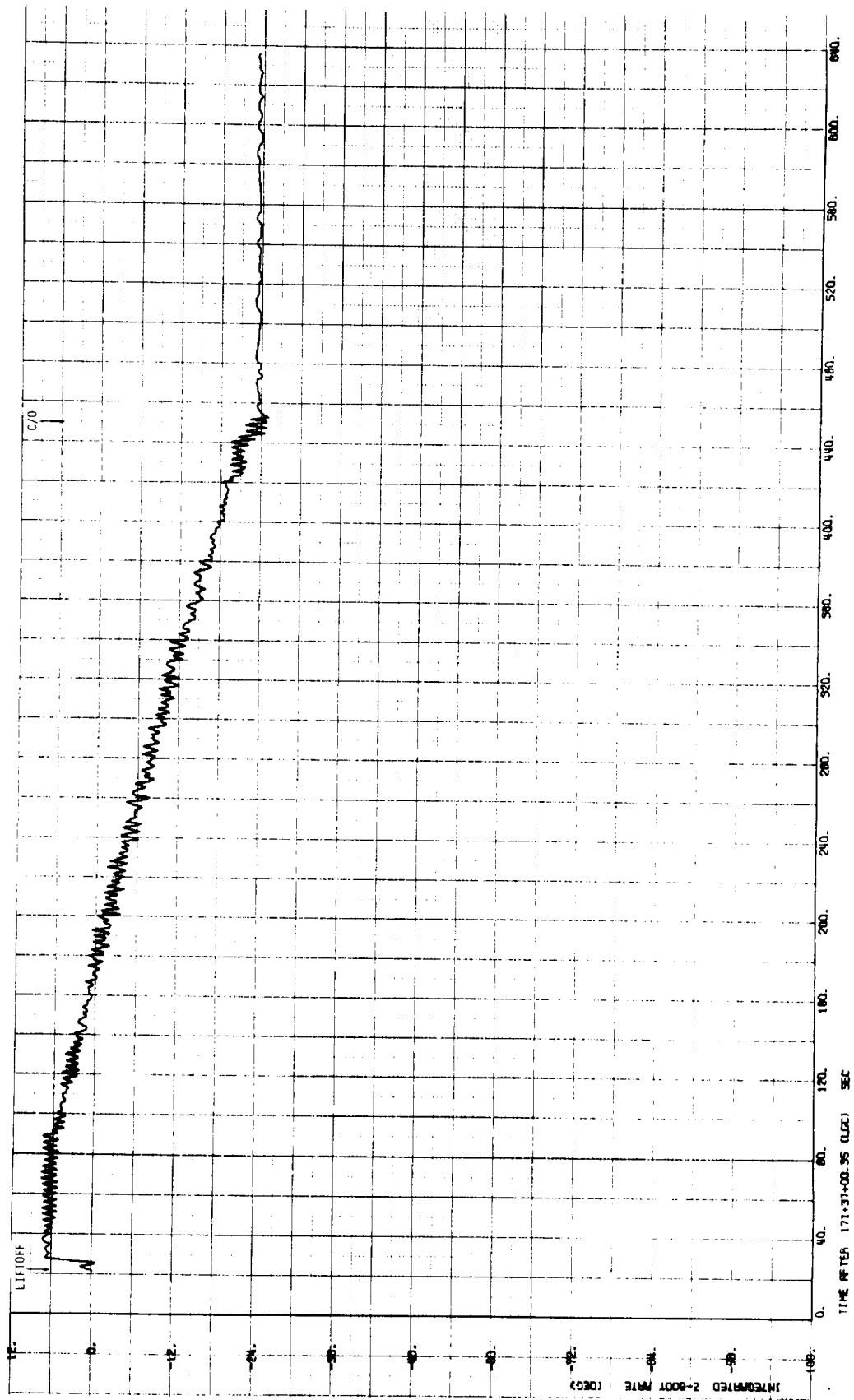


FIGURE 3-14. APOLLO 15 LM ASCENT
INTEGRATED BODY RATE

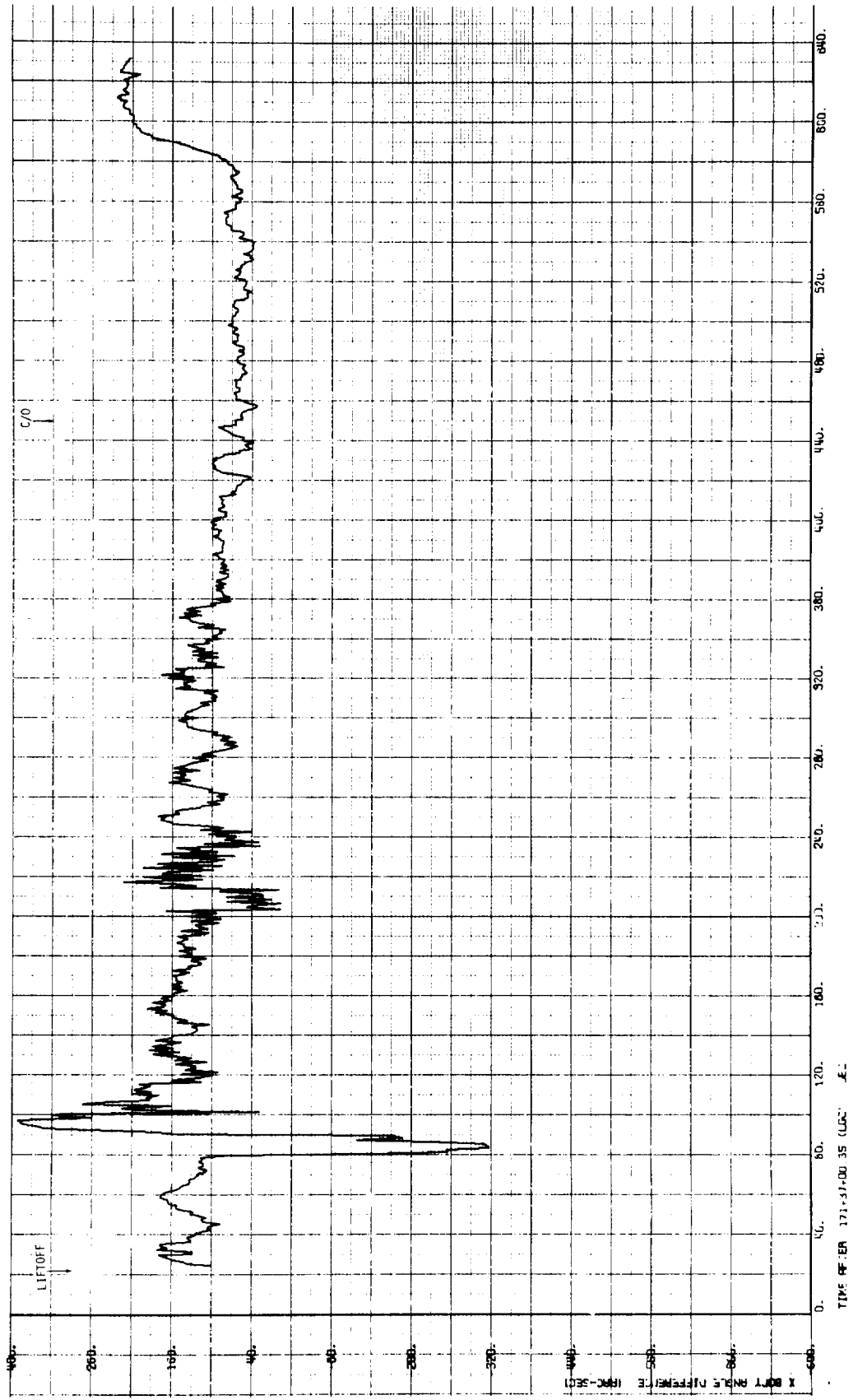


FIGURE 3-15. APOLLO 15 LM ASCENT AGS-PGS ATTITUDE DIFFERENCE

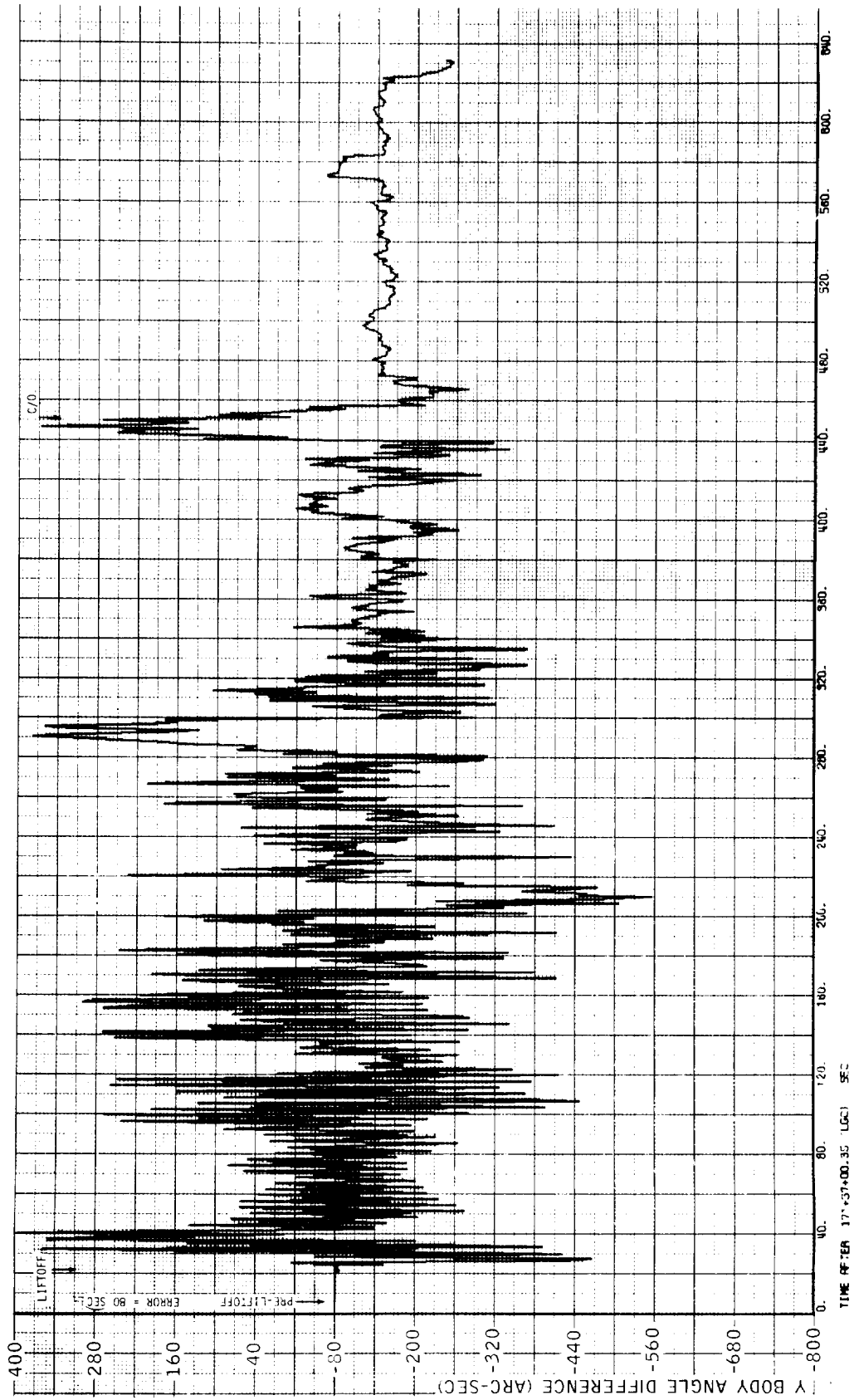


FIGURE 3-16. APOLLO 15 ASCENT AGS-PGCS ATTITUDE DIFFERENCE

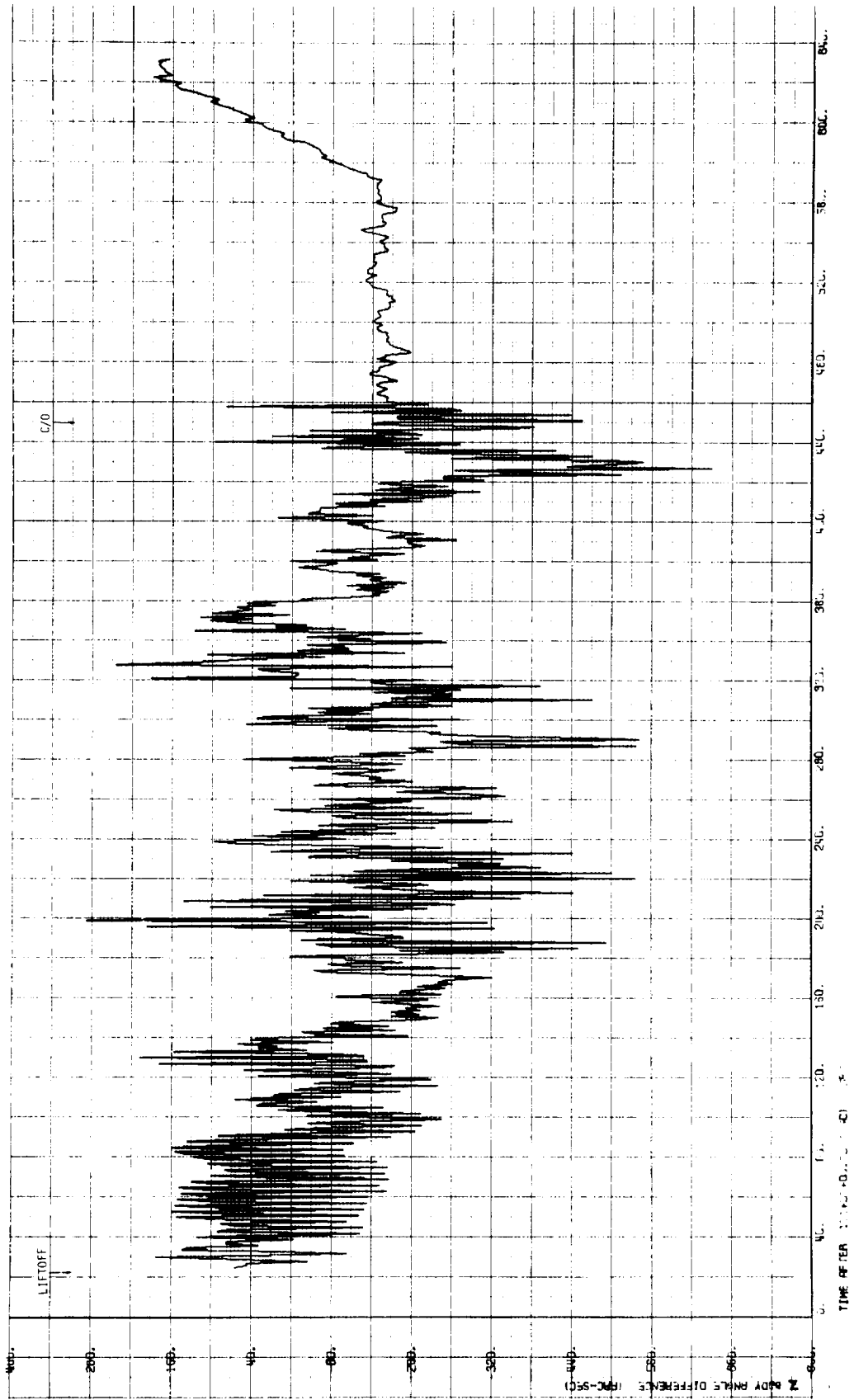


FIGURE 3-17. APOLLO 15 LM ASCENT AGS-PGS ATTITUDE DIFFERENCE

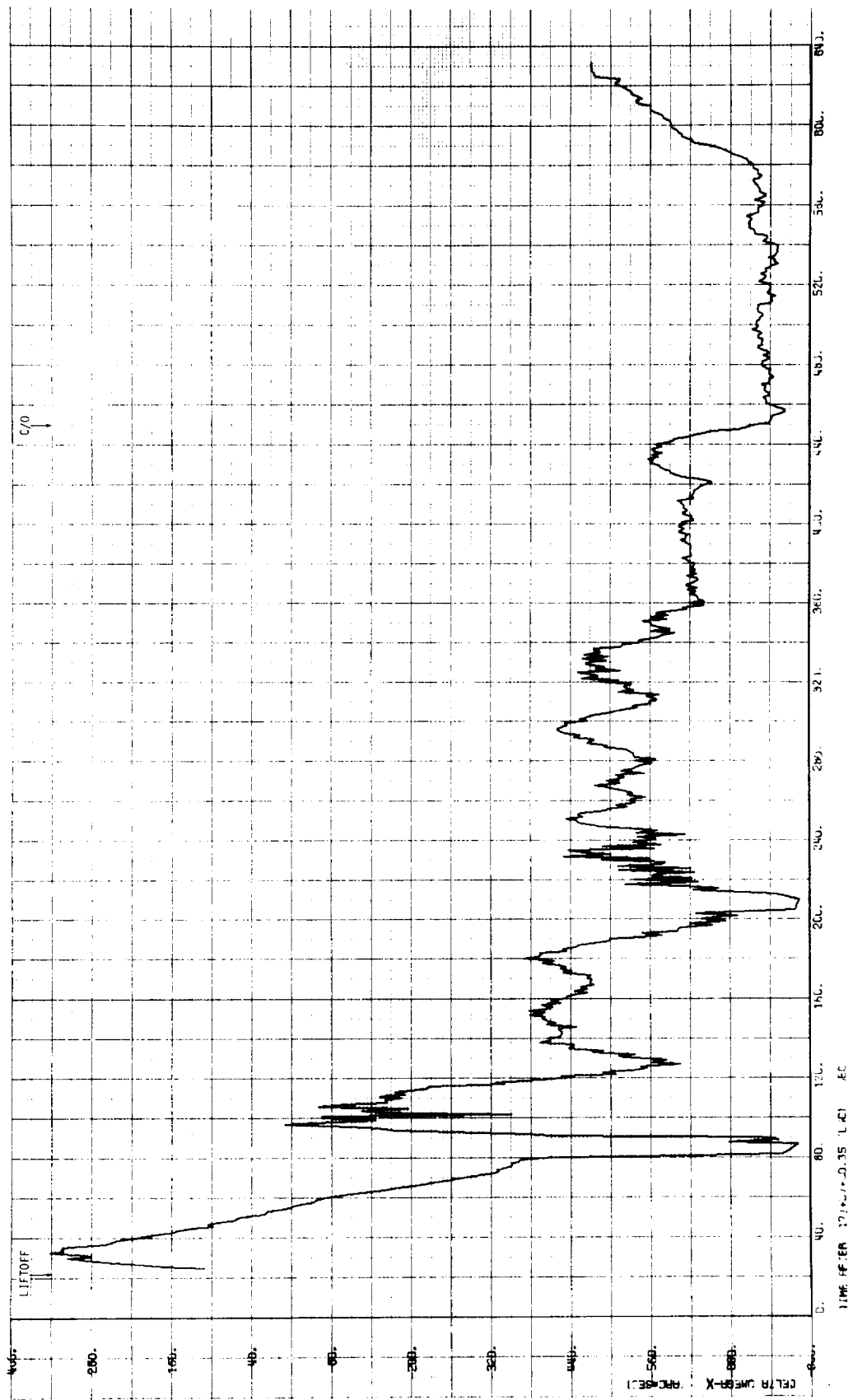


FIGURE 3-18. APOLLO 15 LM ASCENT AGS-PGS
INT. BODY RATE DIFFERENCE

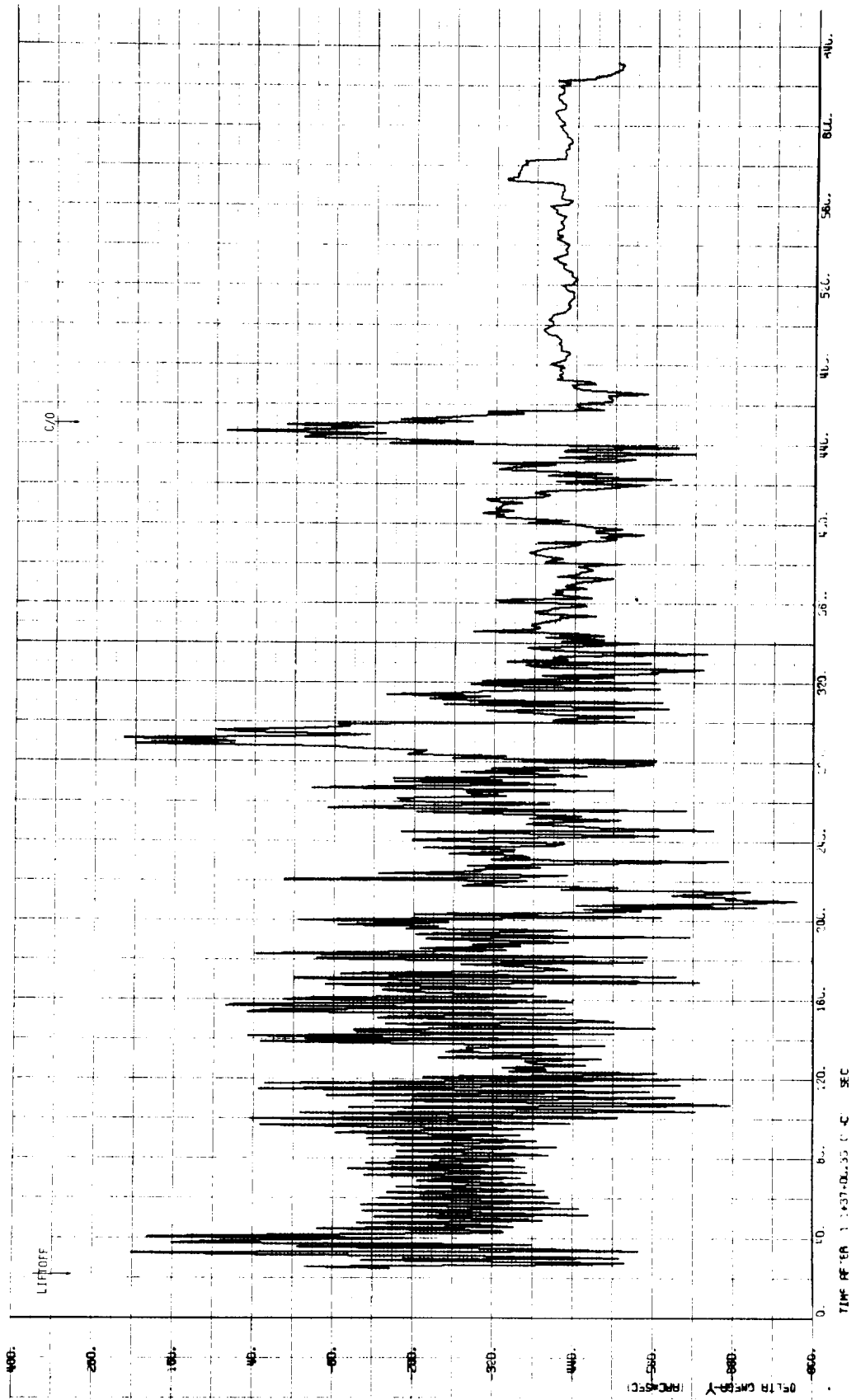


FIGURE 3-19. APOLLO 15 LM ASCENT AGS-PGS INT. BODY RATE DIFFERENCE

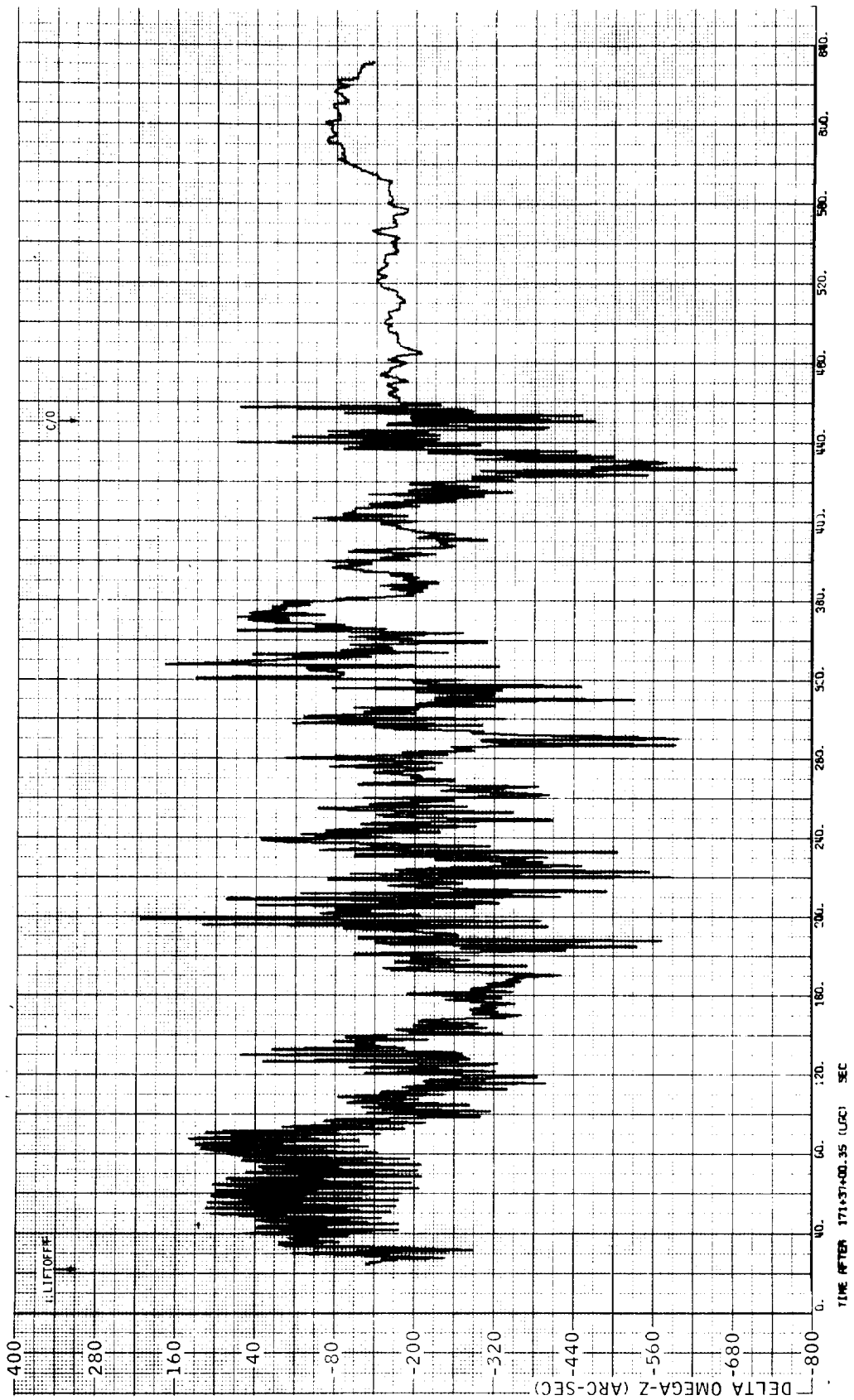


FIGURE 3-20. APOLLO 15 LM ASCENT INT. BODY RATE DIFFERENCE

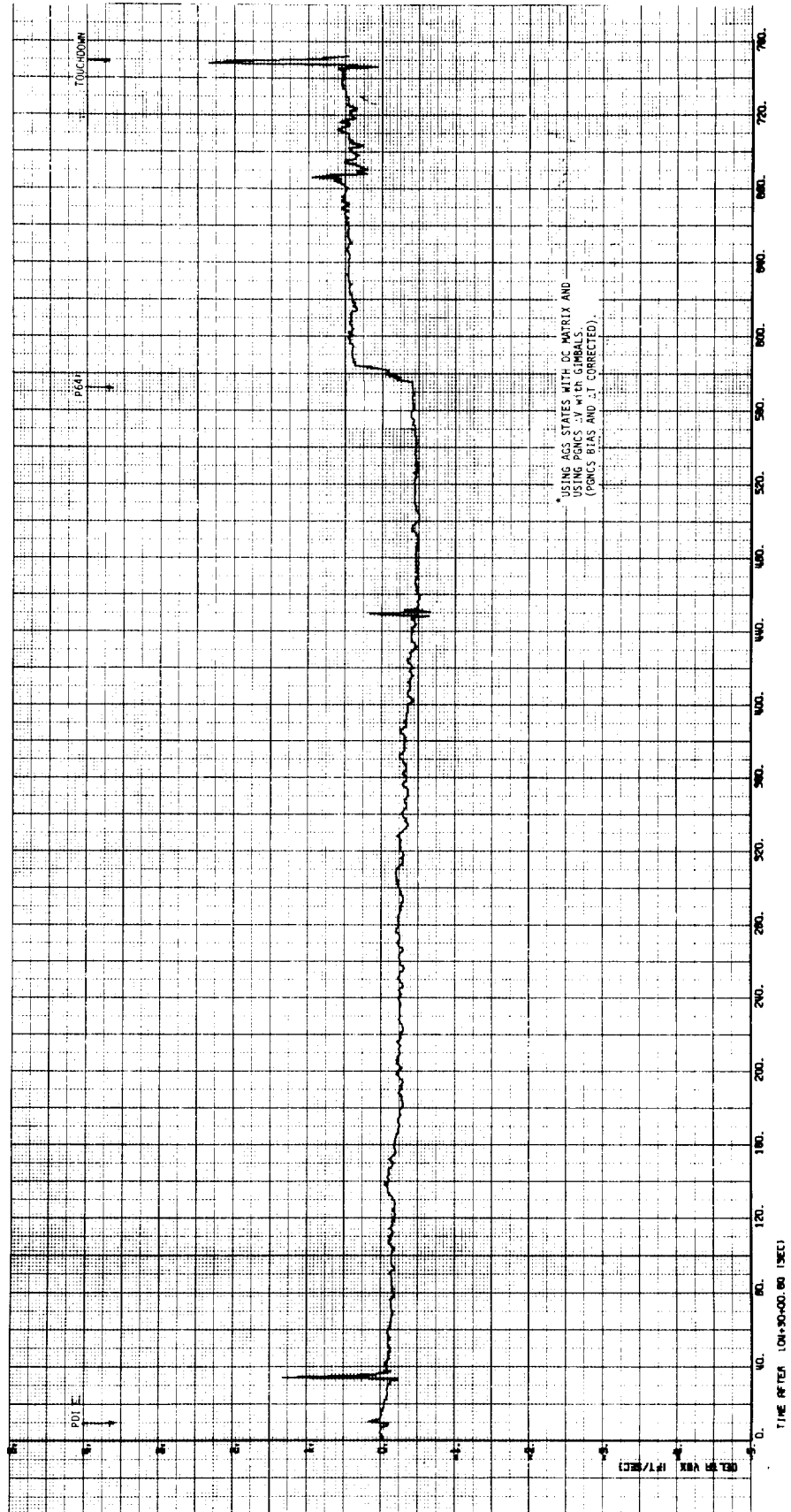


FIGURE 3-21. APOLLO 15 LM DESCENT DELTA VB (AGS-PGS)

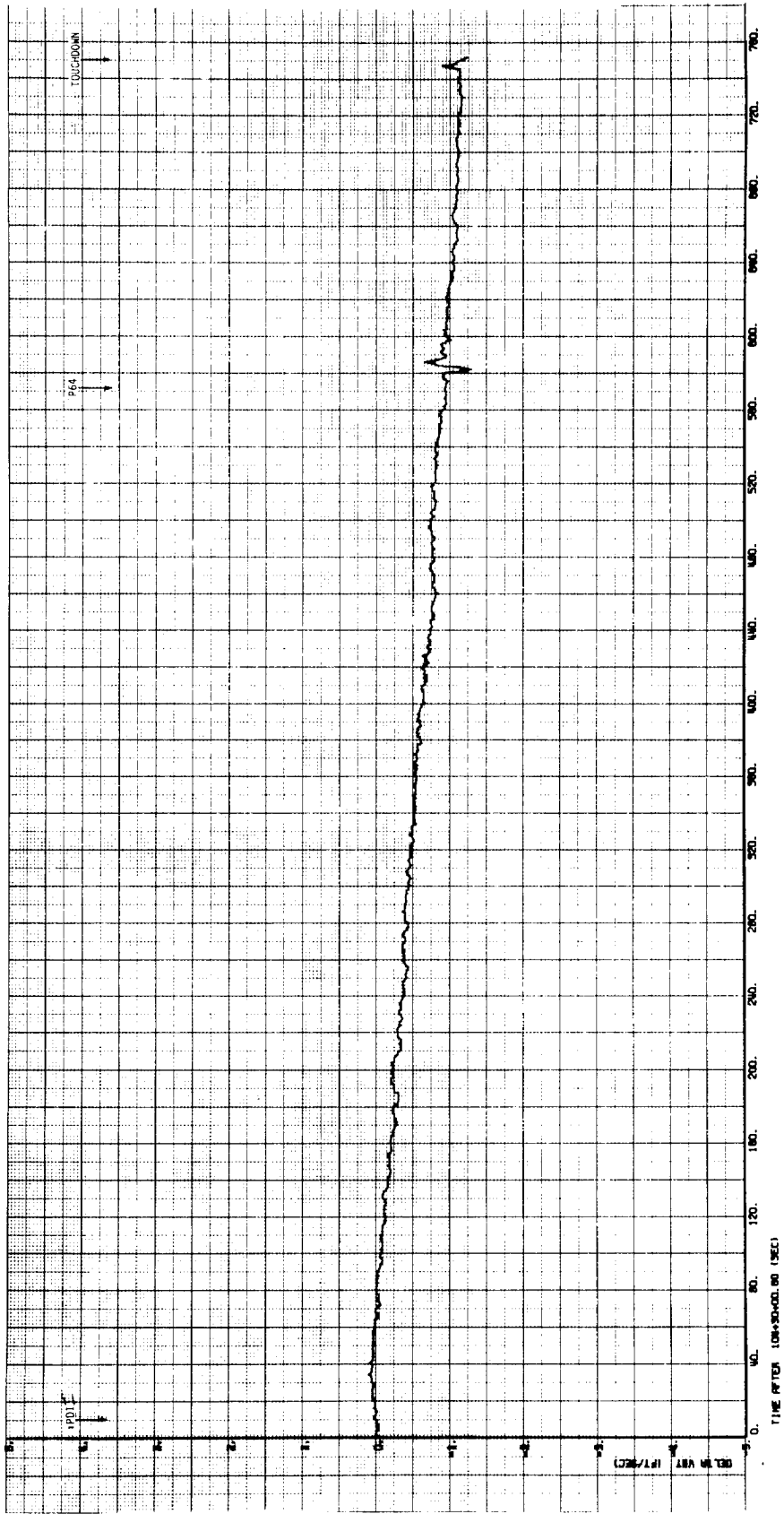


FIGURE 3-22. APOLLO 15 LM DESCENT DELTA VB (AGS-PGS)

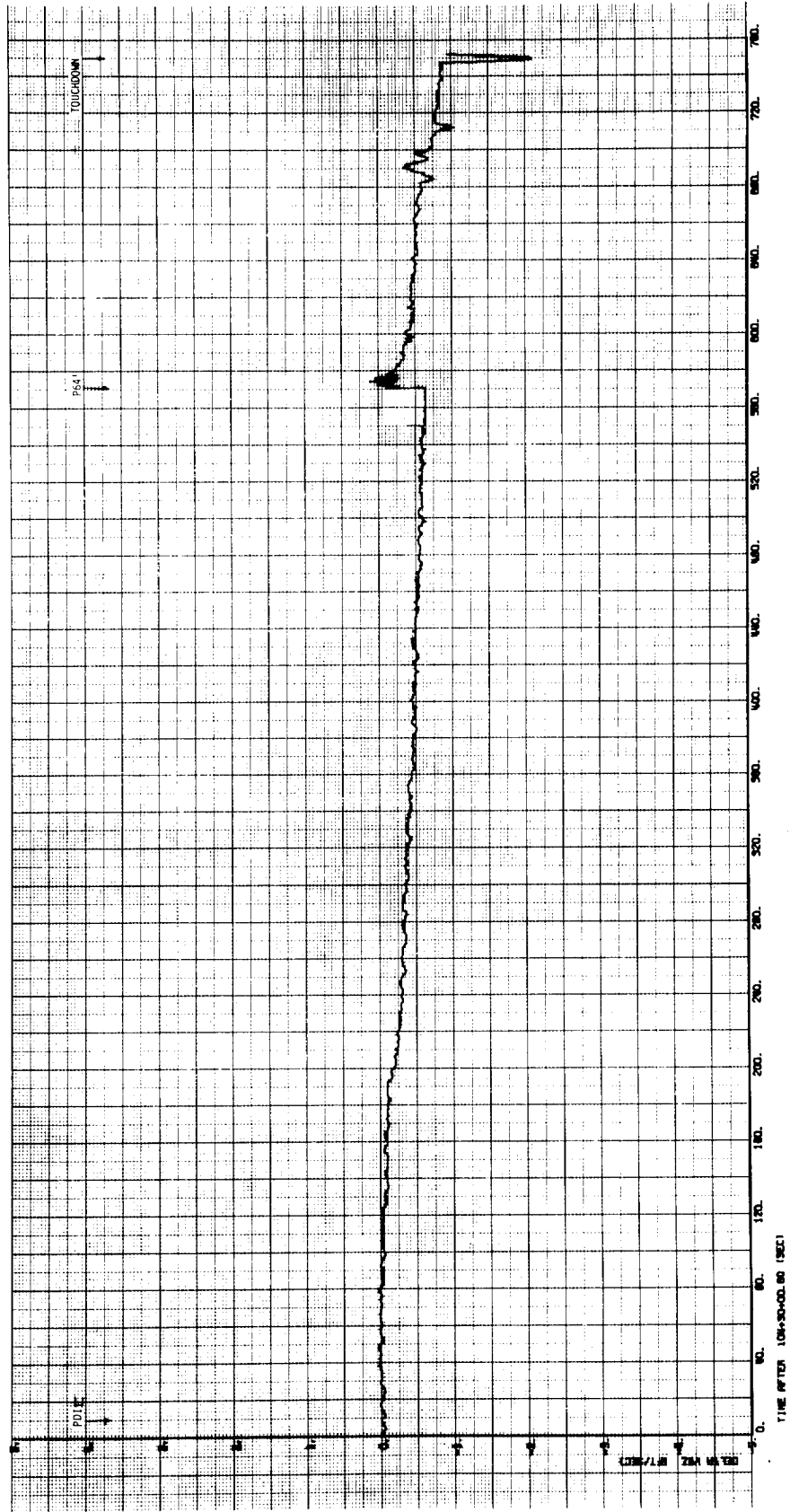


FIGURE 3-23. APOLLO 15 LM DESCENT DELTA VB (AGS-PGS)

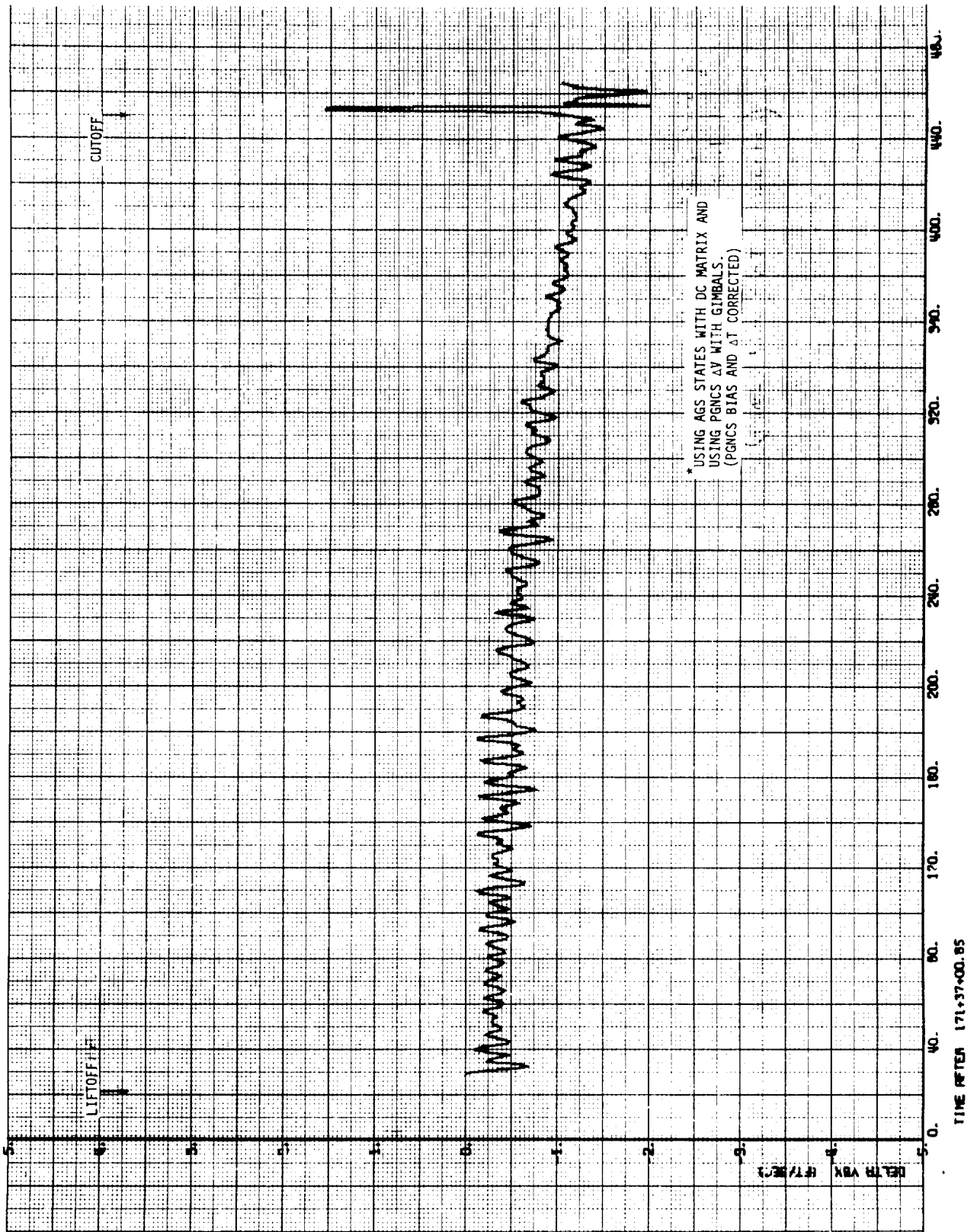


FIGURE 3-24. APOLLO 15 LM ASCENT DELTA VB (AGS-PGS)

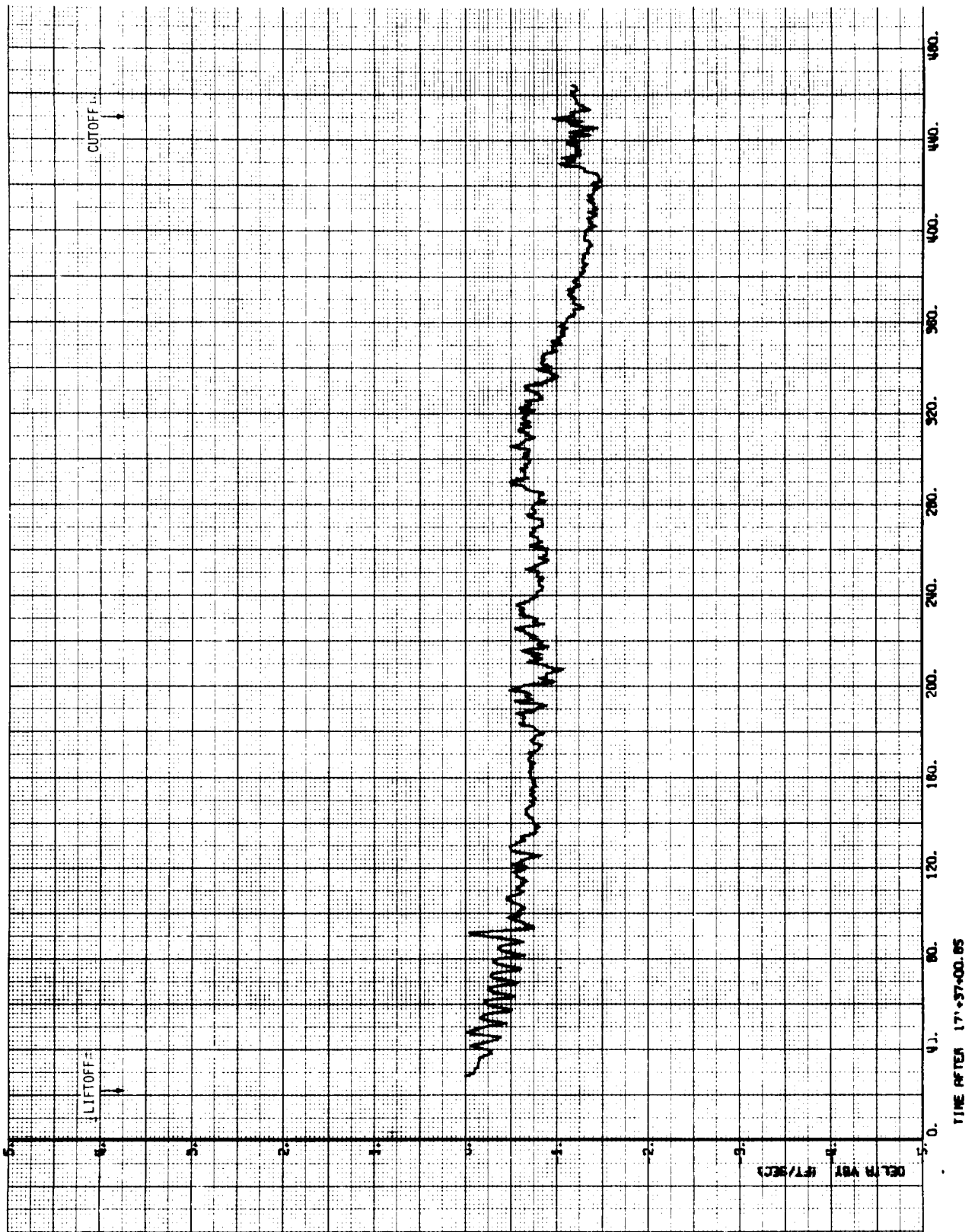


FIGURE 3-25. APOLLO 15 LM ASCENT DELTA VB (AGS-PGS)

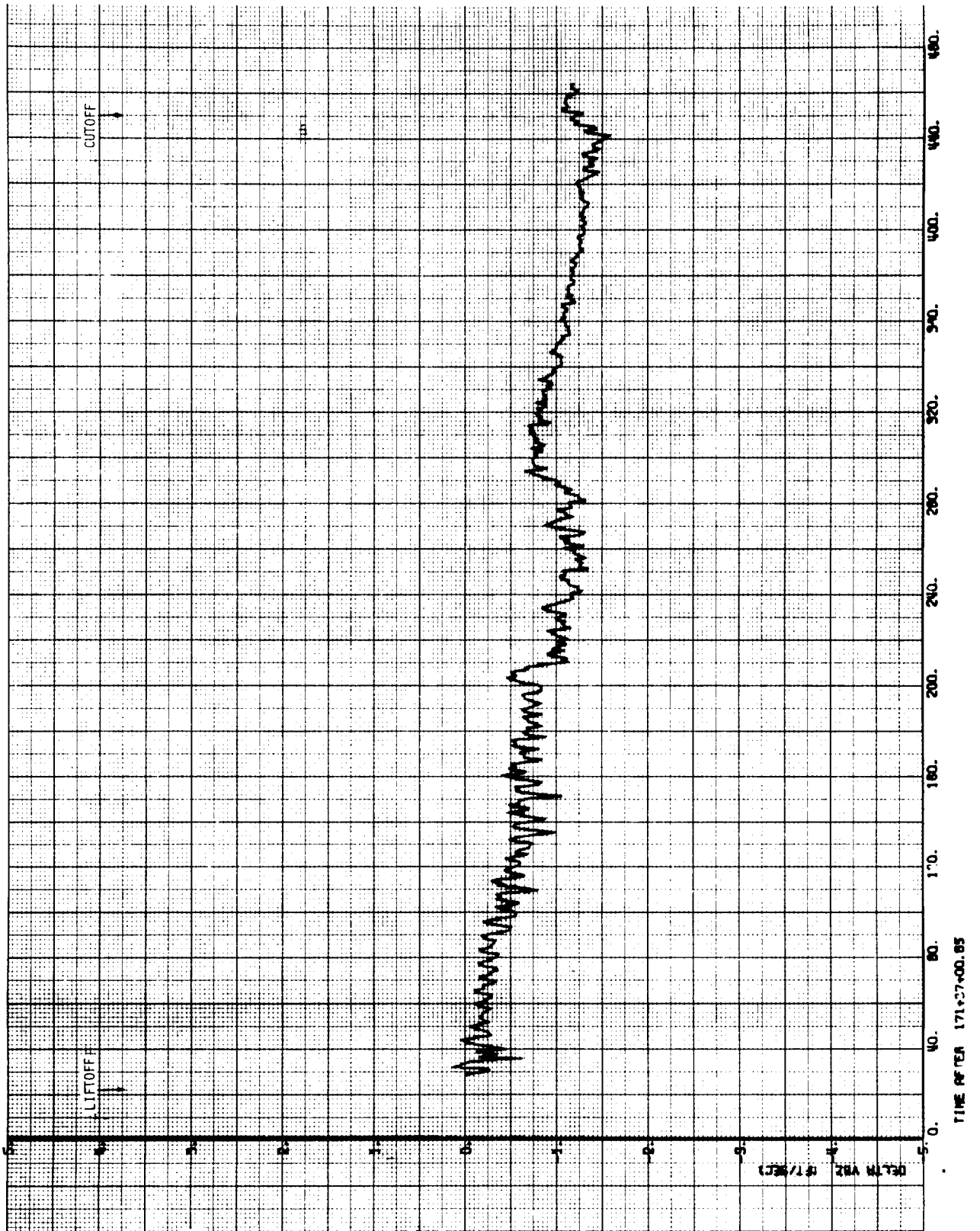


FIGURE 3-26. APOLLO 15 LM ASCENT DELTA VB (AGS-PGS)

4. DIGITAL AUTOPILOT PERFORMANCE

4.1 CSM DIGITAL AUTOPILOT

Analysis of the CSM DAP on Apollo 15 was primarily directed toward those phases of DAP operation which were new to this mission and toward peculiarities observed from initial review of the data. CSM Thrust Vector Control (TVC) DAP performance agreed closely with successful SPS burns of previous missions with one exception. A yaw SPS gimbal transient was detected during the TEI burn apparently caused by a CDU transient. The new universal tracking (P20) option 2 capability for orbital rate maneuvering was tested when the vehicle was in lunar orbit. Postflight analysis indicated the performance was acceptable. The use of universal tracking (P20) option 5 for S/C pointing to accommodate the SIMBAY experiments while in lunar orbit was also examined. When the CSM was docked to the LM and P20 option 5 was used, several occurrences of long duration jet firings were observed, when only minimum impulse firings were expected. Postflight analysis of the CSM DAP performance indicated that the orbital rate maneuver was interrupted periodically for a duration of approximately 20 seconds. When these interruptions occurred at a time when the vehicle attitude error was close to the deadband, large jet firings would occur as the DAP reverted to its attitude hold function of phase plane maintenance. Upon restoration of spacecraft pointing, jet firings were again required to re-establish the orbital rate. Detailed results from the above studies are presented below.

4.1.1 SPS Burn/Yaw SPS Gimbal Transient During TEI

A yaw SPS gimbal transient observed during the TEI burn was most likely the result of a CDU transient. Analysis of available telemetry data at the time of the transient indicate good correlation between DAP commands, SPS gimbal motion and CSM body rates. All data pertinent to the event are shown in Figure 4-1. As shown, the CDU's are only read-out on telemetry once per second whereas the DAP reads the CDU's every 40 ms. Gimbal commands are

also read once per second but fortunately the yaw command was read near the time the transient occurred. The gimbal trim command (YACTOFF) is read once per 2 seconds. The combination of YACTOFF and YCMD is the total DAP command to the SPS gimbal actuator. At the time of the transient the total DAP command changes from 0.12 degrees to 0.35 degrees, a change of 0.23 degrees.

The TVC DAP initial gain at the time of transient is 0.66 deg/deg. If the CDU outputs are examined in terms of the attitude error equations at the time of the transient, it can be shown that the yaw attitude error is related to the CDU's as follows:

$$\gamma_e = \text{yaw error} = -\cos \psi \sin \phi' (CDUY - CDUY_D) + \cos \phi (CDUZ - CDUZ_D)$$

where

$$\psi = CDUZ$$

$$\phi' = CDUX - 7.25^\circ$$

$$CDU_D = \text{Desired CDU angle}$$

Assuming the transient occurred in only one CDU, the magnitude of the CDU transient was computed as follows:

- a) Knowing the DAP gain and observed engine deflection, the attitude error (γ_e) was determined to be approximately 0.33 degrees.
- b) Using the gimbal angles at the time of the last telemetry sample, compute the CDU change required to cause the 0.33 degree DAP attitude error. Results were $(CDUY - CDUY_D) = 6.67^\circ$ or $(CDUZ - CDUZ_D) = 0.33^\circ$.

The CDUY case was discarded because transients of that size have not been observed in ground testing. Laboratory testing has isolated two types of CDU transients;

- 1) Fine error switch transients observed when the CDU is changing slowly and various low order bits remain unchanged for several minutes. The size of the transient is usually less than 0.24 degree and lasts for a second or less.

- 2) Coarse error switch transients observed when the CDU is at angles of $0^\circ + \text{integer multiples of } 45^\circ$. These transients are less than 0.34° and last for less than 50 milliseconds.

The CDUZ transient does not fit the second case because the gimbal was 0.68 degrees, not zero, but the conditions did meet the first case since the CDUZ was moving at a slow 0.012 deg/sec. The transients result from a design deficiency in the transistor switches of the CDU read counter. Since the problem causes only short term effects (less than a second) hardware changes have not been implemented.

In following the effects of the CDU transient, the SPS gimbal was driven from 0.19 degrees to 0.32 degrees, a peak change of 0.13 degrees. The SPS control authority for CSM only configuration is approximately 3 deg/sec^2 per degree of SPS gimbal travel, and the gain is negative. The rate gyro trace, which is 100 sample per second data, shows the body negative rate building to -0.02 deg/sec. Taking the average SPS positive deflection $\frac{0.13}{2}$ and time of deflection (200 ms) and multiplying by the SPS gain, an expected body rate of -0.04 deg/sec is computed, well within the sensitivity of the measurement data. In response to the engine deflection, the DAP detected the vehicle rate and attitude errors, and commanded a negative engine command of 0.17 degrees. Computing the expected vehicle rate for this deflection, a value of 0.08 deg/sec is obtained. Examination of the rate gyro data shows the yaw vehicle rate building to 0.06 deg/sec, again well within the granularity of the measurement data. An expected lag exists between the rate gyro data and the rapid engine deflections due to vehicle bending.

In summary, available data indicate that the DAP issued an erroneous SPS gimbal command which was most likely the result of a CDU transient. The DAP satisfactorily corrected for the subsequent vehicle rate and attitude errors within the following $540 \pm 20 \text{ ms}$ and the data were nominal for the remainder of the maneuver.

4.1.2 Universal Tracking Program - Option 2

CSM DAP performance during the CMC Universal Tracking Program P20, Option 2, was examined with particular reference to initial transients due to program start-up and the time to reach orbital rate. These effects were studied by comparing actual and desired rates, and actual and desired gimbal angles. Figures 4-2 and 4-3 present these quantities for the Y-control axis (the axis of greater rotation maneuver for Option 2) and X-control axis, respectively. It is seen that the Y-axis actual rate is considerably larger, during the first portion of the maneuver, than the orbital rate command (0.0506 deg/sec) required for landmark tracking. This is because of the necessity for first maneuvering to the appropriate attitude for tracking before the orbital rate alone is to be maintained. Hence, initiation of P20, Option 2 was verified to be nominal.

As Figure 4-2 indicates, the maneuver was performed with the actual CDUY following the desired CDUYD satisfactorily. The higher slope on the CDUYD curve early in the maneuver indicated the need for a rate greater than orbital rate at the start of the maneuver. Also, CDUYD finally approached a constant slope curve indicative of a constant orbital rate maneuver.

4.1.3 Universal Tracking Program - Option 5

During SIMBAY pointing in lunar orbit, frequent discontinuities in P20 were observed, which caused the DAP to perform an inertial attitude hold and interrupt the established orbital rate. When these discontinuities occurred, transients of 0.7° in each of the pitch and yaw attitude errors were caused and if the DAP deadbands were exceeded, the RCS jets would stop the vehicle rate. When the maneuver commands were resumed, the orbital rate had to be re-initiated. The circumstances leading to this start-stop jet firing sequence occurred rather frequently with the docked CSM/LM because of the nature of the gravity gradient torques. Analysis indicated the maneuver command terminations were correlated with the orbital integration routine which was being exercised at intervals of about 35 minutes. The remainder of this discussion will detail the sequence of events in P20 leading to the problem and will analyze the DAP response.

The SIMBAY vector is pointed downward along the local vertical during long periods of orbital rate maneuvering. In this attitude, the X-axis of the vehicle is horizontal. The SIMBAY vector is located about midway between the +Y and -Z axes of the vehicle and 45° from RCS Quads A and B. The roll orientation of the spacecraft is shown at the top in Figure 4-4. The vehicle is rotated 127.5° clockwise from the heads-up position relative to the lunar surface when vehicle +X is along the velocity vector. The jets shown in the top sketch are those that perform all the firings during the major RCS firings and just prior to such events.

The sketch in the lower half of Figure 4-4 shows the two X-axis orientations that were used for SIMBAY experiments. The long duration orbital maneuvers were performed with the +X axis pointed uprange as shown on the right. The orbital rate direction is indicated by the arrows and yields the pitch and yaw rates indicated below each sketch.

The gravity-gradients are not aligned with the control axes and do not produce predictable DAP phase-plane trajectories. Gravity-gradient torques are parallel to the orbital rate axis and are proportional to the attitude deviation from the horizontal. Pitch and yaw attitude and rate errors are a combination of errors in both the vertical and horizontal planes; only by combining pitch and yaw attitude errors can one compute the angular acceleration produced by gravity-gradients in either of the control axes. Hence, the DAP phase-plane was abandoned as a tool for analyzing DAP performance in the presence of gravity-gradient torques.

ATTITUDE ERROR ANOMALY

The discontinuity in P20 which causes the large jet firings was discovered from a cross-plot of pitch and yaw attitude errors shown in Figure 4-5. The pitch and yaw axes are rotated 45° in Figure 4-5 to correspond to the roll orientation shown in Figure 4-4; as a result, the attitude errors in the vertical plane are measured up and down the page and cross-range attitude errors are measured left and right. The effect of gravity-gradients is to cause the errors in the vertical plane to increase in either direction from the horizontal.

In addition, the gravity-gradient torque increases with the vertical attitude error and causes the trace in Figure 4-5 to reach the upper or lower corners of the plot. Eventually, a minimum-impulse limit-cycle is established near one of these two corners. The gravity-gradient torques force the vehicle toward the DAP deadbands, and the RCS jets fire alternately in pitch and yaw to reverse the vertical rate. These limit-cycles are so small for the docked vehicle that they are barely visible in Figure 4-5.

Several discontinuities in DAP attitude errors can also be seen in Figure 4-5. The most obvious discontinuity appears near the origin at 86:38:17 GET and does not cause any jet firings to occur since the DAP deadbands were not exceeded. No change in vehicle motion was responsible for the sudden change in DAP attitude errors; the change was due to the termination of orbital rate commands and the corresponding CDUD increments. Before and after the discontinuity, the trace is moving from left to right at a high rate. Two pitch firings occur when the deadband is encountered, and the horizontal and vertical rates are both reversed. As the trace moves slowly upward and toward the left, a second discontinuity occurs (86:59). As the plot continues to the left, the vertical rate is reversed by gravity-gradient torques which force the curve toward the lower corner in Figure 4-5. A tiny (0.3° peak-to-peak) minimum-impulse limit-cycle is established until a third discontinuity occurs (87:40); this time, both DAP deadbands are exceeded and major firings occur.

These major firings are both unnecessary and undesirable. If the jets are fired, the orbital rate will be stopped and additional jet firings will be required later to re-establish the vehicle rate. During Apollo 15 SIMBAY operations, all pitch and yaw firings were performed by the -X jets because of impingement constraints and these un-coupled firings produce a delta-V of 0.1 ft/sec for each major firing. The impulses are not predictable and may produce significant errors in the ground and onboard orbital navigation computations.

Enlargements of two of these attitude error anomalies are shown in Figures 4-6 and 4-7. Figure 4-6 is a plot of the first discontinuity in the curve in Figure 4-5 at GET 86:38:17. Dots indicate one or more 2-second samples of the pitch and yaw attitude error in Figure 4-6, while solid lines were plotted from occasional data points. At the start of the plot in Figure 4-6, the data points are fairly dense even though the DAP rate error is higher than usual for SIMBAY operations. At GET 86:38:17, the data points break sharply toward the lower left for 20 seconds due to the erroneous commands to the DAP. At GET 86:38:37, the DAP is commanded to maneuver back to the local horizontal, and this brings the DAP error back to the line established before the 0.91 degree vertical transient occurred. The attitude error transient in Figure 4-6 had no effect on the motion of the vehicle because the DAP deadbands were not exceeded, and because the change occurred in the commanded attitude, not the actual attitude.

Figure 4-7 is a close-up of the extreme lower corner of Figure 4-5 25 times. The heavy curve plots the attitude errors prior to the loss of commands. The thin line connecting the circled data points is a plot of the DAP pitch and yaw attitude errors after the orbital rate commands are removed. The plot starts at the upper right (87:27:05) in Figure 4-7 where a small pitch firing occurs and crosses the yaw deadband at a high rate. A larger yaw firing reverses the vertical rate and the trace drifts slowly toward the left until the yaw deadband is encountered once more. The first minimum impulse occurs on the far left and is followed by four additional minimum impulses in pitch and yaw and one roll firing which couples into pitch.

The first circled point in Figure 4-7 indicates the last data point where the DAP attitude errors are normal. Starting at the second circle, the two curves separate; the arrow shows the direction that the vehicle takes with respect to the local vertical reference, while the circles plot the DAP errors which move rapidly in the opposite direction. Within two seconds (third circle), major jet firings begin and continue intermittently until the attitude errors stabilize (circle 5 at bottom). The attitude errors

decrease slowly until the commands resume at circle 10 near the pitch deadband. A maneuver is commanded at a rate which is higher than the orbital rate in order to bring the center of the DAP deadbands back to the local horizon. This causes the attitude error plot in Figure 4-7 to move rapidly across the page from the bottom to the top (circle 10 to 14).

Figure 4-8 is a plot of the commanded and measured gimbal angles at the time of the major firings plotted in Figures 4-5 and 4-7. For purposes of demonstration, the inner gimbal angles can be considered to be angles in the orbital (vertical) plane. Prior to the attitude error anomaly, both curves are following the orbital rate slope with a 7° vertical attitude error determined by the 5° control deadbands. This orbital rate maneuver should be expected to continue indefinitely with a precisely constant pointing error. Instead, the orbital rate maneuver was stopped by terminating the command increments at GET 87:39:59 as shown by the CDUYD curve in Figure 4-8. As the measured gimbal angle (CDUY) continues to decrease, the attitude error increases and causes the jet firing to reduce the vehicle rate to 23% of the orbital rate. After 20 seconds, the CDUYD increments are larger than before and denote a catch-up maneuver to place the CDUYD curve back on the "ORB RATE" line.

Invariably, one other event occurs in the same telemetry time frame with the start of the command discontinuity. In every case studied, the discontinuity in CDUYD begins at the same time-tag as the loading of the new permanent state vectors at the end of the orbital integration routines. The mechanism by which the termination of the orbital rate commands is triggered at the completion of the orbital integration has been studied by MIT/CSDL and work around procedures are being developed.

After a major firing occurs, the DAP deadband is crossed and a limit cycle is established in the upper corner of Figure 4-5. The two discontinuities indicated at the top of Figure 4-5 cause no major jet firings. Small firings do occur after the DAP commands are restored. During the attitude-error anomaly, the DAP is unaware of the true vehicle motion during a period of 40

to 60 seconds. During this period, small initial rates and gravity-gradient torques can cause the vehicle attitude error to increase, so that when the orbital rate maneuver is resumed after the interruption, the attitude error can cause small jet firings. These firings are typically smaller than those encountered at the negative attitude error limits.

This P20 limitation was studied by MSC flight controllers and several operational considerations have been proposed for Apollo 16 to help alleviate the problem. The most significant procedural work-around is the setting of the CMC SURF FLAG (bit 8 of FLAGWORD 8) to prevent LM state vector integration. This will result in approximately four seconds of interruption of the P20 orbital rate maneuver (for integration of the CSM state vector only) compared to the twenty seconds required for both LM and CSM state vector integration. Consequently, the errors accumulated during the shortened interruption period will be greatly reduced, which will reduce the number of times the deadband is exceeded. Furthermore, if the deadband is exceeded, the amount which the deadband is exceeded is decreased and the resultant firings will be smaller than those observed in the Apollo 15 mission. Other operational considerations are limiting the time tag on state vector uplinks to be within 30 minutes of uplink time, limiting the use of programs that allow P20 to run in the background and which prevent periodic state vector integration, and also limited use of extended verbs that require state vector integration.

4.2 LM DIGITAL AUTOPILOT

LM Digital Autopilot performance was reviewed during descent and ascent to identify any major differences between this mission and previous missions. On the whole, the DAP performance was found to be nominal and in agreement with previous lunar landings.

4.2.1 LM DAP Performance During Powered Descent Braking Phase

Powered Descent Initiation (PDI) was effected using LGC Braking Phase Program P63. The conditions observed on the DSKY at DPS ignition were:

LM Inertial Velocity Magnitude:	5559.6 fps
Altitude Rate:	-35.7 fps
Altitude:	52,899 ft

The RCS propellant consumption and jet on-time for attitude control during P63 were:

+U' axis:	1.35 lbs., 3.633 sec.
-U' axis:	1.51 lbs., 4.072 sec.
+V' axis:	2.25 lbs., 6.063 sec.
-V' axis:	0.60 lbs., 1.613 sec.
+P axis:	1.52 lbs., 4.095 sec.
-P axis:	1.64 lbs., 4.426 sec.

The unbalanced usage in the V' axis is primarily the result of c.g. offset from the engine thrust vector which existed at the time of PDI and slow response time of the gimbal trim system. Total RCS propellant consumption during P63 was 8.87 lbs and is slightly more than 7.06 lbs used for Apollo 14 but less than the 16 lbs used in Apollo 12. A plot of RCS propellant consumption during powered descent is given in Figure 4-9. It is noted, however, that a comparison of propellant consumption of previous missions with Apollo 15 should be done with special care for the following reasons: Apollo 15 was a different vehicle of greater mass and it utilized a different steering profile to achieve a trajectory of greater rate of descent.

DAP estimated body rates indicate that slosh oscillations started later in the burn (420 seconds compared to 270 seconds for Apollo 14) and with lower amplitude than on previous flights. As noted previously, the

LM-10 vehicle moments of inertia were considerably different (greater overall mass because of larger DPS tanks, more propellant and the Lunar Rover) from those on earlier flights. Also, the greater rate of descent of the Apollo 15 trajectory contributed to greater mass at any given time during the burn. However, it is of interest to note that the 150 second longer burn before slosh initiation resulted in the propellant onboard at this time being only 38% (of that used from P63 initiation to touchdown) compared to 52% for Apollo 14.

In summary, nominal response was observed during P63 for the Apollo 15 Powered Descent Burn.

4.2.2 LM DAP Performance During Powered Descent Approach Phase

The conditions at the entrance to P64 observed on the DSKY were:

LM Inertial Velocity Magnitude:	318 fps
Altitude Rate:	-135.3 fps
Altitude:	6,733 ft

Upon entering P64, the attitude error deadband was changed from 1.0 degree to 0.3 degree. The automatic pitchover maneuver was started immediately and the total pitchover maneuver was -40.2 degrees. The maximum estimated pitch rate during the maneuver was -11.06 deg/sec, slightly larger than Apollo 14 but is consistent with the fact that the Apollo 15 pitchover maneuver was 9 degrees greater than the Apollo 14 pitchover maneuver.

The RCS propellant consumption and jet on-time for attitude control during P64 were:

+U' axis:	1.58 lbs., 4.266 sec.
-U' axis:	2.19 lbs., 5.909 sec.
+V' axis:	1.27 lbs., 3.420 sec.
-V' axis:	2.38 lbs., 6.428 sec.
+P axis:	1.78 lbs., 4.781 sec.
-P axis:	1.79 lbs., 4.820 sec.

The total RCS propellant required for attitude control during P64 was 10.99 lbs. This is about 40% greater than the 7.83 lbs for Apollo 14. The increase is consistent with a heavier vehicle.

In summary, nominal response was observed during P64 for the Apollo 15 Powered Approach Burn. Attitude control of the heavier vehicle, however, resulted in 40% increase in RCS propellant consumption compared to Apollo 14.

4.2.3 LM DAP Performance During Powered Descent Landing Phase

The LM DAP performance during P66 defies exact comparison because of the manual control mode and the individual pilot choice in landing technique.

The conditions observed on the DSKY at the entrance to P66 were:

Horizontal Velocity:	29.8 fps
Altitude Rate:	-11.9 fps
Altitude:	331 ft

The maximum LGC estimated body rates at touchdown were:

OMEGAP:	-14.21 deg/sec
OMEGAQ:	0.52 deg/sec
OMEGAR:	-2.51 deg/sec

The rate in roll was much higher than the corresponding one in Apollo 14; this is attributed to the fact that one leg of the LM landed in a small crater.

The RCS propellant consumption and jet on-time for attitude control during P66 were:

+U' axis:	4.63 lbs., 12.486 sec.
-U' axis:	5.59 lbs., 15.070 sec.
+V' axis:	5.76 lbs., 15.537 sec.
-V' axis:	4.69 lbs., 12.643 sec.
+P axis:	1.47 lbs., 3.936 sec.
-P axis:	0.06 lbs., 0.148 sec.

The total RCS propellant consumption for attitude control during P66 was 22.20 lbs. This is a substantial reduction of 66% from the 64.96 lbs required for Apollo 14. This reduction is primarily the result of a more rapid and monotonic descent with negligible hovering using manual control before touchdown.

4.2.4 LM DAP Performance During Ascent

The maximum attitude errors and rate errors near liftoff were:

P ERROR	-1.02 deg	OMEGAP ERROR:	3.17 deg/sec
U'ERROR:	-2.19 deg	OMEGAU' ERROR:	-3.01 deg/sec
V'ERROR:	-4.05 deg	OMEGAV' ERROR:	8.66 deg/sec

The CDUY output indicated a pitchover of approximately 56.9 degrees which lasted for 10 seconds. During this interval the maximum pitch rate was 15.64 deg/sec and the maximum angular acceleration was 11.66 deg/sec². This pitchover was similar to that in Apollo 14 in which the same maneuver was performed in 9 seconds with a comparable pitch rate but lower peak angular acceleration. This is consistent with the fact that the Apollo 15 pitchover was 5.7 degrees greater than for Apollo 14.

The ascent burn was performed with the APS interconnect open such that the RCS jets consumed APS propellant. About 67.86 lbs of APS propellant was used by the RCS jets for attitude control. This consumption was 4 lbs less than for Apollo 14.

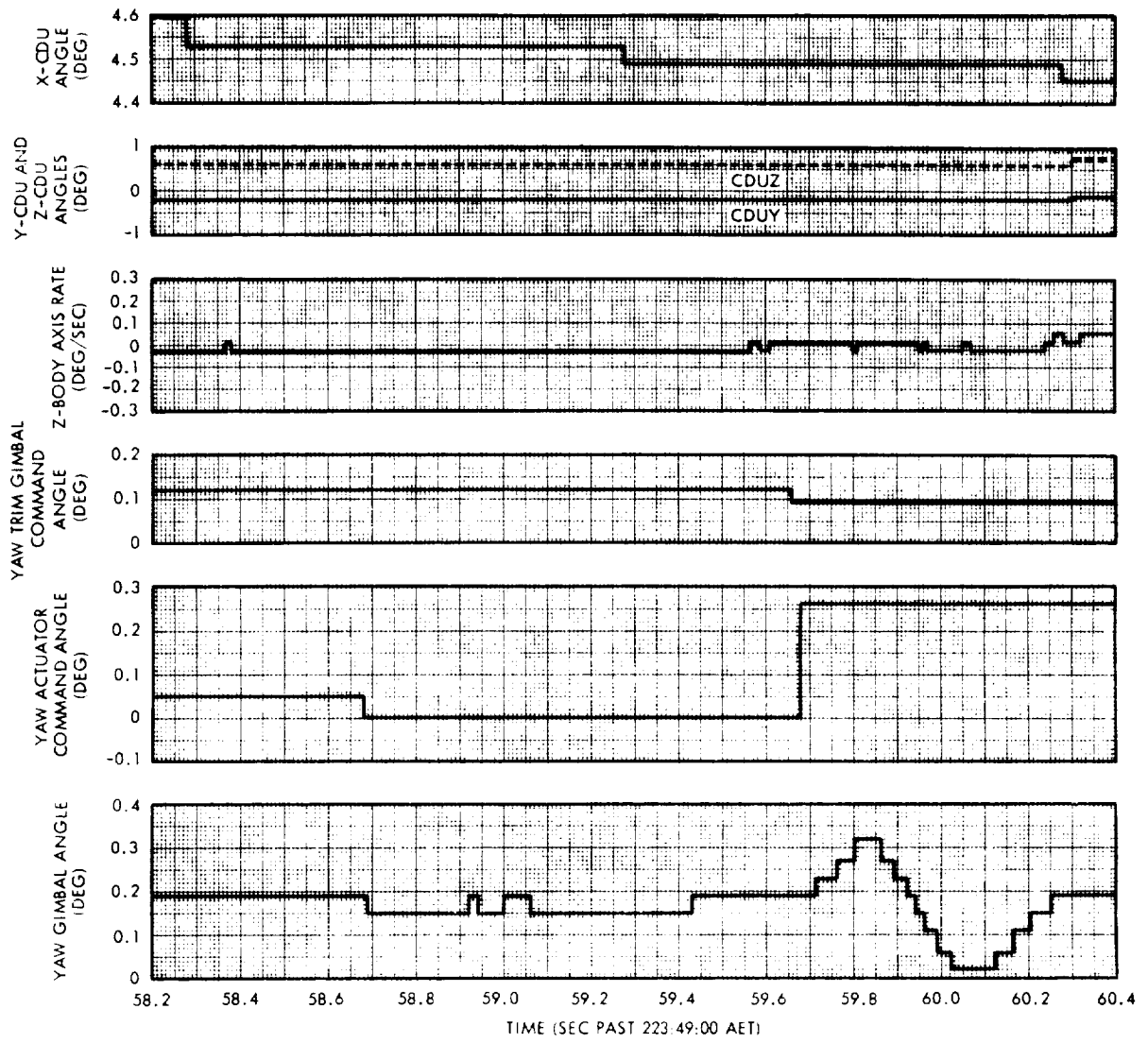


FIGURE 4-1. YAW SPS GIMBAL TRANSIENT DURING TEI

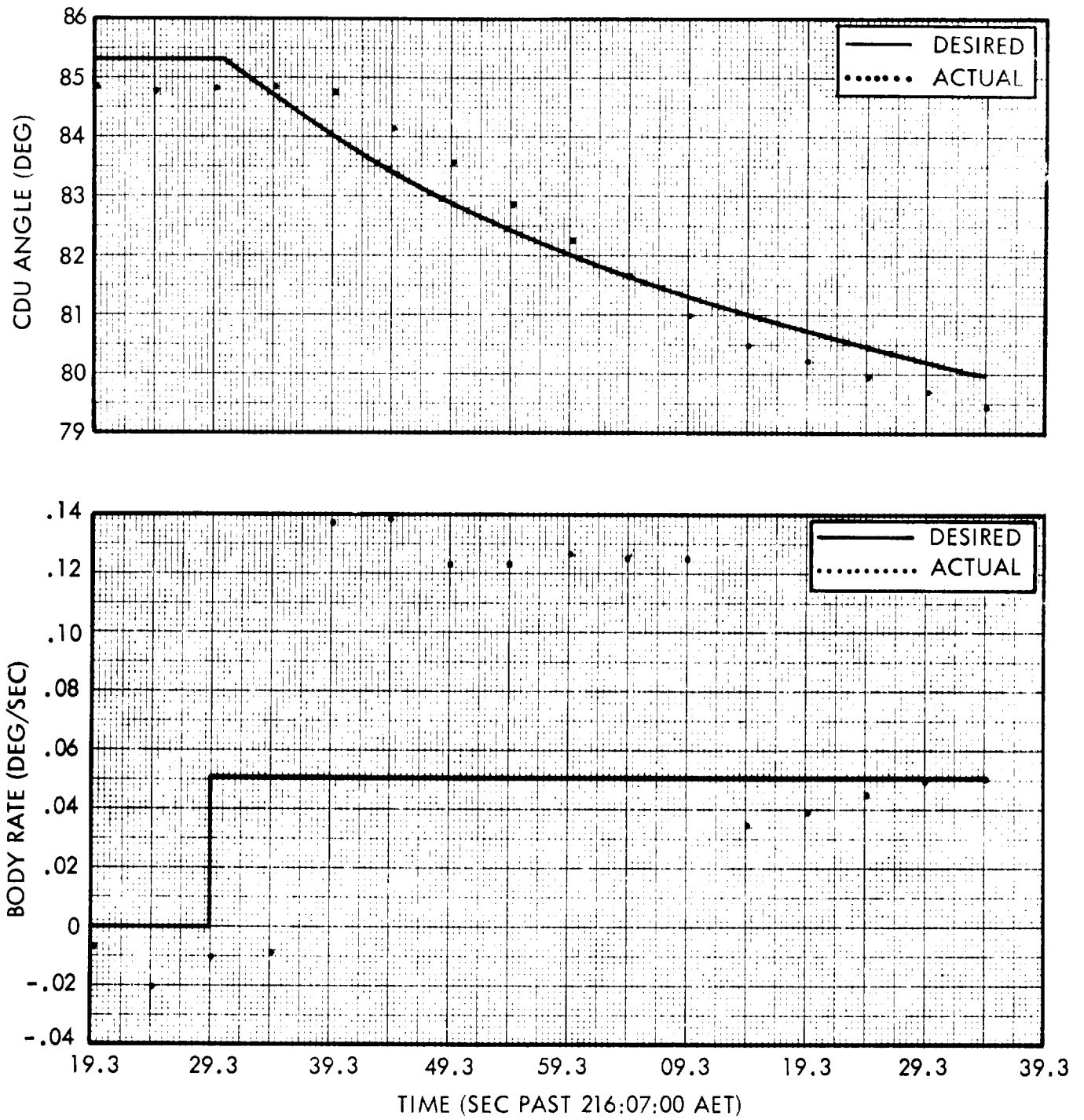


FIGURE 4-2. CSM Y-CONTROL AXIS RATES AND CDU ANGLES DURING CMC PROGRAM P20

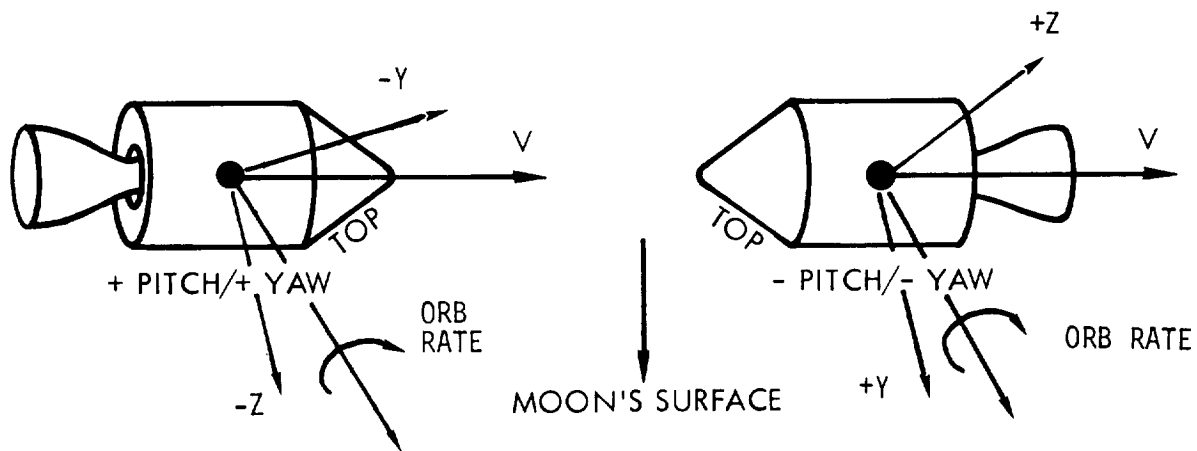
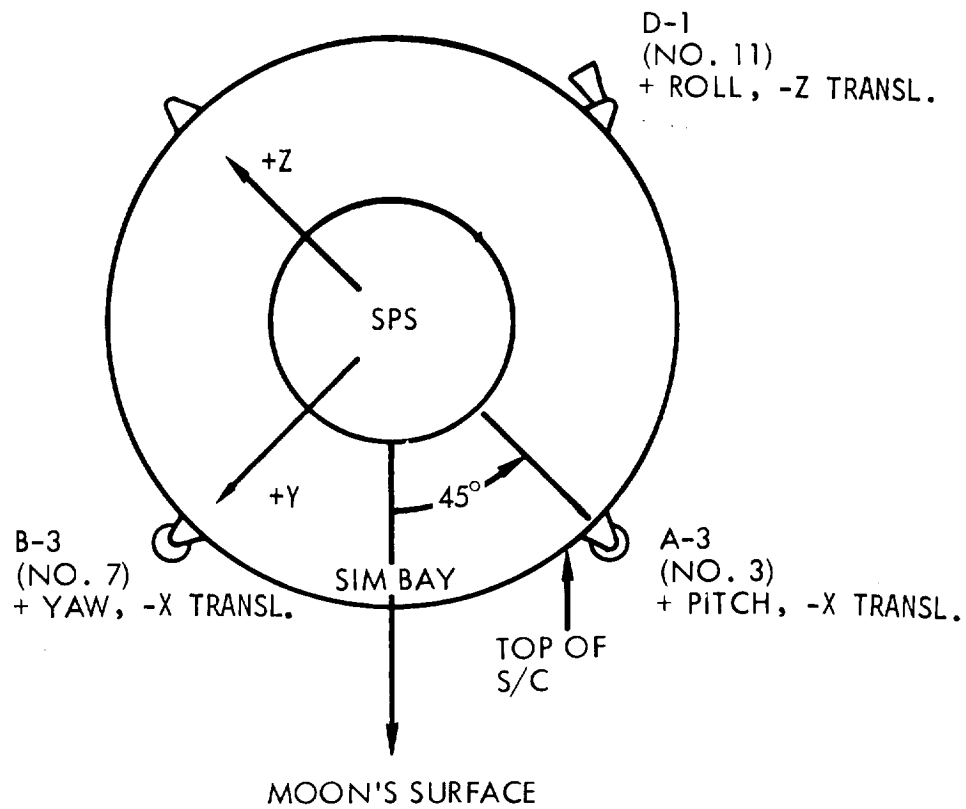


FIGURE 4-4. VEHICLE ORIENTATION

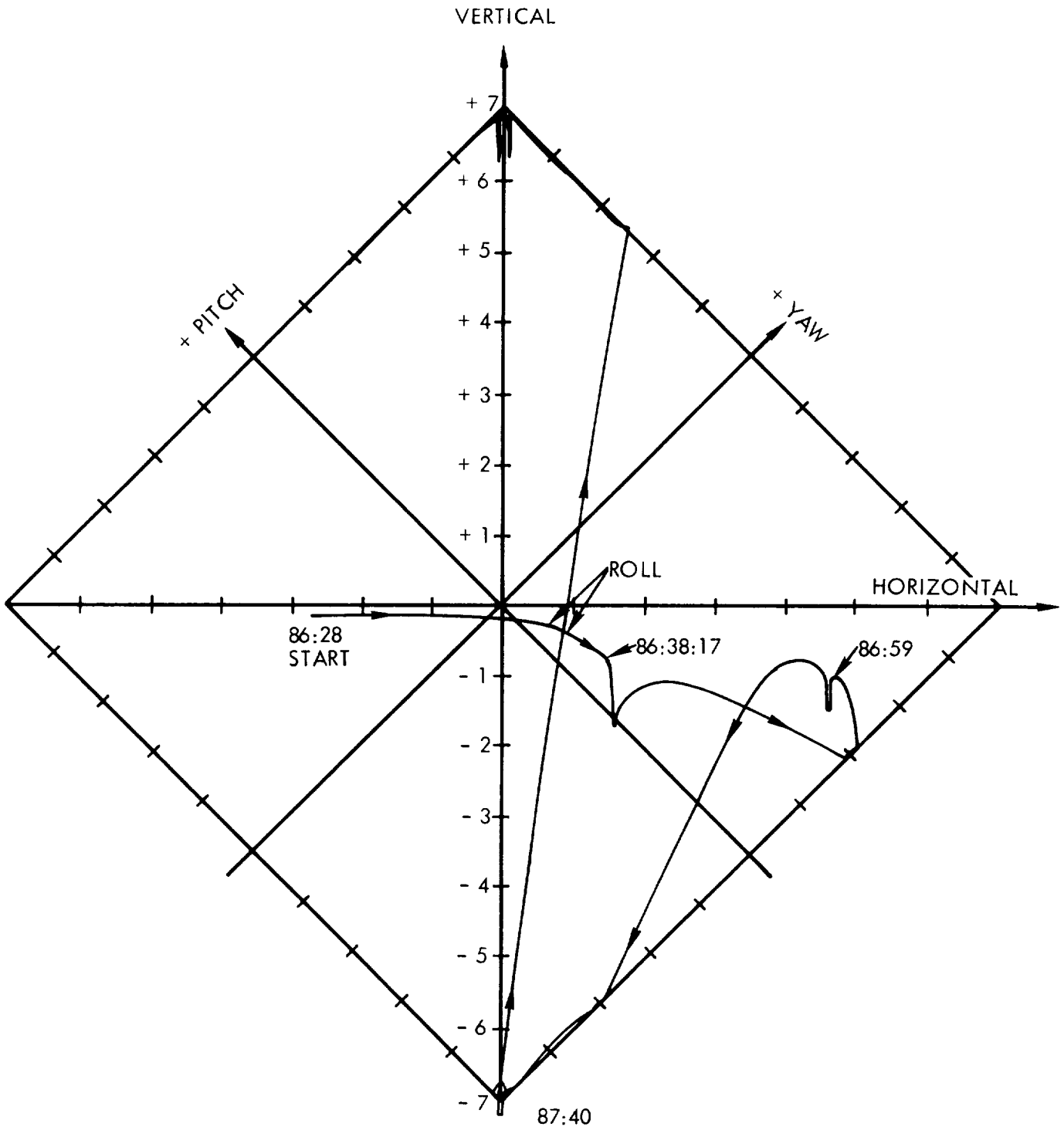


FIGURE 4-5. ERROR CROSSPLOT

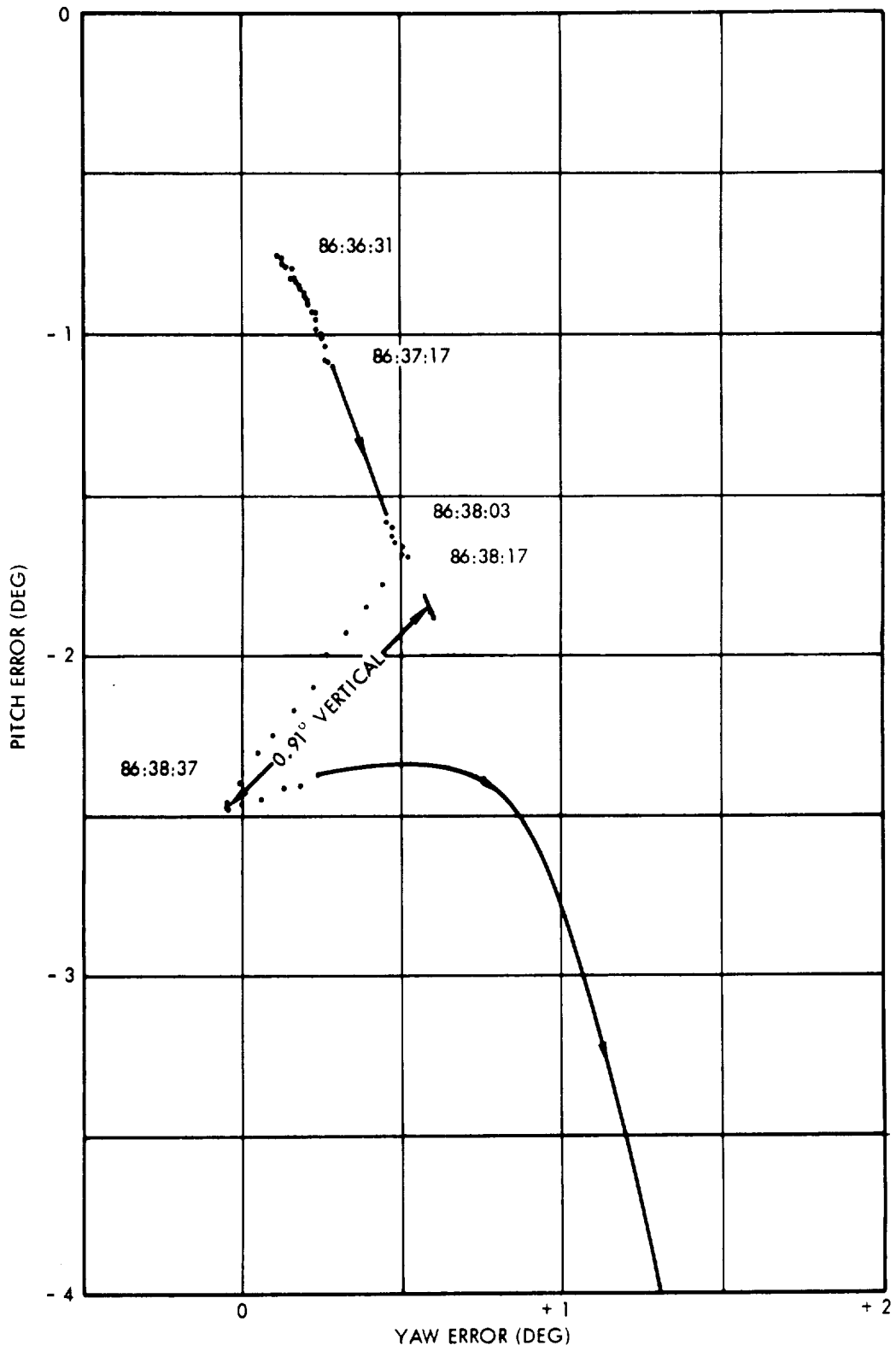


FIGURE 4-6. ENLARGEMENT OF ATTITUDE ERROR ANOMALY

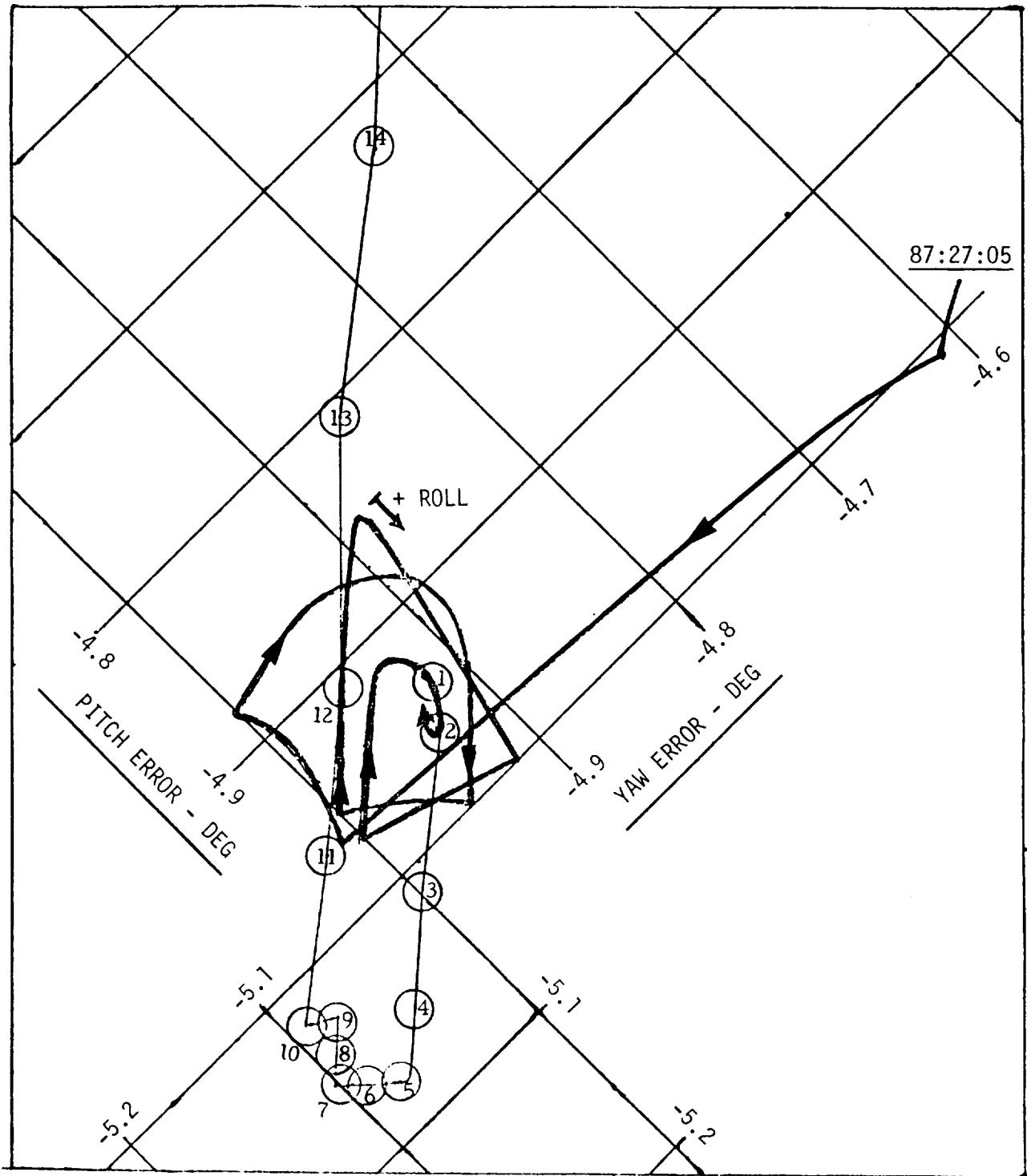


FIGURE 4-7. MAJOR JET FIRINGS

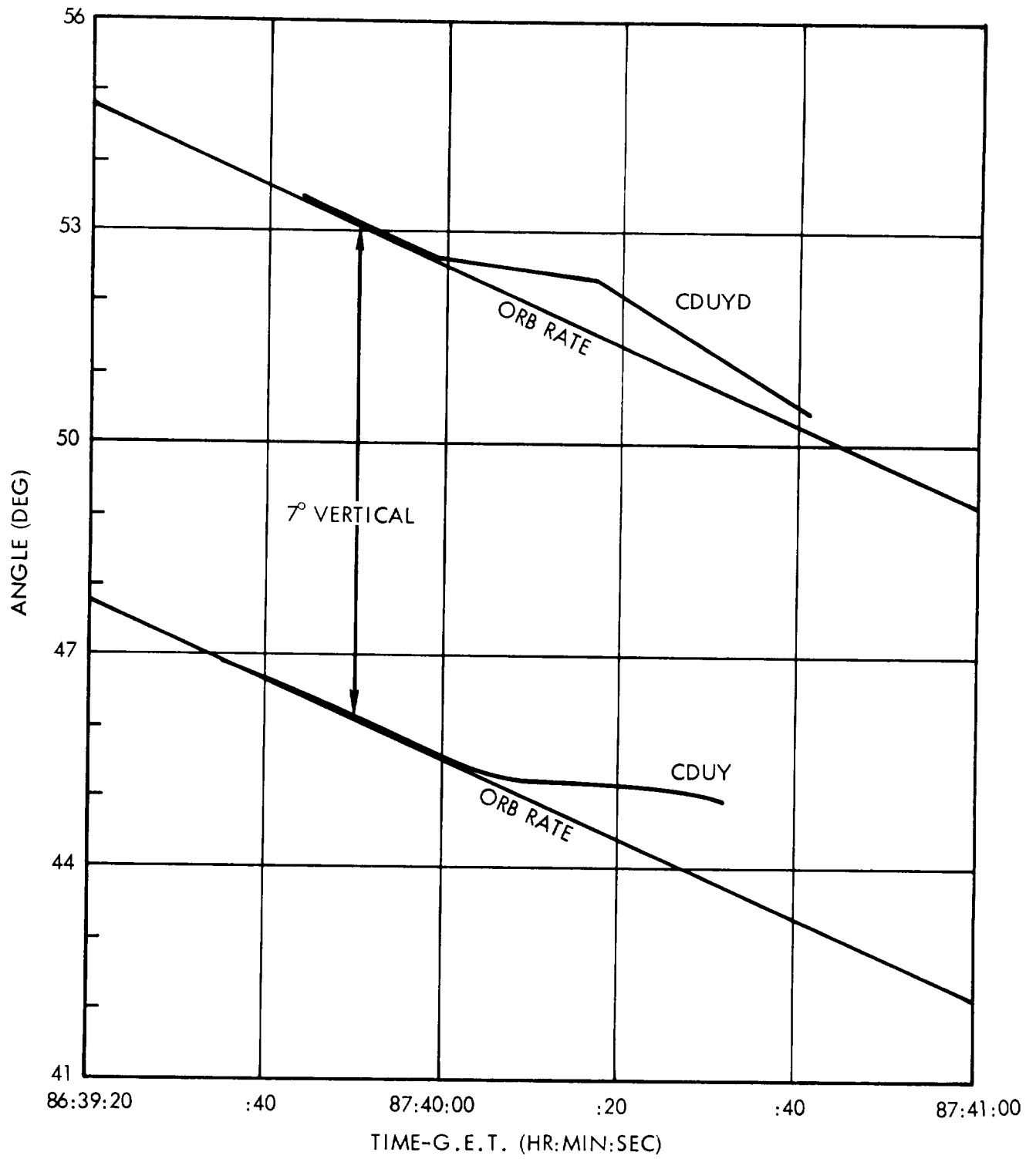


FIGURE 4-8. COMPARISON OF GIMBAL ANGLES AND COMMANDS DURING ANOMALY

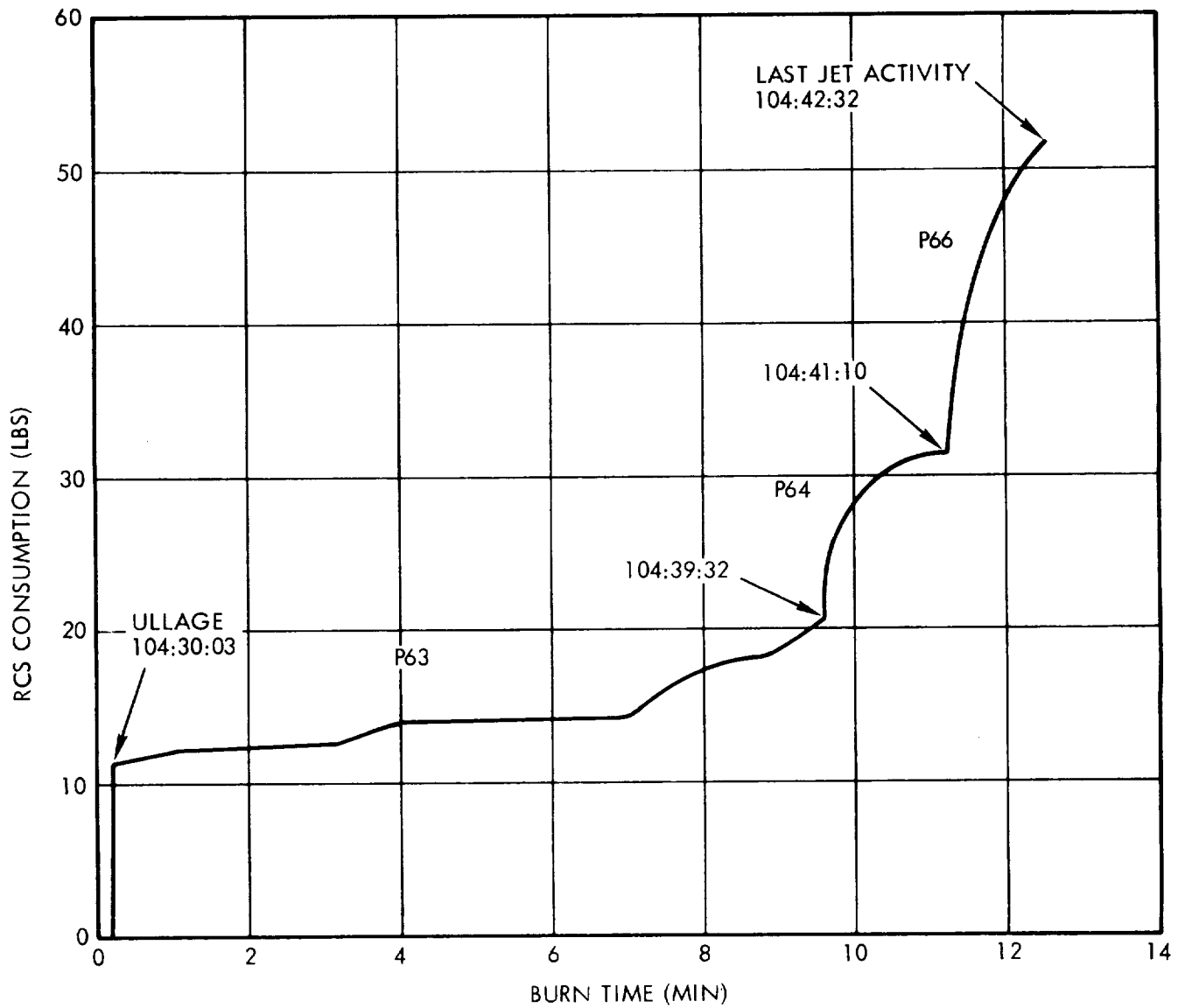


FIGURE 4-9. APOLLO 15 RCS PROPELLANT CONSUMPTION DURING POWERED DESCENT

REFERENCES

1. MSC Report MSC-05161, "Apollo MIssion Report," dated December 1971.
2. MSC Report MSC-04789, "Apollo 15 LM Descent Postflight Analysis," (Addendum), dated 17 September 1971.
3. TRW Report 11176-H524-R0-00, "Apollo XII Guidance, Navigation and Control Systems Performance Analysis Report," dated 8 April 1970.

